THE UNIVERSITY OF CHICAGO

SURFACE STABILITY, PHONON BAND STRUCTURE, AND VIBRATIONAL DYNAMICS OF THE NB(100) SURFACE OXIDE RECONSTRUCTION

A DISSERTATION SUBMITTED TO

THE FACULTY OF THE DIVISION OF THE PHYSICAL SCIENCES

IN CANDIDACY FOR THE DEGREE OF

DOCTOR OF PHILOSOPHY

DEPARTMENT OF CHEMISTRY

BY

ALISON ANN MCMILLAN

CHICAGO, ILLINOIS

MARCH 2022

Copyright © 2022 Alison Ann McMillan

All Rights Reserved

The wall was built of jasper, while the city was pure gold, like clear glass. The foundations of the wall of the city were adorned with every kind of jewel. The first was jasper, the second sapphire, the third agate, the fourth emerald, the fifth onyx, the sixth carnelian, the seventh chrysolite, the eighth beryl, the ninth topaz, the tenth chrysoprase, the eleventh jacinth, the twelfth amethyst. And the twelve gates were twelve pearls, each of the gates made of a single pearl, and the street of the city was pure gold, like transparent glass. *Rev. 21:18-21*

Table of Contents

List of Figures

List of Tables

Acknowledgments

Thank you to Peter Walhout and Ben Lovaasen for shifting me from math to chemistry, convincing me to apply to graduate school, and showing me how the beauty of chemistry points us to its source.

Thank you to my advisor, Steve Sibener, for bringing me to UChicago, welcoming me into your group, teaching me how to design and think through the entire experimental process, and being more kind, supportive, and encouraging than I could have imagined.

Thank you to my committee members, Ka Yee Lee and Greg Engel, for taking the time to be on my candidacy and thesis committees and guide me through the most important milestones of my graduate career.

Thank you to Melinda Moore, Maria Jimenez, Tanya Hagerman, and Vera Dragisich for making my part in the administrative aspects of my graduate degree understandable and minimal.

Thank you to John Phillips and Bentley Wall for keeping the building running and handling my many reorganizations of Sibener group belongings, and to Luigi Mazzenga for helping me navigate the rather terrifying devices in the machine shop.

Thank you to Kevin Gibson for being an invaluable source of knowledge of all sorts, for showing us the humorous side of the experimental process, and for the massive compliment when you said I would make a good motorcycle driver.

Thank you to the Sibener group: to Grant, Kevin, Jon, Darren, Jeff, Jacob, Becca, Ross, Tim, Sarah B., Michelle, Julia, Rachael, Sarah W., Caleb, Josh, Stephen, Blake, Jasper, Mark, and Michael, for aiding in experimental difficulties, putting up with my rummaging and cleaning, and appreciating that life does not revolve around lab.

Thank you to Kevin Nihill for introducing me to the world of helium scattering and showing me how to run a lab, and to Caleb Thompson for reminding me how to actually think like a scientist when it seems all hope is lost.

Thank you to Jacob Graham for teaching me every single thing I know about conducting experiments, modifying equipment, and generally surviving life in a lab in good spirits.

Thank you to Michelle Brann for being my inseparable companion during first year and beyond, as we learned to fix the myriad issues in lab while staying sane.

Thank you to Dave, Lisa, Bing, and Christy, for giving your lives to the proclamation of the Gospel, for leading our church, and for supporting me during my time in Hyde Park.

Thank you to my church, especially John, Joan, Jim, Jill, Bill, and Betty-Ann: you welcomed me into your family and became the most important part of my life in Chicago.

Thank you to Ezra, Finley, Archie, and Vivian (among others) for giving me joy and laughter and for keeping my priorities aligned.

Thank you to Christy, Annie, Whitney, Torie, Maggie, Eden, Kelsey, Rachel, and many others for walking alongside me in all the ups and downs of graduate school and for redirecting my attention towards our true Helper.

Thank you to Uncle Doug, Auntie Kelly, Joelle, Sulty, and Zuzu (and Ethan, Marie, and Naboo) for your amazing hospitality when I needed it most; for your encouragement, grace, and laughter; and for helping me stand up on all sorts of waves.

And finally, thank you to my family: to Dad, Mom, Brendan, Sharon, Elise, Matthew, and Allison, for encouraging me first and foremost to follow my Savior while taking the steps He has put in front of me.

Hither to hath the LORD led.

Abstract

Niobium is the current industry standard for modern superconducting radiofrequency cavities in particle accelerators, but technology has pushed these cavities to niobium's fundamental limits. Future progress rests on improved growth procedures for existing materials and the development of new materials, and a complete, detailed, atomic-scale characterization of the niobium surfaces used in accelerators is a prerequisite for this progress. Towards this end, this thesis contains a set of experiments that employ helium atom scattering to describe the (3 × 1)-O reconstruction of the Nb(100) surface.

Elastic helium diffraction from the (3 × 1)-O Nb(100) surface is used to characterize the structure of the surface over a wide range of high temperatures. High-resolution helium diffraction and line-shape analysis, confirmed by Auger electron spectroscopy, reveal that the (3 × 1)-O reconstruction is stable up to at least 1130 K. The atomic-scale surface structure, composition, and coherence do not change up to this temperature, which exceeds the temperature at which niobium is held during typical tin nucleation procedures.

Inelastic helium time-of-flight measurements are used to map out the phonon band structure of the Nb(100) oxide and determine the nature of the surface's vibrational dynamics and force constants. Density-functional theory calculations correspond with measured phonon dispersions and elucidate the atomic displacement patterns for each measured phonon resonance. The difference between the calculated bare and oxidized Nb(100) surfaces show that the oxide disperses electron-phonon coupling strengths to higher energies and significantly increases force constants at the surface, potentially affecting surface superconductivity and superconducting radiofrequency cavity behavior.

Chapter 1

Introduction

Surface science, the study of the interface of two phases, has led to the revolution of many day-to-day life processes. For example, semiconductor and biomedical devices, fuels, heterogeneous catalysis technology, and adhesives all owe their development to a molecular-level understanding of surfaces.[1] The atomic and electronic structures at a surface differ significantly from bulk: symmetry is broken and each atom on the surface has fewer nearest neighbors than a corresponding atom in the bulk of the material.[2] This leads to higher chemical reactivities, opening the door for the development of new materials and new uses for old materials.[1] Technological advances, however, come about through a foundation of information that at first can seem to be "in the weeds" of fundamental physics. While building technology and improving lives is one goal of science, the pursuit of knowledge for the sake of knowledge itself is a worthy endeavor. The two go hand-in-hand: many major advances have come through a scientist's curiosity about the intricate workings of the physical world. Describing the basic structure of a crystalline surface both paves the way for future practical discoveries and deepens our understanding of nature.

One of the most successful methods of analyzing a solid surface involves the vacuum-solid interface: by isolating a surface in vacuum, techniques can be used to probe directly the surface's chemical composition, structure, and dynamics. The vacuum allows electrons, X-rays, or other particles to travel to, interact with, and leave a clean surface without interference from ambient gas molecules.[3] Many important techniques have been developed that take advantage of this interface, including low-energy electron diffraction (LEED), Auger electron spectroscopy (AES), scanning tunneling microscopy (STM), and atomic force microscopy (AFM). One such technique,

supersonic atomic and molecular beam scattering, originated with crossed-beam experiments.[3] Many gas-phase reactions were characterized successfully through the interaction of multiple supersonic beams, and this led to improvements in supersonic beam technology. Directing beams at solid surfaces introduced a new surface-sensitive technique: while other probes, such as neutrons, electrons, and X-rays, have similar velocity profiles and can be used to study crystal lattices, helium atoms are neutral and reflect off the electron density above the surface.[2] Helium atom scattering (HAS) is reproducible, non-destructive, strictly surface sensitive, and adjustable—beam energy can be controlled simply through nozzle temperature.[4]

This thesis uses HAS to understand and characterize a niobium oxide. As the current material of choice for superconducting radiofrequency (SRF) cavities in particle accelerators, niobium has pushed accelerator technology to higher efficiencies and higher fields.[5] Accelerators are used in a wide range of applications, from high-energy particle physics to medical imaging devices.[6] Future progress in SRF technology rests on the development of new materials and cavity treatment processes, which requires an in-depth, atomic-scale characterization of niobium and niobium oxide. Helium scattering provides a unique method by which the niobium oxide surface can be explored over a wide range of temperatures.

Chapter 2 details the theory and experimental capabilities needed for HAS. A brief introduction to crystal theory, surface phonons, and atomic beam scattering is given. The vacuum instrument used for the succeeding experiments is described in detail, as well as data analysis techniques, crystal preparation procedures, and typical experimental parameters.

Once He scattering is understood and defined, it can be used to address technologically relevant surface science questions. In **Chapter 3**, the adaptability of HAS is used to characterize the (3×1)-O reconstruction of the Nb(100) surface at high temperatures. While some surface

science techniques, such as STM, are unable to measure surface structures at high temperatures due to atomic movements, elastic He scattering can be used over a wide range of surface temperatures. Here it is found that the (3 × 1)-O Nb(100) surface is stable up to temperatures of at least 1130 K. One promising candidate to replace Nb in particle accelerators is Nb_3Sn; current fabrication processes include Sn deposition on Nb, with nucleation occurring at surface temperatures within the range measured here.[7] A thorough understanding of the Sn alloying process starts with a thorough understanding of the Nb oxide surface, and the stability of the (3 × 1)-O Nb(100) surface up to temperatures of at least 1130 K carries implications for Nb SRF cavities.

The surface sensitivity of He scattering gives it a unique ability to probe surface phonons: the de Broglie wavelength of a typical He beam is on the same order of magnitude as crystal lattice constants, and beam energies are similar to surface phonon energies.[8] **Chapter 4** continues the characterization of the (3 × 1)-O Nb(100) surface, but with inelastic scattering measurements that are verified by density-functional theory (DFT). The surface Brillouin zone is mapped out with inelastic HAS and compared with DFT calculations of both the bare Nb(100) surface and the (3 × 1)-O Nb(100) surface. Results show the importance of the oxide to surface dynamics and bonding, highlighting the need for role of the oxide to be included in any study of Nb SRF cavities.

Chapter 2

Theoretical Background and Experimental Methods

Helium atom scattering (HAS) uses fundamental surface science, scattering theory, and ultra-high vacuum (UHV) techniques to study and characterize surface structure and dynamics. This chapter contains a review of these essential concepts, a detailed description of the scattering apparatus used for the succeeding experiments, and an explanation of data analysis techniques. The review begins with crystalline surfaces and phonons before tracing the progression from basic crystal theory to HAS measurement techniques. Next the UHV instrument, with its three primary regions—beamline, scattering chamber, and rotatable detector—is explained in detail and connected to the scattering theory it demonstrates. Lastly, the equations necessary for interpreting HAS data are explained.

2.1 Crystals, Surfaces, and Phonons

An ideal crystal lattice can be described by a unit cell that is repeated and stacked to fill a three-dimensional space. From a defined origin, each point $\vec{r}$ in the crystal is the same as the point $\vec{r}'$,[9]

$$\vec{r}' = \vec{r} + n_1 \cdot \vec{a} + n_2 \cdot \vec{b} + n_3 \cdot \vec{c}, \tag{2.1}$$

where n_1, n_2, and n_3 are integers and $(\vec{a}, \vec{b}, \vec{c})$ are the unit cell vectors. An ideal surface is made by taking a planar cut through the crystal and is denoted by the Miller indices of that bulk plane. The surface can be described by only two unit cell vectors:

$$\vec{r}' = \vec{r} + n_1 \cdot \vec{a} + n_2 \cdot \vec{b}. \tag{2.2}$$

While many different crystal and surface configurations exist, this thesis will focus on the body-centered cubic (BCC) structure seen in Nb and, more specifically, on the Nb(100) surface. Here, $|\vec{a}| = |\vec{b}|$ and the angle between the two vectors is $\gamma = 90°$.[9]

To understand diffraction experiments, it is useful to convert a lattice into reciprocal space. The two-dimensional reciprocal surface lattice vectors, $\vec{a}^*$ and $\vec{b}^*$, can be defined in terms of the real-space vectors $\vec{a}$ and $\vec{b}$ by[10]

$$\vec{a}^* = 2\pi \frac{\vec{b}\times\vec{n}}{\vec{a}\cdot(\vec{b}\times\vec{n})},\ \vec{b}^* = 2\pi \frac{\vec{n}\times\vec{a}}{\vec{a}\cdot(\vec{b}\times\vec{n})}, \tag{2.3}$$

where $\vec{n}$ is the surface-normal unit vector. Any point in the reciprocal lattice, then, can be obtained through the translation vector

$$\vec{G}_{hk} = h\vec{a}^* + k\vec{b}^*, \tag{2.4}$$

where h and k are integers known as Miller indices.[9] As will be seen with HAS, diffraction peaks are designated by Miller indices, as are crystallographic faces, e.g. Nb(100).[9]

An important region in reciprocal space is the Brillouin zone (BZ). The first BZ can be constructed by drawing lines from a reciprocal lattice point that is defined arbitrarily as the origin, (00), to the nearest neighboring reciprocal lattice points. Perpendicular lines drawn at the midpoints of each of these lines form an enclosed area: the smallest area that contains the origin is the first BZ.[10] All lattice vibrations or diffraction peaks from a surface can be linked to an analogous vibration or peak within the first surface Brillouin zone (SBZ).[9,11] By convention, the center of the first SBZ is labeled as $\bar{\Gamma}$, with other high symmetry points labeled as $\bar{X}$, $\bar{M}$, etc. Bulk BZ edges are labeled in a similar manner, but without bars.[2]

The simplest description of a crystal vibration, or phonon, starts with a one-dimensional chain of atoms of mass M separated by the lattice spacing a, as seen in Figure 2.1. Assuming the

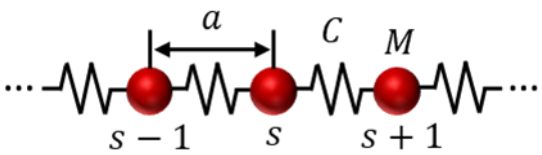

Figure 2.1: Representation of a one-dimensional chain of atoms of mass M connected by springs with force constants C.

force between any two adjacent atoms can be described as a spring with force constant C, the force, F_s, acting on atom s can be written in terms of the displacements, u:[9]

$$F_s = C(u_{s+1} - u_s) + C(u_{s-1} - u_s). \tag{2.5}$$

As described in solid state physics textbooks, the solution to the time-dependent equation of motion for the atomic displacements is a traveling wave. The dispersion relation, showing how the frequency of the wave, ω, behaves as a function of the wavevector, K, is[9,11]

$$\omega = \left(\frac{4C}{M}\right)^{\frac{1}{2}} \left|\sin\frac{1}{2}Ka\right|. \tag{2.6}$$

For three-dimensional crystals with multiple atoms per unit cell, the dispersion relation becomes much more complicated, with multiple solutions available for ω. Each solution becomes a branch within the phonon dispersion plot of phonon energy vs. phonon wavevector, $\vec{q} = (q_x, q_y, q_z)$. In general, at each value of $\vec{q}$ there are $3n$ branches for a crystal with n atoms per unit cell.[11] Three branches are acoustic, with the atoms moving coherently, while the remaining $3n - 3$ branches are optical, with each atom moving out-of-phase with its neighbor.[11] Acoustic phonons can be categorized further into longitudinal (L) phonons, where atomic displacement is along the direction of wave propagation, and transverse (T) phonons, where atomic displacement is perpendicular to the direction of wave propagation.

When a crystal is cut along a symmetry axis to form a surface, the termination of the bulk at the surface perturbs the system. The phonons at the surface can be divided into two types: bulk

phonons that are projected onto the two-dimensional surface, and surface-localized phonons that are created by the perturbation.[2]

First, consider the bulk phonons projected onto the surface. Within a three-dimensional crystal, discrete phonons in a dispersion plot are identified by their three-dimensional wavevector, $\vec{q}$. Once a surface is formed, these phonons are projected onto two dimensions, with two-dimensional wavevector $\vec{Q} = (q_x, q_y)$. Each wavevector parallel to the surface, $\vec{Q}$, is associated with many wavevectors normal to the surface, q_z, where $\vec{q} = (\vec{Q}, q_z)$. Each bulk phonon branch creates as many phonon branches on the two-dimensional surface as there are possible values of q_z; for a theoretical calculation using the slab method where the slab has N layers, there are N values of q_z. Similar to how a three-dimensional sphere projected onto a two-dimensional plane becomes a circle, the three-dimensional bulk phonons projected onto a two-dimensional surface collapse and form a band. For a crystal with n atoms per unit cell, there are $3n$ degrees of freedom and $3n$ surface-projected bands in the two-dimensional phonon dispersion spectrum. Using the slab method, this creates $\nu = 3nN$ total modes in the two-dimensional representation for each value of $\vec{Q}$.[2] ν increases as the number of layers in the slab increases, making the surface-projected bulk bands denser. The frequency distribution for all bands is known as the $\vec{Q}$-selected phonon density of states (DOS).

Second, consider the phonons localized on the surface. When a surface is formed, a layer of bonds is broken, modifying the force constant matrix. In 1896, Lord Rayleigh proposed a theorem saying that a surface-localized perturbation would generate surface-localized phonon modes.[2] These modes separate from the surface-projected bulk band; typically, they can be found below the bulk band. The lowest energy acoustic mode is named the Rayleigh wave.

These surface modes can be acoustic or optical, and their displacement amplitudes decay exponentially to zero with increasing distance from the surface. Each mode can be categorized by the direction of its displacement. As mentioned before, acoustic phonons can be either longitudinal (L) or transverse (T). At the surface, transverse phonons can be categorized further into either shear-vertical (SV), where polarization is out-of-plane, or shear-horizontal (SH), where polarization is in-plane. Rayleigh waves are elliptically polarized with a quasi-SV nature.[2]

There also can be overlap between surface-localized modes and surface-projected bulk bands. When polarizations are not orthogonal to bulk modes this causes mixing, and when polarizations are orthogonal to bulk modes this causes pseudo-surface modes. Mixed modes have displacements that are large at the surface but do not decay to zero within the bulk of the crystal, while pseudo-surface modes are localized at the surface but can occur only along a symmetry axis.[2]

2.2 Supersonic Helium Beams

The first He atom diffraction experiments were reported in 1930, when Estermann and Stern diffracted effusive He from LiF and NaCl surfaces.[12] These experiments made at least two significant contributions to surface science. Coming directly on the heels of de Broglie's 1929 Nobel Prize in Physics for the wavelike nature of particles, Estermann's and Stern's He diffraction peaks confirmed that de Broglie was correct to extend his theory from electrons to all matter. Additionally, Estermann and Stern introduced a powerful new technique that could study surfaces without causing any damage, and indeed, without touching the surface at all.

He atom beams are low-energy, neutral, and chemically inert. Supersonic He beams typically range in energy from 10 meV ($\lambda \sim 1.4$ Å) to 85 meV ($\lambda \sim 0.5$ Å); these de Broglie wavelengths are within the order of magnitude of crystal lattice parameters, allowing He atoms to

characterize surface structure.[8] He atoms in this energy range do not penetrate the surface electron density: the classical turning point is about 1–3 Å away from the centers of the surface atoms or molecules. This results in a probe that is similar to neutrons or X-rays, but that is highly surface-sensitive and suitable for insulators, conductors, and semiconductors.[8] The most effective He beams are supersonic. Supersonic beams are more intense and have much narrower velocity distributions ($\Delta v/v \leq 1\%$) than effusive sources, allowing for precise control over scattering kinematics and high-resolution determination of surface structure and dynamics.[3]

Generation of a supersonic He beam starts with a high-pressure source of gas that enters a vacuum through a nozzle of diameter D. If the mean free path of the atoms in the source is λ_0, a nozzle diameter of $D \gg \lambda_0$ ensures that the atoms collide with each other many times during the expansion process.[13] With a high backing-pressure, P_0, on the source side of the nozzle and a low background pressure, P_b, on the vacuum side of the nozzle, the resulting gas flow in the vacuum can be considered as an adiabatic, isentropic expansion. Since He is small and monoatomic, it acts as an ideal gas with a constant heat capacity ratio $\gamma = C_p/C_v$, where C_p and C_v are the specific heat capacities at constant pressure and volume, respectively (γ = 5/3 for He). An adiabatic expansion requires that the sum of the beam's enthalpy and kinetic energy along a streamline is conserved, which limits the beam velocity (v_{max}) and kinetic energy (E_B) to[3]

$$v_{max} = \sqrt{\frac{2k_B T_0}{m}\left(\frac{\gamma}{\gamma-1}\right)} \text{ and } E_B = \left(\frac{\gamma}{\gamma-1}\right) k_B T_0, \tag{2.7}$$

where m is the mass of a He atom, k_B is Boltzmann's constant, and T_0 is the nozzle stagnation temperature. The Mach number, M, of an expansion is defined as the ratio of the average speed of the expanding gas, v, to the local speed of sound of the gas, v_b. Using properties of ideal gases and assuming an internal beam temperature of T, M can be written as

$$M = \frac{v}{v_b} = \sqrt{\frac{mv^2}{\gamma k_B T}}. \tag{2.8}$$

As M increases, T decreases and narrows the internal velocity distribution. The atomic flow becomes supersonic when $M > 1$; in terms of pressure, this requires that[3]

$$\frac{P_0}{P_b} \geq \left[\frac{1}{2}(\gamma + 1)\right]^{\frac{\gamma}{\gamma - 1}}. \tag{2.9}$$

The higher the Mach number, the higher the quality of the beam. Excellent supersonic He beams have Mach numbers of over 200, which requires a high collisional frequency in the nozzle before expansion into the vacuum chamber. The frequency of collisions is governed by the product $P_0 D$, while He beam flux leaving the nozzle is proportional to $P_0 D^2$.[8] The sensitivity of beam flux to nozzle diameter requires that the vacuum chamber have high-throughput pumping. To maintain reasonable pumping speeds, high-quality beams use high source pressures and small nozzles ($D \sim 15$ μm), while low background pressures are achieved via differential pumping.

After passing through the nozzle, the beam expands into vacuum until it reaches free molecular flow, where almost no collisions occur. A conical skimmer strategically placed in this region minimizes shock waves and collimates the beam into He atoms traveling with approximately the same translational energy. The energy of the beam is controlled by the beam's nozzle temperature.[3]

According to de Broglie's theory, He atoms traveling with momentum p, mass m, velocity v, and energy E may be treated as a wave, with wavelength, λ, [14]

$$\lambda = \frac{h}{p} = \frac{h}{mv} = \frac{h}{\sqrt{2mE}}, \tag{2.10}$$

where h is Planck's constant. The wavevector, $\vec{k}_i$, of a beam is related to its wavelength via $k_i = 2\pi/\lambda$; using the beam energy after expansion given in Equation 2.7 with T_N representing beam

temperature, the incident energy, E_i, and velocity, v, of a beam striking a surface can be expressed as:

$$E_i = \frac{1}{2}mv^2 = \frac{\hbar^2}{2m}k_i^2 = \frac{5}{2}k_B T_N; \tag{2.11}$$

$$v = \sqrt{\frac{5k_B T_N}{m}}. \tag{2.12}$$

2.3 Helium Atom Scattering

A He atom can scatter from a crystal in one of two ways: either it scatters elastically, where no energy is exchanged with the surface, or it scatters inelastically, where energy is exchanged with the surface. These two scattering processes create the two major categories of HAS experiments. Diffraction experiments use elastic scattering to characterize surface structure, while time-of-flight (TOF) experiments use inelastic scattering to characterize surface vibrations and dynamics. Both experimental techniques and the data analysis methods used for each are described below.

2.3.1 Elastic Scattering and Diffraction Analysis

During an elastic scattering event, the incident and final energies of the He atom are equal: $E_i = E_f$. If the surface is crystalline with a periodic structure, the Laue equations dictate that the change in momentum between the final, $\vec{k}_f$, and incident, $\vec{k}_i$, beams must equal a reciprocal lattice vector, $\vec{g}$:[8]

$$\Delta\vec{k} = \vec{g} \Rightarrow \vec{k}_f = \vec{k}_i + \vec{g}. \tag{2.13}$$

Usual convention puts the surface in the $x-y$ plane with surface normal along the z-axis.

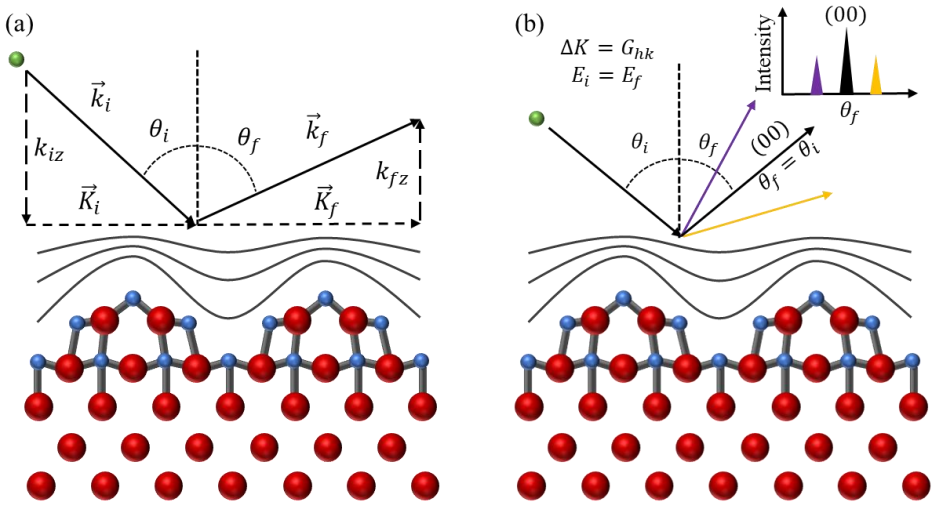

Figure 2.2: Illustration of a He atom scattering elastically from the (3 × 1)-O Nb(100) surface. Scattering wavevector components are defined in (a); (b) shows the positions of measured diffraction peaks relative to specular (black) for forward (yellow) and backward (purple) scattering.

Wavevector components parallel to the surface are labeled with capital letters, e.g. $\vec{k}_i = (\vec{K}_i, k_{iz})$. In-plane diffraction, where the He atom diffracts in the plane defined by the z-axis and the incident wavevector, is illustrated in Figure 2.2. The Laue equation for in-plane diffraction becomes:[8]

$$\Delta\vec{K} = \vec{K}_f - \vec{K}_i = \vec{G}_{hk}, \tag{2.14}$$

where $\vec{G}_{hk}$ is the sum of reciprocal surface lattice vectors with Miller indices h and k, as in Equation 2.4. Using the angles and wavevector components defined in Figure 2.2(a), the parallel momentum transfer ΔK can be written:

$$\Delta K = K_f - K_i = k_i(\sin\theta_f - \sin\theta_i) = G_{hk}. \tag{2.15}$$

He diffraction peaks occur when this relation is satisfied, and peaks are labeled with the Miller indices corresponding to their respective reciprocal surface lattice vectors, (hk). Diffraction can occur on both angular sides of specular, as seen in Figure 2.2(b). Forward scattering occurs when $\theta_f > \theta_i$ and results in positive values of ΔK; backward scattering occurs when $\theta_f < \theta_i$ and results

in negative values of ΔK. An illustration of the relative positions of measured He diffraction peaks is shown in the inset of Figure 2.2(b).

For the diffraction experiments described herein, a pre-collision chopper is set to a square-wave pattern (50% duty cycle). Scattered signal is collected during the open channel while background signal is collected during the closed channel, and a triggering slot on the chopper sets a start time for the He beam. Using the known total flight path from the chopper to the post-collisional detector, L_{CD}, elastic travel time t_0, and beam temperature T_N, Equations 2.11 and 2.12 can be rearranged to determine the incident wavevector of a beam:

$$k_i = \frac{mL_{CD}}{\hbar t_0}; \tag{2.16}$$

$$t_0 = \sqrt{\frac{mL_{CD}^2}{5k_B T_N}}. \tag{2.17}$$

HAS is very sensitive to surface disorder, and indeed the specular peak, where $\theta_i = \theta_f$, can be used to determine the average domain size of a particular crystal.[15] The domain size broadening, $\Delta\theta_w$, is a convolution of the measured full-width-half-maximum (FWHM) of the specular peak, $\Delta\theta_{exp}$, and the instrument function broadening, $\Delta\theta_{inst}$:

$$\Delta\theta_w^2 = \Delta\theta_{exp}^2 - \Delta\theta_{inst}^2. \tag{2.18}$$

The crystal's coherence length, l_c, or average domain size, can be found through $\Delta\theta_w$ according to the relation[15,16]

$$l_c = \frac{5.54}{\Delta\theta_w k_i \cos\theta_f}. \tag{2.19}$$

2.3.2 Inelastic Scattering and Time-of-Flight Analysis

For an inelastic scattering event, the He atom exchanges energy with the surface. This

energy exchange occurs through the creation or annihilation of a phonon, and the conservation of energy becomes:

$$\Delta E = E_f - E_i = \hbar\omega, \tag{2.20}$$

where E_f and E_i are again the final and initial energies of the He atom, respectively, and $\hbar\omega$ is the energy of a phonon with frequency ω. By using Equation 2.11, this becomes

$$\Delta E = \frac{\hbar^2}{2m}k_f^2 - \frac{\hbar^2}{2m}k_i^2 = \hbar\omega. \tag{2.21}$$

For inelastic scattering, $k_i \neq k_f$, so the parallel momentum exchange in Equation 2.15 becomes:

$$\Delta K = K_f - K_i = k_f \sin\theta_f - k_i \sin\theta_i = G_{hk} + Q, \tag{2.22}$$

where Q is the wavevector for the phonon being created or annihilated. Combining Equations 2.21 and 2.22 gives what is known as the scan curve,[8]

$$\Delta E = \frac{\hbar^2}{2m}\left[\frac{(k_i \sin\theta_i + \Delta K)^2}{\sin^2\theta_f} - k_i^2\right], \tag{2.23}$$

which defines all possible observable phonon energies and exchanged parallel momentum for a given set of He scattering conditions.

Phonons can be characterized with TOF experiments, which are based on the simple definition of speed and measure scattered intensity per unit of flight time. The speed, v, of an atom is determined by the distance traveled, L, and the time the atom takes to travel that distance, t, while the atom's kinetic energy, E, can be written in terms of its speed:

$$v = \frac{L}{t} \text{ and } E = \frac{1}{2}mv^2. \tag{2.24}$$

For a He atom scattering from a crystal, there are two different speeds to be considered. There is the speed of the atom before it hits the crystal and the speed of the atom after it hits the crystal. Timing is determined by a pre-collisional chopper. The chopper can be set either to a single-slit modulation mode (1% duty-cycle) or a pseudo-random cross-correlation mode (50% duty-cycle),

which allows for a much higher signal-to-noise ratio.[17] The speed of the atom before scattering can be written in terms of the time, t_{CS}, the atom takes to travel the distance L_{CS} from the chopper to the sample, while the speed of the atom after scattering can be written in terms of the time, t_{SD}, the atom takes to travel the distance, L_{SD}, from the sample to the detector. During a TOF experiment, the known variables are the distances and the total time taken to travel from the chopper to the detector: $t_{CD} = t_{CS} + t_{SD}$. The measured arrival times of elastically and inelastically scattered He will differ because of differing sample-to-detector times, t_{SD}. The total flight time of an elastically scattered atom, t_0, can be used to determine the initial energy of an inelastically scattered atom and provides a method to determine the time it takes that inelastically scattered atom to travel from the sample to the detector:

$$t_{SD} = t_{CD} - \frac{L_{CS}}{L_{CD}} t_0. \tag{2.25}$$

The change in energy of an inelastically scattered atom, and hence the energy of the created or annihilated phonon, is found by using Equations 2.20, 2.24, and 2.25, where $t_{obs} = t_{SD}$ for that atom. Since t_{CS} is the same for both the elastically and inelastically scattered atoms, the energy of the phonon is:[18]

$$\hbar\omega = \Delta E = E_f - E_i = \frac{1}{2}\left(v_f^2 - v_i^2\right) = \frac{1}{2} m \left[\frac{L_{SD}^2}{\left(t_{obs} - \frac{L_{CS}}{L_{CD}} t_0\right)^2} - \frac{L_{CD}^2}{t_0^2}\right], \tag{2.26}$$

and the momentum of the phonon can be found using Equation 2.22, where

$$k_f = \frac{m L_{SD}}{\hbar\left(t_{obs} - \frac{L_{CS}}{L_{CD}} t_0\right)}. \tag{2.27}$$

TOF intensity is recorded as a function of time. Since the transformation from the time domain to the energy domain in Equation 2.26 is nonlinear, the relative amplitudes of inelastic peaks change significantly during the transformation, while the area under a given peak is kept

constant. The Jacobian of the transformation describes the intensity scaling of this nonlinear relationship. If the distribution of intensities measured by the TOF is $f(t_{obs})$ and the distribution as a function of energy exchange is $f(\Delta E)$, then the number of detector particles, dN—the area under the curve—is conserved, and[18]

$$dN = f(t_{obs})dt_{obs} = f(\Delta E)d(\Delta E). \tag{2.28}$$

Since

$$dv = -\frac{L_{SD}}{t_{obs}^2}dt_{obs}, \tag{2.29}$$

then

$$d(\Delta E) = mvdv = m\frac{L_{SD}^2}{t_{obs}^3}dt_{obs} \tag{2.30}$$

and the Jacobian becomes:

$$\frac{dt_{obs}}{d(\Delta E)} = \frac{t_{obs}^3}{mL_{SD}^2}. \tag{2.31}$$

However, the detector used for this thesis is sensitive to number density, not particle flux. As will be seen, He atoms are ionized by electron bombardment before striking the detector. Since particles moving slowly have a greater ionization cross-section than particles moving quickly, ionization efficiency is inversely proportional to final particle velocity, v_f, and the corrected scaling factor can be found:

$$f(\Delta E) = \frac{t_{obs}^3}{mL_{SD}^2}v_f f(t) = \left(\frac{t_{obs}^2}{mL_{SD}}\right)f(t_{obs}). \tag{2.32}$$

2.4 Experimental Apparatus and Parameters

This section details the apparatus used for HAS experiments. After a brief overview of UHV conditions, the three main components of the HAS instrument are explained in detail: the

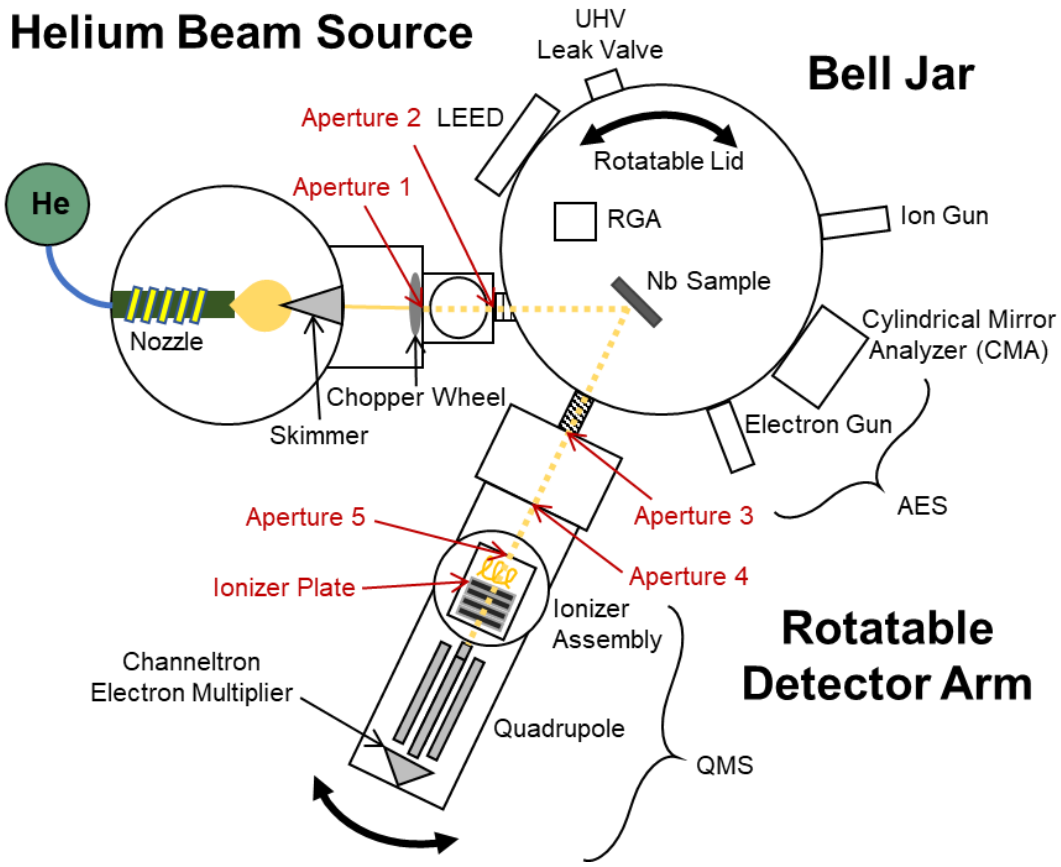

Figure 2.3: Schematic of the He atom scattering apparatus, with instrumentation used in this thesis identified. The collimating apertures are labeled in red.

atomic beamline, the scattering chamber, and the rotatable detector. This is followed by a description of the crystal preparation method and experimental parameters used in the succeeding chapters. A schematic of the HAS instrument is shown in Figure 2.3.

2.4.1 Ultra-High Vacuum

An instrument under UHV is a prerequisite for the He scattering experiments described in the following chapters. UHV, where the pressure is at or below 10^{-9} Torr, is necessary for two primary reasons. First, it greatly diminishes the number of collisions an atom experiences when

Degree of Vacuum	Pressure (Torr)	Gas Density (molecules/m^3)	Mean Free Path (m)	Time/ML (s)
Atmospheric	760	2×10^{25}	7×10^{-8}	10^{-9}
Low	1	3×10^{22}	5×10^{-5}	10^{-6}
Medium	10^{-3}	3×10^{19}	5×10^{-2}	10^{-3}
High	10^{-6}	3×10^{16}	50	1
Ultra-High	10^{-10}	3×10^{12}	5×10^{5}	10^{4}

Table 2.1: Approximate pressure, gas density, mean free path, and time required to form a monolayer for each vacuum regime, spanning from atmospheric to ultra-high.

traveling through a chamber, allowing a beam of atoms to reach a scattering target without being deflected by nearby gas-phase atoms. The mean free path of an atom, λ, depends on the background pressure, P, temperature, T, and scattering cross section, σ:

$$\lambda = \frac{k_B T}{\sqrt{2} P \sigma}. \tag{2.33}$$

An increase in gas temperature or a decrease in pressure will increase λ: the lower the vacuum pressure, the fewer the number of atoms deflected either before or after scattering from the sample. In UHV, $\lambda \sim 10^5$ m. The second reason for UHV conditions during scattering experiments is surface cleanliness. Even in the cleanest vacuum chamber, there always will be trace contaminants that can adsorb to the scattering surface. HAS is extremely surface sensitive; any adsorbate will reduce scattered signal and impede experimental reproducibility. The rate at which a monolayer of adsorbates will form on a sample depends on the pressure. For pressures on the order of 10^{-10} Torr, a monolayer will form in about 10^4 seconds. Table 2.1 shows the approximate gas densities, mean free paths, and times needed to form monolayers for a range of pressures. The experiments described in the following chapters were taken at elevated surface temperatures ($T_S > 300$ K). This caused the scattering chamber walls to heat up and release adhered gas molecules, which in turn

increased the background pressure of the chamber. To reduce this effect, the chamber was baked at ~370 K for multiple days before crystal preparation and scattering experiments.

2.4.2 Atomic Beamline

The beamline is composed of three differentially pumped regions: the source region and the first and second differential stages. Ultra-high purity He gas is controlled by a single-stage gas regulator (Airgas, Y11-N198K), with backing pressures between 300–1200 psi. He enters the source region through 15 μm Mo circular pinhole (SPI) that sits at the end of a custom-built elkonite (Cu-W alloy) nozzle. The nozzle is wrapped around the second stage of a closed-cycle He refrigerator (Advanced Research Systems, DE-202A), which enables temperature control of the He beam. The temperature of the nozzle is measured by a Si diode (Lakeshore Cryotronics, DT-470-SD-13-3S); a resistive ribbon heater (Advanced Research Systems, 36 Ω) wraps around the nozzle and is run by a PID controller (Lakeshore Cryotronics, Model 325). The entire nozzle manifold is wrapped in Mylar superinsulation to limit thermal loss due to radiative heating. The PID controller holds the nozzle within ± 0.1 K of operating temperatures, T_N, between 50 K and 400 K, which correspond to He beam energies, E_i, between 11 meV and 86 meV. The high backing pressures used for a supersonic beam create a very large atomic flux in the source chamber. This requires high pumping speeds and large throughputs, which is accomplished by an 8000 L/s diffusion oil pump (Varian, VHS-400) backed by a 750 m^3/h roots blower (Pfeiffer, WKP 500AM) in series with a 70 m^3/h rotary vane pump (Pfeiffer, Duo65MC). The source chamber has a base pressure of 1×10^{-7} Torr that increases to the order of 1×10^{-4} Torr when a He beam is flowing.

The beam exits the source chamber and enters the first differential stage through a conical, Ni skimmer (Beam Dynamics, Model 2), which has a diameter of 0.5 mm and sits approximately

1 cm away from the end of the nozzle. The skimmer collimates the expanded beam by selecting only its centerline, and its position is optimized to minimize shock waves. The first differential stage is pumped by a 700 L/s diffusion oil pump (Edwards, Diffstak 160) backed by a 70 m^3/h rotary vane pump (Pfeiffer, Duo65MC), and it houses a chopper wheel used to modulate the beam and start the timing for TOF measurements. The chopper is a 15 cm-diameter wheel mounted on a linear feedthrough (Huntington, VF-108), by which the wheel's vertical position can be adjusted, modifying the point of intersection of the beam axis and the chopper. Three different modulation patterns can be used, each at a specific radius from the center of the chopper. A square-wave pattern (50% duty-cycle) is used for diffraction experiments, while TOF experiments use either the single-shot (1% duty-cycle) or cross-correlation (50% duty-cycle) patterns. Single-shot has four trigger slots per revolution and allows for high-resolution TOF measurements, while cross-correlation has a pseudorandom, 511-bit pattern of openings that greatly increases signal-to-noise ratios of TOF measurements, while approximately halving the resolution compared to single-shot. The chopper is spun by a motor (Globe Motors, 75A1003-2) that is attached to the wheel with high-vacuum bearings (Barden Precision Bearings, SR4SSTA5). The motor is powered by AC voltage from a function generator (Stanford Research Systems, DS335) that is amplified by a stereo amplifier (Bogen, GS150), resulting in chopper wheel speeds of 7–200 Hz. TOF timing is initiated by a light pulse from an LED source that passes through triggering slots in the chopper and is sensed by a photon detector, after which it is converted into a TTL pulse and triggers the multichannel scaler (MCS) and successive counting electronics described in Section 2.4.4.

The beam enters the second differential stage through the first collimating aperture of the instrument, labeled Aperture 1 in Figure 2.3—a complete list of aperture dimensions and placements are given in Table 2.2. This stage is pumped by a 135 L/s diffusion pump (Edwards,

Aperture	Aperture Size	Distance from Chopper
Nozzle	15 μm	-13.81 cm
Skimmer	0.5 mm	-12.81 cm
Chopper	Variable	0
Aperture 1	0.89 mm	2.66 cm
Aperture 2	1.93 mm	22.35 cm
Sample	~4 mm	49.96 cm
Aperture 3	4.45 mm	76.88 cm
Aperture 4	5.56 mm	95.88 cm
Aperture 5	5.79 mm	103.36 cm
Ionizer Entrance Plate	6.35 mm	105.97 cm
Filament	N/A	107.01 cm

Table 2.2: HAS instrument aperture sizes and distances from the chopper; aperture names correspond with labels in Figure 2.3.

Diffstak 63) backed by the same rotary vane pump used for the first differential stage. After passing through all three beamline regions, the He beam finally enters the scattering chamber through a second aperture and a manual gate valve (Aperture 2 in Figure 2.3). The first two apertures collimate the incident beam to a 0.22° angular spread that results in an approximately 4 mm diameter beam spot size on the crystal.

2.4.3 Scattering Chamber

The scattering chamber is a UHV bell jar with a differentially pumped, rotatable lid. The sample is mounted on a manipulator that rotates with the lid and can be positioned for low energy electron diffraction (LEED), Auger electron spectroscopy (AES) and crystal sputtering, or He scattering experiments. Vacuum conditions are maintained primarily by a 2400 L/s diffusion pump

(Varian, VHS-6) backed by a 24 m^3/h rotary vane pump (Pfeiffer, Duo20M), with a 10 in right-angle, pneumatic solenoid valve separating the vacuum chamber from these pumps. Above the diffusion oil pump and separating it from the right-angle valve is a baffle system cooled by a Freon refrigerator (Polycold, PCT-200). Additionally, there is a 60 L/s ion pump (Perkin-Elmer, 2106035), within the bell jar on the high-vacuum side of the right-angle valve, that maintains vacuum conditions if the right-angle valve closes. The ion pump has filaments for titanium sublimation pumping to lower the base chamber pressure. The valve is interlocked with the scattering chamber pressure; diffusion pump temperature, waterline flow, and power; foreline pressure; and baffle temperature—the valve will close if any setpoint is tripped, protecting the chamber from potential exposure to the foreline or pump oil. The sample cooling system, discussed later, further improves vacuum conditions through cryopumping.

The lid of the bell jar rests on three concentric, MoS_2-coated Teflon spring seals (St. Gobain) that form two separate pumping regions: the inner lid and the outer lid. The inner lid is closest to the bell jar and is pumped by a 10 L/s ion pump (Gamma, TiTan); the outer lid is pumped by a 12 m^3/h rotary vane pump (Pfeiffer, Duo10M). After the chamber is vented, the inner lid first is brought to rough vacuum ($\sim 10^{-5}$ Torr) by a sorption pump before the ion pump is turned on.

The Nb(100) crystal, described later, is mounted on a six-axis manipulator (Vacuum Generators, HPT2) that precisely controls translation along the x-, y-, and z-axes, rotation in the polar (θ) and azimuthal (ϕ) directions, and tilt (χ) orientation. The manipulator is offset 5 cm from the center of the lid and, for a specific lid position, aligns with the geometric scattering center of the instrument. The crystal can be cooled to temperatures of ~230 K by a closed-cycle He refrigerator (Advanced Research Systems, DE-202P). The second stage of the refrigerator connects to an OFHC Cu bar, which is attached to a Cu braid with a sapphire/In joint. The braid

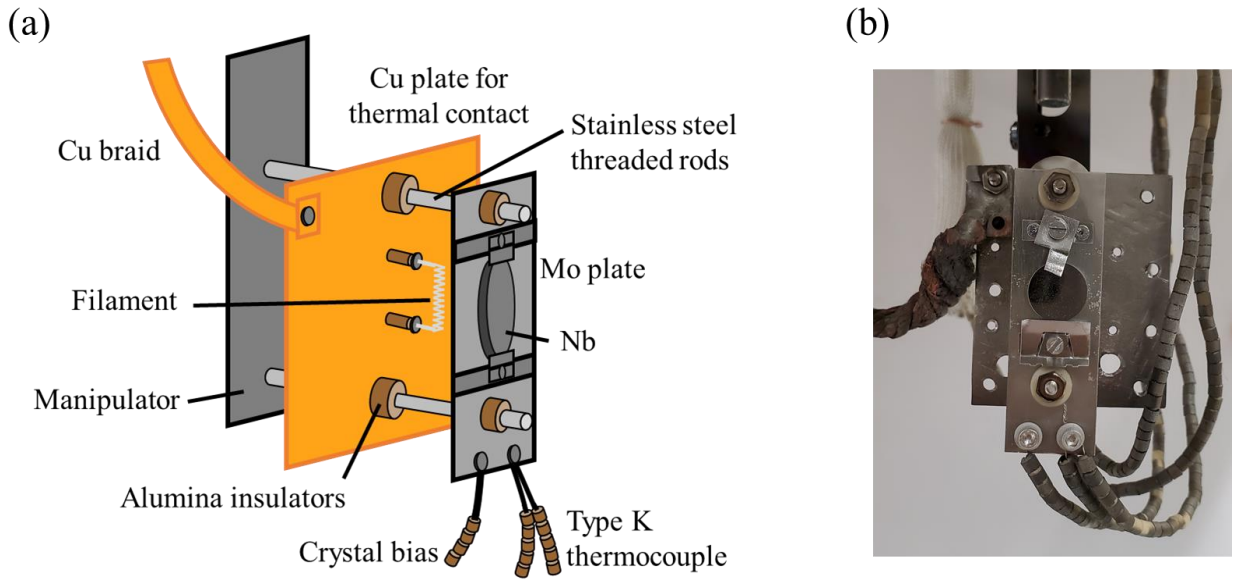

Figure 2.4: (a) Schematic of crystal mounting system viewed from the side; (b) head-on picture of Nb(100) crystal installed on the mount.

connects to an OFHC Cu plate behind the crystal. In order to reach the extreme high temperatures needed to prepare Nb, a new heating and crystal mounting system was designed and built; it is illustrated in Figure 2.4(a) and shown in Figure 2.4(b). The crystal is mounted on a Mo plate with Mo clips and screws which originally were part of a commercial mount (Vacuum Generators). The Cu and Mo plates are attached to the manipulator via stainless-steel threaded rods that pass through alumina (Al_2O_3) bushings, for both thermal and electrical separation. The crystal is heated by an electron-beam (e-beam) system that uses a 1%-thoriated W filament, made from coiled 0.25 mm diameter wire fixed to threaded Mo rods with Mo nuts (Kimball Physics). These rods are run through the Cu plate and attached to Cu leads. Alumina bushings separate the rods from the Cu plate and allow one end of the filament to float electrically while the other end is grounded. Filament current is controlled with a 0–10 A power supply (BK Precision, 1687B) that is attached to a vacuum feedthrough that connects to the Cu leads. For an e-beam heating system to work, the crystal must be at a positive voltage relative to the filament, so electrons emitted from the filament

are drawn towards and strike the crystal. A hole was drilled through the Mo plate immediately behind the crystal, giving the filament line-of-sight access to the back of the crystal.

The Mo plate is separated from the stainless-steel mounting rods by alumina bushings, which allow the plate and crystal to float electrically. A 0.5 mm, Cu-Mn-Ni alloy bias wire (Alfa Aesar) is attached to the bottom of the Mo plate with stainless-steel screws and nuts and runs to a BNC feedthrough in the bell jar lid, which connects to a 0–600 V power supply (Sorensen, XG 600-1.4) and provides the necessary voltage difference between the filament and crystal. During experiments, the crystal temperature is monitored by a type-K thermocouple (Omega Engineering) attached to the bottom of the Mo plate, near the bias wire, with stainless-steel screws and nuts. The leads for the filament, bias wire, and thermocouple are threaded through alumina beads to insure physical and electrical separation.

Since the Mo plate is floating electrically at 0–600 V from ground, the voltage difference across the thermocouple leads is converted first by a signal conditioner (Automation Direct, FC-T1) before it is sent to a PID controller (Eurotherm, 2404). The temperature gradient between the center of the crystal and the thermocouple is moderate at crystal temperatures below ~700 K, but becomes extreme when the crystal is above 1400 K. The temperature of the thermocouple was calibrated to the crystal for temperatures at or below 1400 K by rotating the lid of the bell jar until the crystal was visible through a window, and then using a pyrometer (Advanced Energy, LumaSense IGA 140, MB25L, 350–2500°C) to compare the temperature of the crystal measured by the pyrometer to that measured by the thermocouple. During crystal preparation, when temperatures are above 1400 K, the temperature is monitored by the pyrometer and controlled by the crystal bias voltage, which is attached to the same Eurotherm PID controller and stable within ±1–5 K, depending on the temperature used. In this configuration, the filament current is

controlled manually and varied between 0–6 A. During experiments, the crystal temperature is monitored by the calibrated thermocouple and controlled by the filament current attached to the Eurotherm controller, while the crystal bias is controlled manually and varied between 0–600 V. When controlled through the thermocouple, crystal temperatures are stable within ± 1 K. A custom-made LabVIEW^{TM} (National Instruments, LabVIEW^{TM} 2015) software program is used to interface with the Eurotherm controller.

Crystal preparation is made possible by traditional surface analysis equipment that is mounted in the bell jar and accessed by rotating the bell jar lid. Crystal structure and azimuthal orientation are confirmed by a reverse-view low-energy electron diffraction (LEED) using an integral electron gun (Princeton Research Instruments, RV-8-120). Surface quality and composition is analyzed by Auger electron spectroscopy (AES), with an offset electron gun (Phi, 04-015) and a double-pass cylindrical mirror precision electron energy analyzer (Phi, 15-255). Crystal cleaning is facilitated by a sputter gun (Phi, 04-191) positioned near the AES analyzer, which sputters the crystal with ions when the chamber is back-filled with Ne gas through a UHV leak valve (Duniway, 9069). Chamber partial pressures are monitored with a residual gas analyzer (RGA) (Extrel, RGA300M).

During He scattering experiments, a He beam enters the scattering chamber from the beamline. It then reflects off the crystal and passes into the detector. The scattering chamber is separated from the detector by a custom-built UHV bellows and a hand-operated gate valve. Pressure is monitored by an ion gauge (Varian, UHV-24) and reaches base values of 3×10^{-10} Torr after the chamber has been baked.

2.4.4 Rotatable Detector

The He atom enters the first stage of the detector's differential pumping through a collimating aperture (Aperture 3 in Figure 2.3). This region is connected to a 135 L/s diffusion oil pump (Edwards, Diffstak 63)—backed by a 12 m^3/h rotary vane pump (Pfeiffer, Duo10M) common to the entire detector—by a pneumatic gate valve and liquid N_2-filled baffle trapping system. Additionally, there is a UHV leak valve (Varian, 951-5106) installed in this region that is useful for calibration and troubleshooting the detector. After passing through Aperture 4 (Figure 2.3), the scattered He atom enters the second stage of differential pumping, which houses the ionizer and Aperture 5 (Figure 2.3). This stage is pumped by a 200 L/s turbo pump (Pfeiffer, TPU-170) backed by a 135 L/s diffusion oil pump (Edwards, Diffstak 63) and the rotary vane pump. The third stage of the detector contains the quadrupole and is pumped by a 280 L/s diffusion oil pump (Edwards, Diffstak 100) backed by the rotary vane pump, which is connected to the vacuum region by a pneumatic gate valve and liquid N_2-filled trap. The gate valves in both the first and third stages of the detector are kept closed unless scattering experiments are in progress; when these valves are closed, vacuum is maintained by the turbo pump in the ionizer region. The base pressure of the detector after it has been baked, as measured by an ion gauge (Varian, UHV-24) in the ionizer region, reaches 1×10^{-10} Torr when both gate valves are open.

The detection system consists of an axial ionizer (Extrel, 041-1), ion optics, a quadrupole mass spectrometer (QMS) rod assembly (Extrel, 7-324-9), and an off-axis channeltron electron multiplier (Photonis, 4816). He is ionized by electron bombardment from a hot, 0.005" diameter, 1%-thoriated W filament with typical emission currents of 11 mA. Electrons are focused on the He beam path by a grid biased relative to the ionizer plate; typical settings for the grid and other optics, optimized for He ions, are listed in Table 2.3. He ions are extracted, accelerated, and

Detector Parameter	Setting
Ionizer	11 mA
Ion Energy	57 V
Electron Energy	191 V
Extractor	12 V
Lens 1	15 V
Lens 2	16 V
ELFS Plate	137 V
Electron Multiplier	2900 V

Table 2.3: Operating currents and voltages for the ionizer, ion optics, and QMS.

focused into the quadrupole entrance by two electrostatic lenses. Radiofrequency and DC voltages are applied across the quadrupole rods—which filter incident atoms based on mass-to-charge ratios—by a power supply (Extrel, QPS50) that interfaces with LabVIEW^{TM} software through a USB data acquisition (DAQ) device (National Instruments, USB-6001). The filtered He ions are detected by the electron multiplier, which converts the ions into pulses that are between 5–15 mV in height and approximately 5 ns wide. These pulses are sent through a 200× fast preamplifier (Ortec, VT120A) before traversing a cable to the counting electronics. The pulses then pass through an amplifier and discriminator (Phillips Scientific, 771 quad bipolar amplifier with six-channel discriminator), which removes unwanted background signal and converts the raw pulses to NIM pulses that are 1.6 V tall and 50 ns wide. A custom-built multichannel scalar converts the NIM pulses to TTL and counts the TTL pulses; it is timed by a custom-built CAMAC. The CAMAC is triggered by the chopper and controlled by LabVIEW^{TM} software through a GPIB interface (LeCroy 8901A).

The entire detector sits on a turntable that rotates through a manual- or computer-controlled motor and gear assembly. The angular range of the detector is 38° and is decoupled from the polar angle of the sample manipulator: the detector can be scanned across a wide range of final scattering angles for each incident scattering angle. LabVIEW^{TM} software is used to interface with the motor through an optical encoder and an up-down counter, and the detector rotates with 0.1° precision. The overall angular resolution of the instrument, from the chopper to the multiplier, is FWHM = 0.45°, while the total flight path is approximately 1 m.

2.4.5 Crystal Preparation and Typical Experimental Parameters

The 10 mm diameter, 2 mm thick Nb(100) crystal was purchased from Surface Preparation Laboratory (Netherlands, 99.99% purity, ∼0.1° cut accuracy). As determined by AES, primary initial crystal contaminates were C, B, and S. To remove these contaminates, the crystal was repeatedly annealed at and flashed to ∼1900 K, with 500 eV Ne^+ used to sputter impurities from the surface ($P_{Ne} \sim 5.5 \times 10^{-5}$ Torr, 3 μA maximum emission). Cycles of annealing, flashing, and sputtering were conducted until the crystal could be annealed at 1800 K for at least 2 hours without impurities rising to the surface. Surface order was checked with LEED; an example LEED spectrum is shown in Figure 2.5. As will be reported in the next chapter, Nb(100) forms a (3 × 1)-O superlattice structure, which is visible in the LEED spectrum along both directions due to 90°-rotated domains.

Diffraction scans in Chapters 3 and 4 were obtained by sweeping the detector arm while keeping the incident angle and energy fixed. The detector was stopped every 0.2° for data collection, which typically lasted for 5 seconds at each angle. The square-wave chopping pattern resulted in open and closed (background) signal channels; diffraction scans display the summed

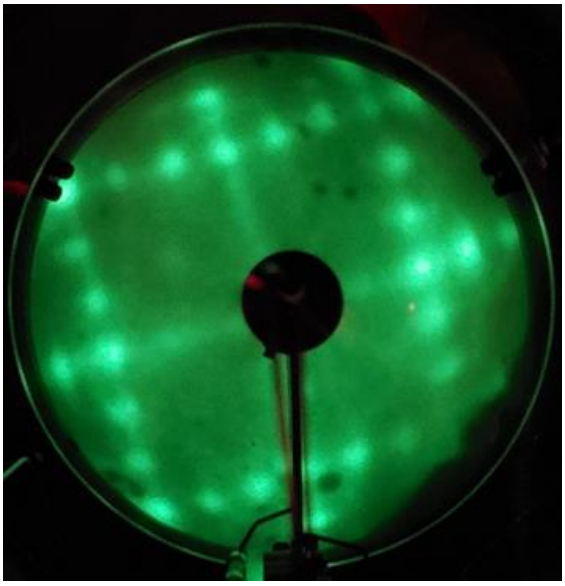

Figure 2.5: Example LEED spectrum of the (3 × 1)-O Nb(100) surface.

intensity from the open channel with the background channel intensity subtracted out. The incident scattering angle, θ_i, is the average of the detector angle, θ_{det}, at specular and the instrument's included angle, θ_{inc}, which depends on the lateral alignment of the detector ($\theta_{inc} = 54.3°$ for these experiments). The final angle, θ_f, is determined through the relationship: $\theta_f = \theta_{det} - \theta_i + \theta_{inc}$. Each scan initially is recorded as a function of scattered intensity vs. θ_{det}, which can be converted to scattered intensity vs. ΔK through Equation 2.15, where k_i is determined by an elastic TOF spectrum and Equation 2.16.

TOF spectra were taken with either the single-shot or cross-correlation chopper modes. For single-shot experiments, the chopper wheel rotated at 200 Hz with 4 μs channel times, while for cross-correlation experiments, the chopper wheel rotated at approximately 196 Hz with 10 μs channel times. The length of each scan was dependent on the intensity levels seen at the given incident and final conditions. Typically, spectra were saved every 20–60 min and added until the desired signal-to-noise ratio was obtained. The arrival times of elastic peaks were used to

determine the incident beam energy. Inelastic peak times were converted to phonon energies and wavevectors through Equations 2.26-27.

Chapter 3

Persistence of the Nb(100) Surface Oxide Reconstruction at Elevated Temperatures

Helium atom scattering and Auger electron spectroscopy (AES) are used to characterize the (3 × 1)-O reconstruction of the Nb(100) surface at elevated temperatures. Persistent helium diffraction peaks and specular lineshape analysis indicate that the oxide structure persists, apparently unchanged, until surface temperatures of at least 1130 K. In a complementary experiment, AES oxygen to niobium ratios for the Nb(100) oxide show little to no change when the surface temperature is varied from 300 K to 1150 K. These data inform future development of superconducting radio frequency (SRF) cavities. In particular, these findings demonstrate the important role that persistent niobium oxides will play in the optimization of thin film growth strategies and coating procedures for Nb_3Sn and other next-generation SRF superconducting alloy materials.

3.1 Introduction

Niobium has become the material of choice for modern superconducting radio frequency (SRF) cavities in particle accelerators. Its low surface resistance (R_S), high critical temperature (T_C), and relatively high cavity quality (Q) factor at large fields all have contributed to its successful utilization in SRF cavities.[7,19–21] In addition, pure Nb is relatively soft and ductile, which allows it to be formed and welded into the cavity geometries required to optimize Q factors and accelerating gradients.[19] Extensive research has been performed on these cavities and enables them to operate close to the fundamental limits of Nb.[5,7,21–25] Future progress, then, rests on the

development of new materials: one of the most promising options is Nb_3Sn. Theoretical and experimental advances show that Nb_3Sn cavities could yield higher Q factors with larger accelerating gradients at higher operational temperatures than traditional Nb cavities,[26–31] improving performance while also greatly reducing the cost of infrastructure and cryogens.

Unlike Nb, there are substantial issues associated with making cavities from Nb_3Sn.[7] While its brittle nature and poor thermal conductivity prevent it from being fashioned into a cavity directly, thin Nb_3Sn coatings formed on Nb cavities have shown promising results.[7,32] This process typically involves coating an existing Nb cavity with Sn and then annealing at high temperatures to form the Nb_3Sn thin film at or near the surface.[5,33] Research into the microscopic formation of these thin films is necessary for the advancement of SRF technology.

One complication present in the growth of Nb_3Sn thin films is the role of Nb's native oxide layer. Nb is highly reactive to O and its surface usually is covered by one of many possible oxide structures, both in air and in vacuum.[34,35] The O exposures required to reach these different oxide structures, as well as the structures themselves, have been well characterized.[34–38] Generally, a thick, insulating Nb_2O_5 layer dominates the surface in air, while thin, ordered $(n \times 1)$-O domains ("ladders") form readily on a Nb(100) surface after high-temperature annealing in vacuum.[36,39–41] As a refractory metal, Nb has a high melting temperature of 2741 K.[42] The O in Nb starts to desorb as NbO and NbO_2[43,44] above 1900 K[34] in ultra-high vacuum (UHV), and it is not until Nb is heated above 2500 K that pure, clean, O-free Nb is seen.[34,43–47] The extreme temperatures needed to remove O mean that the Nb SRF cavities are coated in an oxide layer, and that the Sn deposited to form Nb_3Sn is deposited on one of many Nb oxides. The growth morphology of Nb_3Sn on Nb is dependent on the interaction of Sn with the oxide layer. Thus, a complete, temperature-dependent, microscopic understanding of the Nb oxide surface is critical to the development of consistent,

well-formed Nb_3Sn thin films. Such an understanding will allow for the development of alloy growth procedures with improved overall quality, homogeneity, and stoichiometry, enhancing critical operational SRF characteristics in high fields.

A key, missing factor in the literature is the nature of the Nb oxide surface at elevated temperatures. Up until now, studies have been limited to analyses at or below room temperature: thermal history and desorption temperatures are known, but the structure and stoichiometry at high temperatures has not been elaborated. In Nb_3Sn SRF cavity fabrication processes, the Nb surface temperature is elevated during Sn nucleation, annealing, and degassing.[5,7,33] An understanding of the Nb oxide surface at elevated temperatures will guide current and new routes for improved Nb_3Sn cavity production. To our knowledge, this combined helium atom scattering (HAS) and Auger electron spectroscopy (AES) study represents the first investigation of the Nb(100) oxide ladder structures at elevated temperatures, and it is one of the few in-situ studies of metal oxide structures at high temperatures.

HAS is a unique, nondestructive, surface-sensitive technique that elucidates surface structure and dynamics.[8] The He atoms are neutral probes that scatter off the electron cloud a few angstroms away from the surface: the surface is not damaged in any way.[3,4,18] HAS is particularly suited for examining surface structure at elevated temperatures. Unlike in typical low-energy electron diffraction (LEED), where electron bombardment heating presents experimental challenges, the neutral He probe is not affected by the high voltages required for electron bombardment. Scanning tunneling microscopy (STM) also becomes very difficult at extremely high sample temperatures, due to atomic thermal fluctuations and instrument instability.[48] Debye-Waller attenuation of scattered He does become increasingly more important at elevated surface temperatures,[4] but if the crystal is sufficiently reflective, diffracted He signal can be seen above

the diffuse scattering background and the surface structure obtained.

3.2 Experimental

3.2.1 Helium Atom Scattering—Methods and Sample Preparation

The surface structure of Nb(100) was characterized with a UHV HAS apparatus that has high momentum and energy resolution. The apparatus is described elsewhere and in Chapter 2 of this thesis.[49] We prepared the Nb(100) crystal, obtained from Surface Preparation Laboratory (Netherlands, 99.99% purity, ∼0.1° cut accuracy), according to the procedure detailed in Chapter 2, which included annealing, flashing, and sputtering. Flashes to 1300 K were performed before experiments to remove any trace adsorbates from the crystal surface. For these experiments, the incident He beam was held at 21 meV ($k_i = 6.3$ Å^{-1} and $T_n = 96.7$ K) so that the specular, first-order primitive, and (3 × 1)-O superlattice diffraction peaks could be observed in the same angular distribution.

3.2.2 Auger Electron Spectroscopy—Methods and Sample Preparation

AES measurements of Nb(100) from Surface Preparation Laboratory (Netherlands, 99.99% purity, ∼0.1° cut accuracy) were performed in a UHV experimental system composed of a scanning tunneling microscopy chamber (UHV VT–STM, RHK Technology) and a preparation chamber equipped with AES capabilities, as previously described.[39] The Nb(100) crystal was cleaned via repeated cycles of Ar^+ ion sputtering and electron bombardment annealing at a sample temperature (T_S) of approximately 2100 K, as measured using a Mikron Infrared (MG-140) pyrometer. Surface cleanliness was confirmed by AES and STM analyses, which showed the characteristic (3 × 1)-O superlattice with no surface contaminants.[36,39,50]

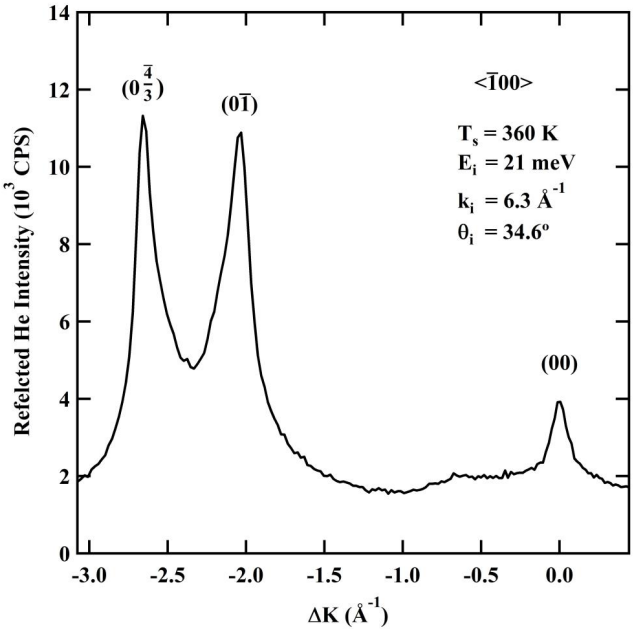

Figure 3.1: Representative diffraction spectrum for He on (3 × 1)-O Nb(100) along the <$\bar{1}$00> symmetry axis as a function of parallel momentum exchange.

3.3 Results and Discussion

3.3.1 Helium Diffraction

After preparation in vacuum, the Nb(100) surface reconstructs into a (3 × 1)-O ladder structure, as observed elsewhere.[39] Figure 3.1 shows an angular distribution of He back-scattered from the (3 × 1)-O Nb(100) surface along the <$\bar{1}$00>, $\overline{\Gamma X}$ azimuthal direction. The diffraction spectrum was taken at a surface temperature of 360 K with an incident angle of $\theta_i = 34.6°$. The reproducibility of the surface was confirmed through repeated scans at $T_S = 360$ K after flashing the crystal to 1300 K. Three diffraction peaks are resolved clearly: a zeroth-order specular peak ($\theta_i = \theta_f$) at $\Delta K = 0$ Å^{-1}, a first-order, $(0\bar{1})$ diffraction peak at ΔK = -2.0 Å^{-1} (θ_f = 14.2°), and a (3 × 1)-O superlattice, $\left(0\frac{\bar{4}}{3}\right)$ diffraction peak at ΔK = -2.7 Å^{-1} ($\theta_f = 8.5°$). These elastic diffraction peaks arise when the requirements for Bragg diffraction are satisfied, such that

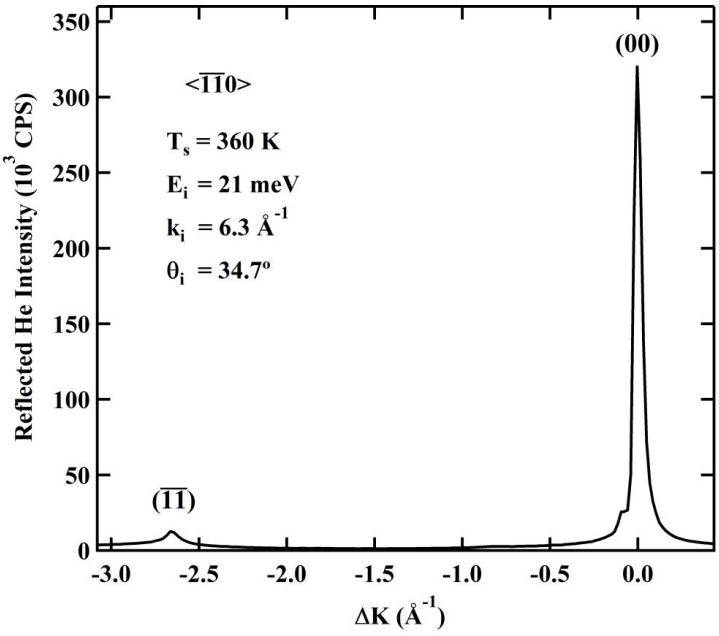

Figure 3.2: Representative diffraction spectrum for He on (3 × 1)-O Nb(100) along the <$\overline{1}$10> symmetry axis as a function of parallel momentum exchange.

$$\Delta K = k_i(\sin\theta_i - \sin\theta_f) = G_{mn}, \tag{3.1}$$

where ΔK is the change in the surface-parallel component of the He wavevector k_i; θ_i and θ_f, respectively, are the initial and final scattering angles relative to the surface normal; and G_{mn} is a linear combination of surface reciprocal lattice vectors. From the first-order, $(0\overline{1})$ diffraction peak, the Nb-Nb lattice spacing was determined to be 3.08 $\pm$ 0.01 Å, which corresponds favorably to surface lattice constants found through LEED measurements.[36] The diffraction peak at ΔK = -2.7 Å^{-1} was identified as (3 × 1)-O superlattice peak, since its ΔK value is approximately $\frac{4}{3}$ times that of the $(0\overline{1})$, primitive peak. This also aligns with previous LEED studies that show the (3 × 1)-O superlattice structure.[36] The intensities of both the $(0\overline{1})$ and $\left(0\frac{\overline{4}}{3}\right)$ peaks are far greater than that of the specular peak, which is in contrast to HAS from the bare Nb(100) surface and suggests an increase in surface corrugation as a result of the ladder structure.[47,51]

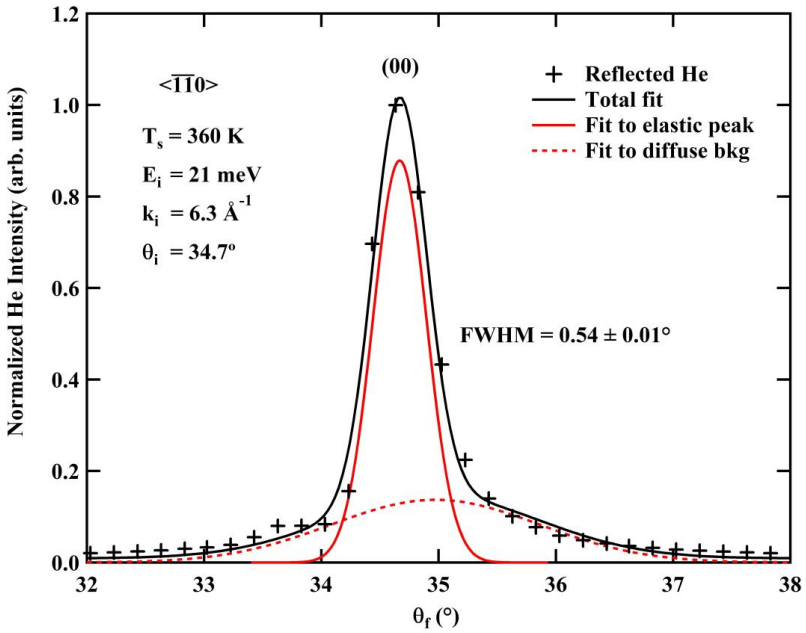

Figure 3.3: Width analysis of a specular ($\theta_i = \theta_f$) He diffraction peak on (3 × 1)-O Nb(100) along the <$\bar{1}$10> symmetry axis, plotted vs. final scattered angle (θ_f). The solid red line is a Gaussian fit to the coherent elastic peak, the dashed red line is a Gaussian fit to the diffuse elastic and multiphonon background, and the solid black line is the overall fit to the data (black crosses). The narrow, coherent elastic peak (solid red line) has a FWHM of 0.54 $\pm$ 0.01°.

The angular distribution of the <$\bar{1}$10>, $\overline{\Gamma M}$ azimuthal direction was determined and is shown in Figure 3.2 at T_S = 360 K. In this direction, the specular peak is far more intense than in the <$\bar{1}$00> direction, indicating less surface corrugation. The small, secondary specular peak can be attributed to surface faceting from the anneal process and was ignored in analysis.[47] The peak at ΔK = -2.7 Å^{-1} corresponds to the $(\bar{1}1)$ diffraction peak.

The high intensity of the specular peak in the <$\bar{1}$10> direction allowed us to analyze the peak lineshape with minimal contributions from the diffuse elastic and multiphonon background seen in the <$\bar{1}$00> direction. The He beam strikes the surface with a 4 mm spot size, averaging over many atomically flat terraces. The average width of these terraces has been shown to be

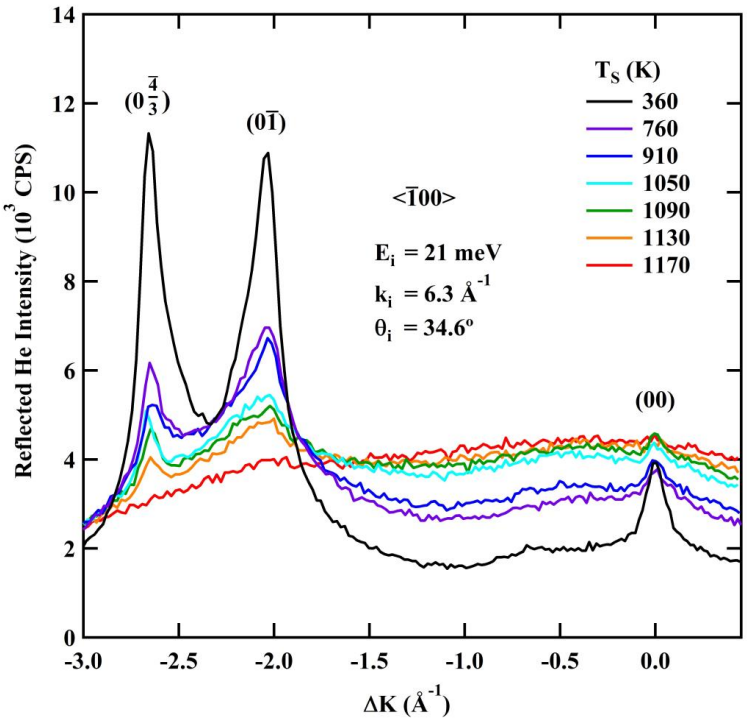

Figure 3.4: Decay of diffraction spectra for He on (3 × 1)-O Nb(100) along the <$\bar{1}$00> symmetry axis as a function of surface temperature, plotted vs. parallel momentum exchange.

approximately equal to the coherence length, l_c.[15,52] The specular peak broadening from the average domain size, $\Delta\theta_w$, can be found through a deconvolution of the measured specular peak full width half maximum (FWHM), $\Delta\theta_{exp}$, and the instrument function broadening, $\Delta\theta_{inst}$:

$$\Delta\theta_w^2 = \Delta\theta_{exp}^2 - \Delta\theta_{inst}^2. \tag{3.2}$$

The coherence length then can be determined through the equation,[52]

$$l_c = \frac{5.54}{\Delta\theta_w k_i \cos(\theta_f)}. \tag{3.3}$$

Figure 3.3 shows the fitting function used to determine the width of the specular peak. The normalized peak was fit with one sharp Gaussian function for the coherent elastic signal and one broad Gaussian for the diffuse elastic and multiphonon background signal.[53] With an overall instrument resolution of 0.45° and a measured specular FWHM of 0.54 ± 0.01°, the average

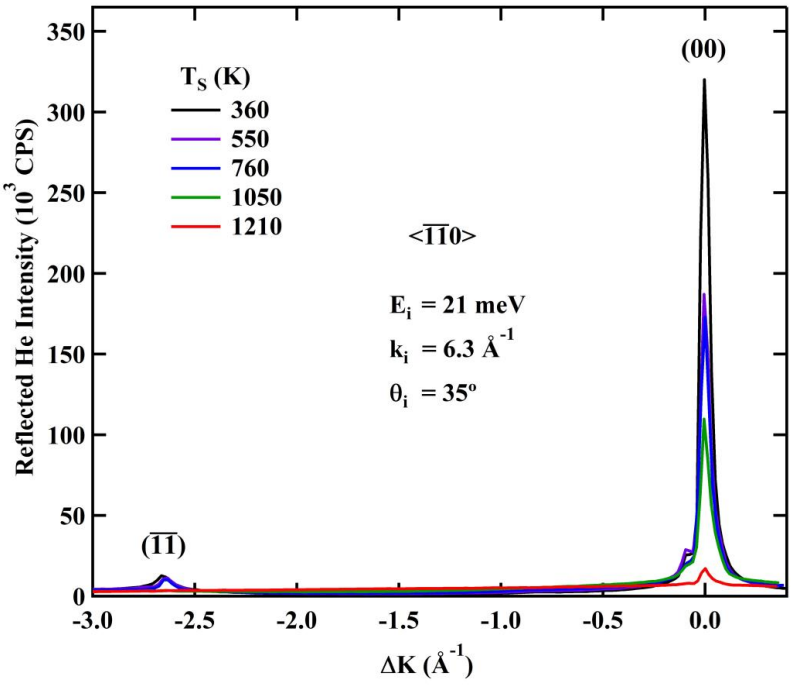

Figure 3.5: Decay of diffraction spectra for He on (3 × 1)-O Nb(100) along the <$\bar{1}\bar{1}$0> symmetry axis as a function of surface temperature, plotted vs. parallel momentum exchange.

domain size was found to be 210 ± 10 Å.

Diffraction spectra in the <$\bar{1}$00> direction, as a function of increasing temperature, are shown in Figure 3.4. Surface stability at each temperature was determined by immediately repeating each scan; the identical scans indicated that the surface structure was unchanging. While the specular peak is enveloped by the background at around 1053 K, the $(0\bar{1})$ and $\left(0\frac{\bar{4}}{3}\right)$ diffraction peaks are visible up to at least 1130 K. At 1170 K, the peak intensities are lower than the detected background.

Temperature dependent spectra in the <$\bar{1}\bar{1}$0> direction are shown in Figure 3.5. Spectra were recorded as a function of increasing temperature, except for the spectrum taken at 550 K, which was taken after a 1900 K flash. The specular intensities at five different surface temperatures

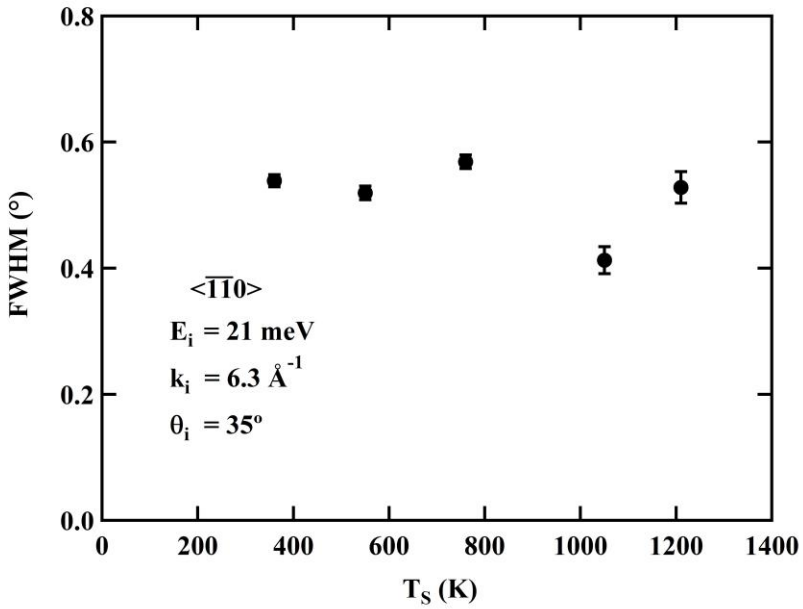

Figure 3.6: FWHM of Gaussian fits to the coherent elastic portion of specular ($\theta_i = \theta_f$) He diffraction peaks on (3 × 1)-O Nb(100) along the <$\overline{1}$10> symmetry axis, plotted vs. surface temperature. All peaks were fit with two Gaussians, as illustrated in Figure 3.3.

were fit in a manner similar to that shown in Figure 3.3, and the FWHM of each coherent elastic peak is shown in Figure 3.6. HAS lineshapes are very sensitive to surface disorder;[4,51] any O dissolution or disorder caused by the elevated temperatures would increase dramatically the width of the specular peak. Instead, the width stays nearly constant as a function of surface temperature up to 1210 K, as seen in Figure 3.6. This, in addition to the existence of the superlattice diffraction peak in Figure 3.4 at 1130 K, indicate that the (3 × 1)-O superlattice remains unchanged on the Nb(100) surface up to at least 1130 K, and presumably up to at least 1210 K.

3.3.2 Auger Electron Spectroscopy

A second Nb(100) single crystal was prepared in a separate UHV experimental system, which resulted in the (3 × 1)-O superlattice structure.[39,54] In order to determine the concentration

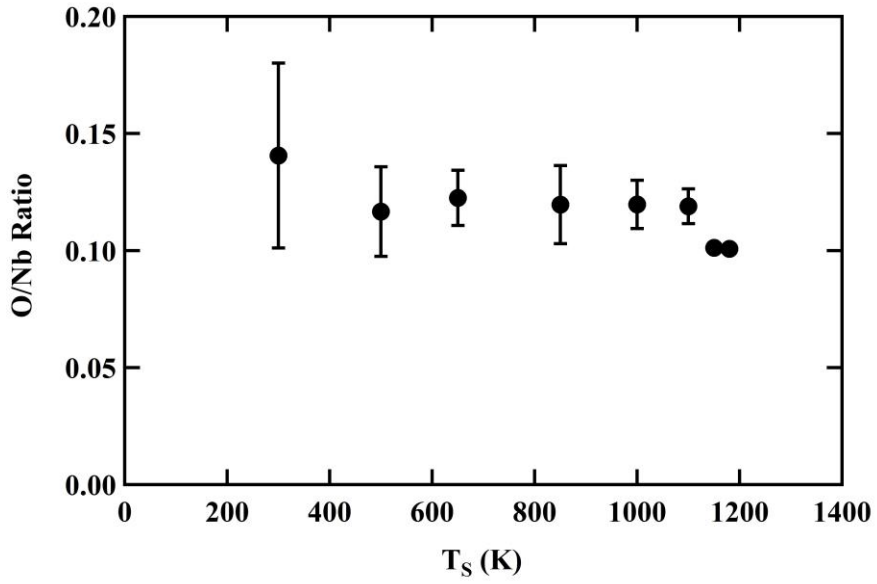

Figure 3.7: O/Nb AES ratios taken at T_s between 300 K and 1150 K. There is no significant decrease in O content on Nb(100) below 1200 K.

of surface O on Nb(100) at elevated temperatures, a ratio of the peak-to-peak intensities of the principle O and Nb peaks were obtained at 519 eV and 169 eV, respectively,[55] for T_S ranging from 300 K to 1150 K. The O/Nb ratios displayed in Figure 3.7, plotted as a function of T_S, quantitatively describe the surface composition at elevated surface temperatures; the displayed error bars account for varying near-surface and surface oxide contributions.

Across the entire temperature range studied in this work, the O/Nb ratio is stable, providing evidence for a constant surface O concentration up to 1150 K. The near surface does not lose O from the thermal annealing,[39] even though the subsurface O content may vary due to the cleaning procedure and the amount of O in the bulk, as seen by slight fluctuations in the O/Nb ratio at T_S = 300 K. The average measured Auger peak intensities did not change as a function of primary beam exposure time, indicating that the AES experiments did not modify the surface elemental composition over the course of data collection. Furthermore, the Nb(100) surface was analyzed by in-situ, room temperature STM following the AES measurements. The STM work confirmed that

the surface remained covered by the characteristic (3 × 1)-O superlattice and that the sample was not damaged by the high temperature AES measurements. Residual gas analyzer spectra indicated that the oxide did not desorb within the studied temperature range, so any observed reduction in the O/Nb ratio would be a result of O dissolution into the bulk crystal. However, based on the AES O/Nb ratios detailed in Figure 3.7, there is no evidence of appreciable O dissolution below 1200 K. This AES analysis confirms the HAS measurements that show no appreciable O dissolution or disorder within the T_S range studied.

3.4 Conclusion

He atom scattering and Auger electron spectroscopy provide evidence for the continued existence of a (3 × 1)-O ladder structure on the Nb(100) surface until at least 1130 K and, to our knowledge, this work is the first investigation of the Nb oxide surface at elevated temperatures. He diffraction peaks from the oxide structure were persistent until 1130 K, and the specular peak lineshapes indicated little to no surface disorder up to 1210 K. The constant AES O to Nb peak ratios of Nb(100) also indicated that O did not leave the surface either through dissolution or evaporation until above at least 1200 K, consistent with previous studies.[34,36] The unvaried oxide reconstruction at the investigated high temperatures informs future SRF cavity research and development. The next-generation method of coating Nb cavities with a thin film of Nb_3Sn involves an initial nucleation step where the surface is held at about 770 K,[7] below the 1130 K temperature measured here. Our research shows that Sn is nucleating on an oxide, not on bare Nb. This further illuminates the role of O in the Sn deposition and cavity optimization processes. The oxide structure above 1130 K, including at approximately 1375 K[7] where the Sn-coated cavities are annealed, is still unknown, and would bring similarly interesting information to the discussion

on SRF cavity production. Additional unanswered questions include Sn mobility and long-term stability, the mechanisms and kinetics for Sn incorporation into the Nb substrate, and the development of Nb_3Sn alloy materials with lower defect concentrations and higher chemical and spatial uniformity. These questions need to be addressed to realize the SRF community's ambitious goal to successfully implement this promising alloy in next-generation accelerator applications.

Chapter 4

A Combined Helium Atom Scattering and Density-Functional Theory Study of the Nb(100) Surface Oxide Reconstruction: Vibrational Dynamics and Phonon Band Structures

Helium atom scattering (HAS) and density-functional theory (DFT) are used to characterize the phonon band structure of the (3 × 1)-O surface reconstruction of Nb(100). Innovative DFT calculations comparing surface phonons of bare Nb(100) to those of the oxide surface show increased resonances for the oxide, especially at higher energies. Calculated dispersion curves align well with experimental results and yield atomic displacements to characterize polarizations. Inelastic helium time-of-flight measurements show phonons with mixed longitudinal and shear-vertical displacements along both the $<\bar{1}00>$, $\overline{\Gamma X}$ and $<\overline{11}0>$, $\overline{\Gamma M}$ symmetry axes over the entire first surface Brillouin zone. Force constants calculated for bulk Nb, Nb(100), and the (3 × 1)-O Nb(100) reconstruction indicate much stronger responses from the oxide surface, particularly for the top few layers of niobium and oxygen atoms. Many of the strengthened bonds at the surface create the characteristic ladder structure, which passivates and stabilizes the surface. These results represent, to our knowledge, the first phonon dispersion data for the oxide surface and the first ab initio calculation of the oxide's surface phonons. This study supplies critical information for the further development of advanced materials for superconducting radiofrequency cavities.

4.1 Introduction

Particle accelerators are used in a wide range of disciplines, including high-energy particle physics, chemistry, free-electron laser (FEL) science, and materials science, as well as in medical and industrial applications.[6,24] High-energy accelerators propagate large, radiofrequency (RF) electromagnetic fields within superconducting RF (SRF) cavities to generate and control beams of charged particles.[56] These RF fields, however, only penetrate through the first ~100 nm of the cavity surface: SRF cavity performance is controlled by the chemistry and quality of the surface.[21] To lower RF surface resistance (R_s), minimize power loss, and optimize performance, the surface preparation of the SRF cavity must be designed and implemented carefully.

Oxidized Nb surfaces are the current industry standard for SRF cavities. Nb has the highest critical temperature of elemental superconductors ($T_c = 9.3$ K) and has low RF surface resistance at operating temperatures of about 2 K.[7,19,25,57] Additionally, Nb is thermally conductive and malleable; it can be cooled effectively and formed into SRF cavity shapes.[19,58] High-energy particle accelerator facilities, such as those at Fermi National Accelerator Lab and the European Council for Nuclear Research (CERN), require a large series of SRF cavities to produce intense and accelerated beams—these series are up to tens of km in length.[58–60] Due to their extreme size and an operational temperature below He's boiling point (4.2 K), the accelerators require extremely costly cryocooling systems, maintenance facilities, and staff.[7,61] Further developments in cavity surface preparation techniques, and even new surface materials, are needed to improve accelerator performance, raise operating temperatures, and lower operational costs.[5,7,24]

Nb has a strong affinity for O. When exposed to air, Nb's surface forms an oxide layer that may be altered by temperature treatments but will return persistently, implying that Nb components in accelerators are covered by an oxide layer.[34,35] Due to the penetration depth of RF

fields, changes in the oxide significantly affect the chemistry of SRF cavity treatments and resulting cavity performance.[21] To gain a thorough and accurate understanding of the interfacial mechanisms driving the performance and development of SRF cavities, we first must investigate the chemistry, structure, and dynamics of oxidized Nb surfaces. The structures of the oxides formed on Nb(100), Nb(110), Nb(111), and polycrystalline Nb have been well characterized, especially at low temperatures.[35,36,38–41,43,54,62–65] Very recently, He atom scattering (HAS) and Auger electron spectroscopy (AES) were used to characterize the evolution of the oxide surface at elevated temperatures, showing that the (3 × 1)-O reconstruction of the Nb(100) surface is stable up to at least 1130 K.[66] However, to our knowledge, oxide surface dynamics have not yet been reported. The (3 × 1)-O Nb(100) surface provides an ideal system to begin investigating the chemistry of Nb oxide surfaces, and this study of the surface's phonon band structure provides information needed to refine current and develop new SRF cavity treatments.

Atomic and molecular beam scattering have been used to investigate the structure and vibrational dynamics of surfaces since the 1920's.[67] Supersonic He beams are suited to study surfaces due to their lack of penetration into the bulk, inertness, and unusually narrow velocity distributions.[3,8,18,68] He atoms' momentum and energy are well matched to those of surface phonons, giving HAS a unique ability to measure and resolve low-energy phonon modes.[3,4,8,18,68,69] These modes, particularly the Rayleigh mode, are sensitive to changes in surface interatomic forces and bonding.[2] In previous studies, the phonon dispersions of bulk Nb and the bare Nb(100) surface were studied with neutron and He atom scattering, respectively, as well as fit to lattice dynamical calculations.[47,70,71] Neutron scattering revealed unusual phonon anomalies for bulk Nb modes along high-symmetry directions.[47,70–73] These phonon dispersion curves were best fit by a model which includes electronic degrees of freedom, indicating that the anomalies are caused by electron-

phonon coupling.[47] Additionally, Kohn anomalies along low-symmetry directions also point to electron-phonon interactions.[72,73] The previous HAS study of Nb(100) surface modes shows no such anomalies, but measurements were confined to the first half of the Brillouin zone (BZ) due to experimental limitations. Furthermore, the discrepancy between the force-constant model used and the experimental data prompted the authors to conclude that a first-principles theoretical approach would be needed to describe the surface accurately.[47]

Unlike for insulators, the interaction between scattered He atoms and the conduction electrons in a metal must play a large role in any successful theoretical model. The He-surface potential is softened relative to that of ionic crystals, while energy exchange with surface phonons is mediated by surface electrons.[2] Density-functional theory (DFT) is a first-principles approach that can create a lattice-dynamical model that includes the role of free electrons in interatomic forces.[2] By reframing the quantum many-body problem into an auxiliary system of independent electrons interacting in an effective potential, while treating the atomic nuclei classically, calculating the dynamical matrix and surface phonon dispersions for the (3×1)-O reconstruction of the Nb(100) surface becomes feasible.[74] In addition, DFT can provide ab initio estimates to quantify the extent of the electron-phonon interaction for a given phonon mode, which correlates directly with the intensity of inelastically scattered He for that phonon.[2]

This combined HAS and DFT study investigates the phonon band structure of the (3×1)-O Nb(100) reconstruction, in addition to the band structures of bulk Nb and the bare Nb(100) surface. The first-principles description of the surface phonon dispersion curves makes clear how the oxide affects phonon polarizations and interatomic forces, and it contributes to a fundamental, chemical understanding of the crystalline and polycrystalline oxidized Nb surfaces. This study provides needed atomic-scale information to the wider SRF community and aids the development

of materials for Nb SRF cavities.

4.2 Experimental

4.2.1 Helium Atom Scattering

We performed measurements with a UHV HAS apparatus that provided high angular and energy resolution. A thorough overview of the instrument is included in Chapter 2, Section 2.4 and reported in detail elsewhere.[49] Elastic diffraction data was taken with a beam modulated by the chopper in a square-wave pattern, with a 50% duty-cycle. Angular distributions were obtained by rotating the detector at 0.2° increments while holding the incident angle and energy fixed, with an overall instrument angular resolution of 0.45°. We collected elastic and inelastic time-of-flight (TOF) spectra by chopping the beam with either a 50% duty-cycle for cross-correlation analysis or with a single-slit, 1% duty-cycle pattern.[17] TOF spectra often were taken multiple times under identical conditions and added to form composite spectra with increased signal-to-noise.

The Nb(100) crystal (Surface Preparation Laboratory, Netherlands, 99.99% purity, ~0.1° cut accuracy) was cleaned according to the procedure in Section 2.4.5 until only Nb and O were present on the surface, as confirmed by AES, and until the surface was smooth enough for high-intensity He diffraction. During data collection, the Nb sample periodically was flashed to about 1200 K to eliminate unwanted surface adsorbates.

4.2.2 Density-Functional Theory

We calculated electron and phonon properties of Nb and NbO with DFT using the open-source plane-wave software JDFTx.[75,76] The electronic states for the outer electrons of Nb ($4p^6 5s^2 4d^3$) and O ($2s^2 2p^4$) were calculated by treating exchange and correlation effects with the

PBE-sol functional and applying the corresponding ultrasoft pseudopotentials parametrized for the functional.[77,78] All DFT calculations presented in this paper employ an electronic cutoff energy of 20 hartree, with a 200 hartree charge density cutoff. Electronic properties for bulk BCC Nb were calculated by sampling 18^3 k-points in the Brillouin zone and solving for 15 bands, with electron occupancies corresponding to a Fermi function at an effective electron temperature of 5 mH. With these parameters, we calculated the lattice constant of Nb to be 3.27 Å, in excellent agreement with the experimental measurement of 3.29 Å.[39] The surface calculations for cubic Nb(100) and (3 × 1)-O Nb(100) sampled 12 × 12 × 1 and 3 × 9 × 1 k-points in the respective Brillouin zones, and electronic occupancies for both systems were calculated using an effective electron temperature of 20 mH. A 10-layer slab was used to calculate the properties of Nb(100) and an asymmetric 8-layer slab was used for (3 × 1)-O Nb(100), with the oxide on one surface and bare Nb(100) on the opposite surface. Using this asymmetric cell, we tested the bare Nb surface of the (3 × 1)-O Nb(100) system against the bare 10-layer Nb(100) slab to ensure that relevant properties converged. To model the experimental oxide surface, whose structure is dominated by a 3 × 1 motif, we introduced surface lattice vectors that are 3 × 1 lattice constants across and allowed the surface vectors of the slab to relax. The surface lattice vectors of the 8 layer (3 × 1)-O Nb(100) slab relaxed between the lattice constants of bulk Nb (3.29 Å) and NbO (2.99 Å); specifically, to values of 3.21 Å and 3.14 Å for the threefold and onefold vectors, respectively.[54] The resulting phonon frequencies of the (3 × 1)-O Nb(100) slab are real-valued, ensuring that our finite system is dynamically stable. To accommodate the minor differences between the DFT and experimental lattice vectors, the reciprocal space plots reported in this paper that compare theory to experiment reference the Brillouin zone in lattice units.

We calculated phonon properties using the finite-difference supercell method, perturbing atoms by ~0.4–0.5 a_0 to calculate the real space interatomic force constant matrix directly.[79] Adequate supercell sizes were 6 × 6 × 6 for bulk BCC niobium, 3 × 3 × 1 for cubic Nb(100), and 1 × 3 × 1 for (3 × 1)-O Nb(100). Properties of the coupled electron-phonon systems required fine k-space samples for accurate calculations of the scattering integrals; we calculated phonon linewidths by transforming into a maximally localized Wannier function (MLWF) basis to sample the Brillouin zone with the Monte Carlo method.[80]

4.3 Theoretical Background

Nb is a conventional superconductor.[57] Its properties can be described reasonably well within the Bardeen-Cooper-Schrieffer (BCS) theory of superconductivity, and its electrons condense into Cooper pairs via the electron-phonon coupling (EPC) mechanism.[81] Theoretical predictions are improved by applying the higher order Eliashberg theory within a DFT framework to calculate EPC explicitly.[79,82,83] By transforming into an MLWF basis, we calculate directly how electrons couple to various lattice distortions to extract the quantities relevant in predicting inelastic He-scattering rates.[84] Specifically, we employ perturbation theory and calculate the overlap of the perturbing electron-ion potential between the unperturbed electronic states in order to calculate explicitly the electron-phonon matrix elements within DFT:[85]

$$g^{\boldsymbol{q}\nu}_{n\boldsymbol{k},\, n'\boldsymbol{k}+\boldsymbol{q}} = \left(\frac{\hbar}{2M\omega_{\boldsymbol{q}\nu}}\right)^{\frac{1}{2}} \langle \psi_{n',\boldsymbol{k}+\boldsymbol{q}} \left| \frac{dV^{e-i}}{du_{\boldsymbol{q}\nu}} \cdot \hat{\epsilon}_{\boldsymbol{q}\nu} \right| \psi_{\boldsymbol{q}\nu} \rangle, \tag{4.1}$$

where $u_{\boldsymbol{q}\nu}$ and $\omega_{\boldsymbol{q}\nu}$ are the atomic displacements and frequencies, respectively, for the phonon mode ν with crystal momentum $\boldsymbol{q}$ and polarization vector $\hat{\epsilon}_{\boldsymbol{q}\nu}$, and M is the ion mass.

The above matrix elements connect to inelastic He-scattering rates through the phonon linewidths and the dimensionless EPC constants. Specifically, the phonon linewidths, or equivalently, the inverse phonon lifetimes, are defined as:[86]

$$\gamma_{\boldsymbol{q}\nu} = 2\pi\omega_{\boldsymbol{q}\nu}\sum_{n,n'}\int\frac{d^3k}{(2\pi)^3}\left|g^{\boldsymbol{q}\nu}_{n\boldsymbol{k},n'\boldsymbol{k}+\boldsymbol{q}}\right|^2\delta\left(e_{\boldsymbol{q},n}-e_F\right)\delta\left(e_{\boldsymbol{k}+\boldsymbol{q},n'}-e_F\right). \tag{4.2}$$

These linewidths then determine the dimensionless EPC constants,

$$\lambda_{\boldsymbol{q}\nu} = \frac{\gamma_{\boldsymbol{q}\nu}}{\pi\hbar N(e_F)\omega^2_{\boldsymbol{q}\nu}}, \tag{4.3}$$

where $N(e_F)$ denotes the electronic density of states at the Fermi level.

Finally, to estimate HAS signal intensities, we follow the theoretical frame of Benedek et al. and estimate the inelastic scattering probability to be proportional to $\lambda_{\boldsymbol{q}\nu}$, but instead of using an approximate analytic form for the surface electron-phonon matrix elements, we calculate the matrix elements ab initio directly in an MLWF basis using DFT.[87–91] In order to better probe the surface-specific phonon characteristics measured by HAS, we project the mode-selected EPC constants onto the z-displacements of the corresponding phonon polarization vector, while including the exponential decay of the He wave functions into the material, and define the surface-projected EPC constants as:

$$\bar{\lambda}_{\boldsymbol{Q}\nu} \propto \sum_{\boldsymbol{Q}\nu,\kappa}|e^{\alpha=z}(\boldsymbol{Q}\nu)|^2\,\lambda_{\boldsymbol{Q}\nu}exp(-\beta z_\kappa)\delta\left(E-\hbar\omega_{\boldsymbol{Q}\nu}\right). \tag{4.4}$$

Here, κ labels the atoms, z represents the atoms' distance beneath the surface, β is the He decay softness parameter, and E is the energy transfer of the He atom. The above expression is written as a proportionality because here we do not include factors, such as additional matrix elements, that are considered to be energy- and wavevector-independent.[87–90] Following standard distorted-wave Born approximations of atom-surface potentials, we estimate the softness parameter, β, for Nb(100) to be ~2.1 Å^{-1}, which falls within the typical range expected for metals.[2,92]

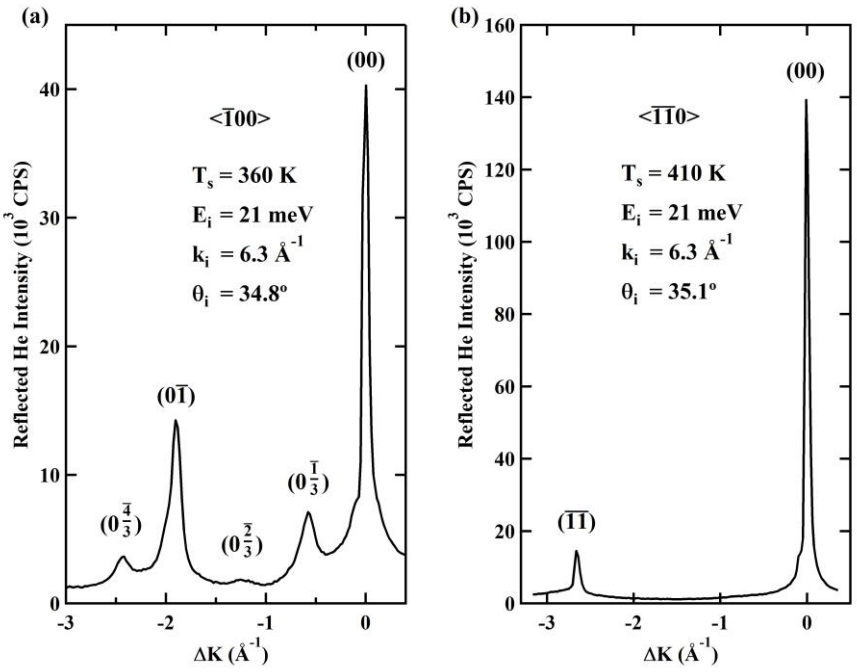

Figure 4.1: Representative He atom diffraction spectra for the (3 × 1)-O Nb(100) surface along the (a) <$\bar{1}$00> and (b) <$\bar{1}\bar{1}$0> symmetry axes. The specular (00) peak is visible in both directions, while the oxide structure can be seen in (a) along the <$\bar{1}$00> axis, with fractional peak notation corresponding to the (3 × 1)-O structure. The <$\bar{1}\bar{1}$0> axis in (b) shows the underlying ($\bar{1}\bar{1}$) Nb(100) lattice peak.

4.4 Results and Discussion

He diffraction scans from the (3 × 1)-O Nb(100) surface are shown in Figure 4.1. Figure 4.1(a) is a representative angular scan along the <$\bar{1}$00>, $\overline{\Gamma X}$ azimuthal direction, while Figure 4.1(b) is a scan along the <$\bar{1}\bar{1}$0>, $\overline{\Gamma M}$ direction. We took both scans with a cold He beam (E_i = 21 meV) and slightly elevated surface temperatures (T_S = 360 K and 410 K for Figures 4.1(a) and 4.1(b), respectively). The scan in Figure 4.1(a) was taken at an incident angle of $\theta_i = 34.8°$; we confirmed surface reproducibility by taking repeated diffraction scans at $T_S = 360$ K after flashing the crystal to 1200 K. The specular peak ($\theta_i = \theta_f$) at $\Delta K = 0$ is approximately 2.6 times more intense than the next largest, first-order ($0\bar{1}$) diffraction peak at ΔK = -1.9 Å^{-1} ($\theta_f = 15.8°$). When

compared with a scan of bare Nb(100), the larger first- to zeroth-order peak intensity ratio indicates that the oxide structure has a higher surface corrugation.[4] Each peak occurs when the Bragg equation holds true; that is, when

$$\Delta K = k_i\left(\sin\theta_i - \sin\theta_f\right) = G_{mn}, \tag{4.5}$$

where the surface-parallel component of the He wavevector k_i changes by ΔK; the initial and final scattering angles, relative to surface normal, are θ_i and θ_f, respectively; and G_{mn} is a linear combination of reciprocal surface lattice vectors.

Three additional diffraction peaks are visible in the angular scan of the <$\bar{1}$00>, $\overline{\Gamma X}$ azimuthal direction, all of which correspond to the (3 × 1)-O ladder structure. The $\left(0\,\frac{\bar{1}}{3}\right)$ peak, at ΔK = -0.6 Å^{-1} (θ_f = 28.7°), is approximately one-third of the way between the (00) and (0$\bar{1}$) peaks. Similarly, the $\left(0\,\frac{\bar{2}}{3}\right)$ peak (ΔK = -1.2 Å^{-1}, θ_f = 22.0°) is two-thirds of the way between the primary peaks, while the $\left(0\,\frac{\bar{4}}{3}\right)$ peak (ΔK = -2.4 Å^{-1}, θ_f = 10.8°) is past the (0$\bar{1}$) peak by one-third of that distance. The visibility of all three superlattice peaks shows the excellent surface order of the sample and the minimal scattered He background intensity measured by the detector.

The angular scan in Figure 4.1(b) was taken at an incident angle of θ_i = 35.1° in the <$\overline{11}$0>, $\overline{\Gamma M}$ direction. Since the (3 × 1)-O reconstruction does not affect atomic spacing along this azimuthal direction, only primary lattice diffraction peaks are seen. The specular peak at ΔK = 0 is much larger than the first-order, ($\overline{11}$) diffraction peak (ΔK = -2.7 Å^{-1}, θ_f = 8.9°), indicating that the surface is corrugated slightly less along this axis than along the $\overline{\Gamma X}$ axis.[4]

For inelastic, in-plane scattering, the conservation of energy and crystal momentum dictates possible scattering angles and energies. For a given beam with incident energy E_i,

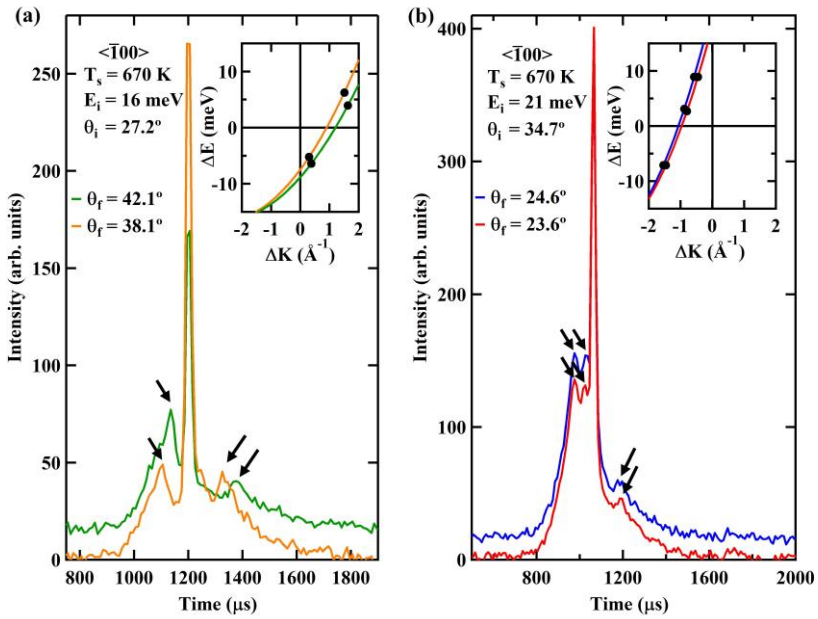

Figure 4.2: Representative cross-correlation TOF spectra for the (3 × 1)-O Nb(100) surface along the <$\bar{1}$00> symmetry axis, under different incident and final conditions. Data in (a) were taken with a 16 meV incident He beam, while data in (b) were taken with a 21 meV incident beam. Phonon peaks are designated by black arrows, with insets showing representative scan curves for each spectrum. Black dots indicate phonon peak positions; ΔE is the energy gained or lost by the He beam.

wavevector k_i, and angle θ_i, possible final conditions (angle θ_f, wavevector k_f, and energy E_f) must satisfy the equation,

$$\Delta K = k_f \sin\theta_f - k_i \sin\theta_i = G_{mn} + Q, \tag{4.6}$$

where G_{mn} again is a linear combination of reciprocal surface lattice vectors and Q is the two-dimensional wavevector for a phonon with energy $\hbar\omega$. By substituting relevant energies (Equation 4.7) and rearranging, the scan curve indicating accessible phonons can be extracted (Equation 4.8):

$$\Delta E = E_f - E_i = \frac{\hbar^2 k_f^2}{2m} - \frac{\hbar^2 k_i^2}{2m} = \hbar\omega(Q); \tag{4.7}$$

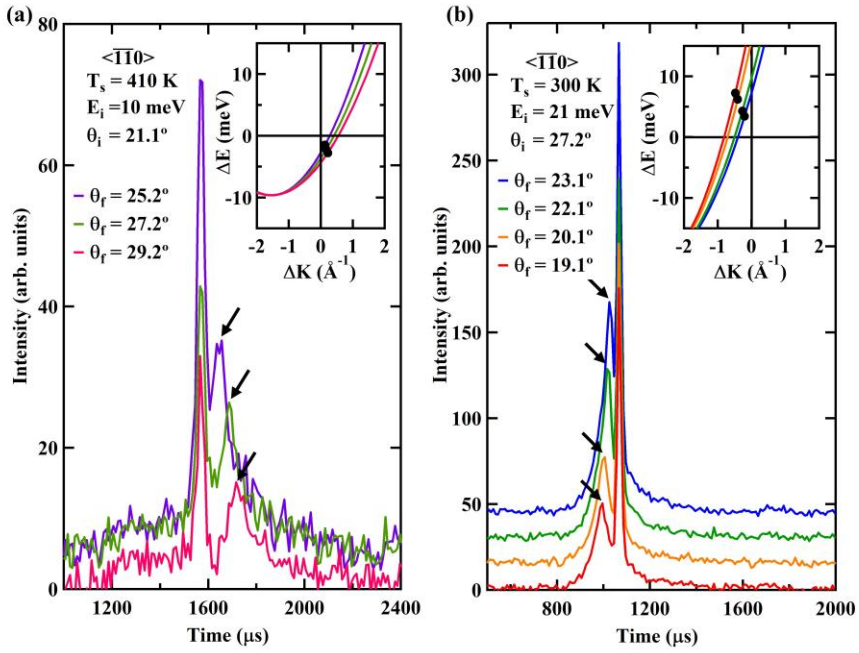

Figure 4.3: Representative cross-correlation TOF spectra for the (3 × 1)-O Nb(100) surface along the <$\overline{1}$10> symmetry axis. Data in (a) were taken with a 10 meV incident He beam, while data in (b) were taken with a 21 meV incident beam. Phonon peaks are designated by black arrows; insets show representative scan curves for each spectrum with black dots indicating phonon peak positions. ΔE is the energy gained or lost by the He beam.

$$\frac{\Delta E}{E_i} = \frac{\left(\sin\theta_i - \frac{\Delta K}{k_i}\right)^2}{\sin^2\theta_f} - 1. \tag{4.8}$$

Systematically varying incident beam energy and angle while capturing TOF spectra moves the scan curve across the surface Brillouin zone (SBZ) and maps out surface phonon resonances.

Figure 4.2 shows examples of cross-correlation TOF spectra measured along the <$\overline{1}$00>, $\overline{\Gamma X}$ axis. Each spectrum was taken under specific incident and final conditions that maximized intensity and resolution. We explored various surface temperatures, with $T_S = 670$ K yielding the best results: for this axis, all spectra were taken with cross-correlation chopping at $T_S = 670$ K. Figure 4.2(a) and Figure 4.2(b) were taken with incident energies $E_i = 16$ meV and 21 meV and angles $\theta_i = 27.2°$ and 34.7°, respectively. The dominant peak in each spectrum is elastic, where

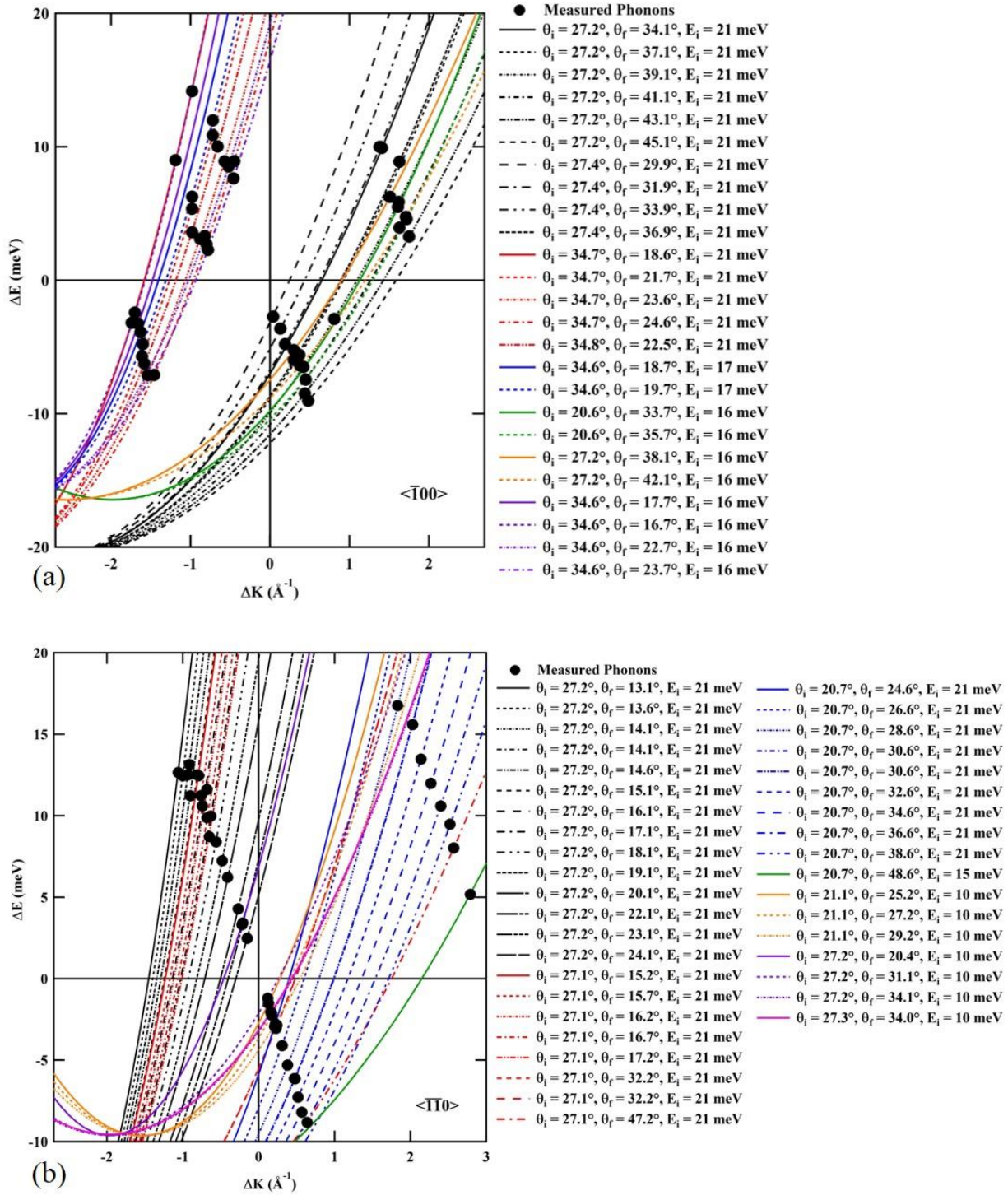

Figure 4.4: Extended dispersion plots along the (a) <$\bar{1}$00> and (b) <$\overline{11}$0> symmetry axes, with corresponding scan curves and He scattering conditions. Each black dot represents the center of a phonon peak from a TOF spectrum, while scan curves are shown as solid or dashed lines. These values are as measured by the He beam, where ΔE indicates energy gained or lost by the He beam.

$E_i = E_f$, and was used to calculate incident beam energy. Subsidiary peaks—indicated by black arrows—are phonon modes, with peaks to the left of elastic corresponding to surface phonon annihilation (the He beam gains energy), and peaks to the right corresponding to surface phonon creation (the He beam loses energy). We identified the position of the top of each peak by fitting a given spectrum with multiple Gaussian functions and extracting the function centers. That time then was correlated with a specific ΔE and ΔK for the He beam and plotted, along with the corresponding scan curve, in Figure 4.2's insets.

Figure 4.3 shows similar TOF spectra but taken along the <$\overline{1}\overline{1}0$>, $\overline{\Gamma M}$ axis. Along this axis, we held the surface temperature at either T_S = 300 K or 410 K, depending on the scan. Additionally, a few phonon modes identified in this direction were measured using a single-shot chopping pattern for increased resolution, though Figure 4.3 contains cross-correlation data. Figure 4.3(a) was taken with $T_S = 410$ K, $E_i = 10$ meV, and $\theta_i = 21.1°$, while $T_S = 300$ K, $E_i = 21$ meV, and $\theta_i = 27.2°$ for Figure 4.3(b). Phonons are identified with black arrows and we obtained peak positions in the same manner as for Figure 4.2. Phonon positions in the SBZ with corresponding scan curves are shown in the figure insets.

All measured phonon peak positions are shown as black dots in Figure 4.4, with Figure 4.4(a) showing data taken along the $\overline{\Gamma X}$ axis and Figure 4.4(b) along the $\overline{\Gamma M}$ axis. As in Figures 4.2 and 4.3, these extended SBZs are as measured by the He beam, with ΔE indicating energy gained or lost by the beam. The scan curve for each TOF spectrum is shown as a solid or dashed line and is labeled according to the incident and final scattering conditions. Multiple phonon resonances are seen in both axes and will be discussed below with DFT results.

Figure 4.5(a) shows the DFT-calculated phonon modes of bulk Nb along the BCC Brillouin zone symmetry directions. These reproduce previously calculated and measured results,

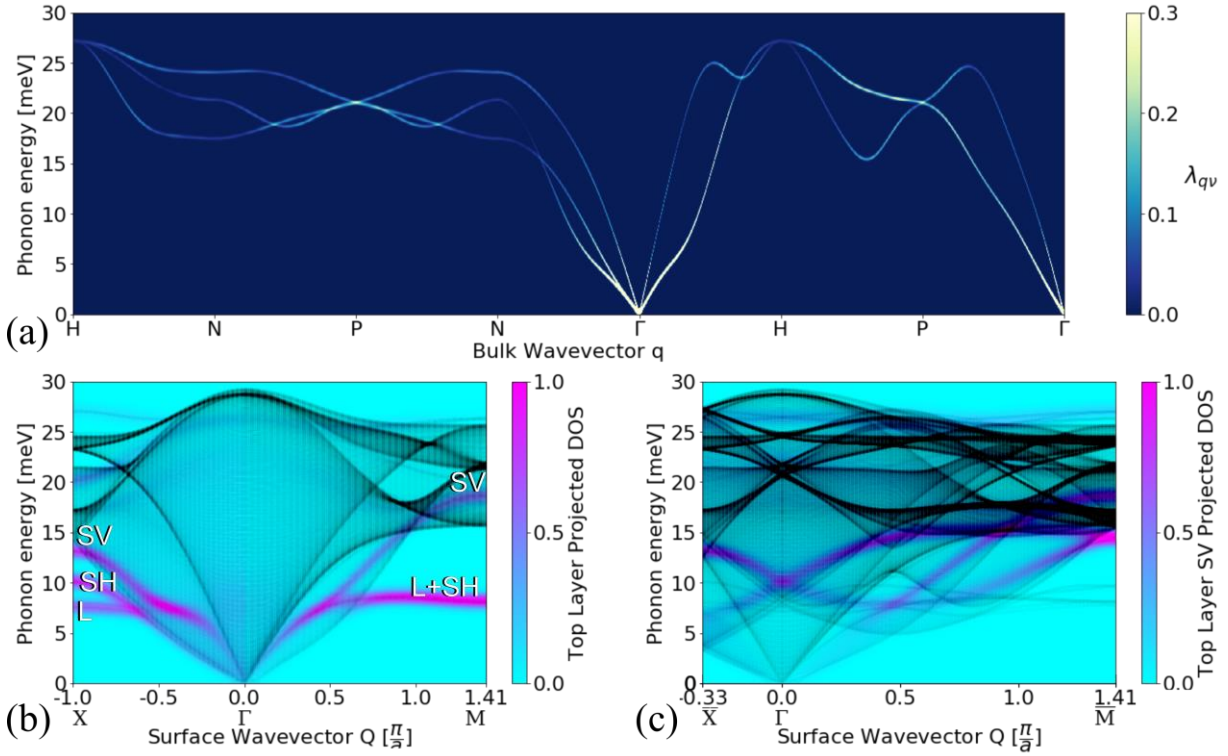

Figure 4.5: (a) Bulk phonon dispersions calculated for Nb along high-symmetry paths of the BCC Brillouin zone, where each mode's EPC strength is indicated by its brightness level and brighter colors correspond to stronger coupling. Surface phonons along symmetry directions $\overline{\Gamma}\overline{X}$ and $\overline{\Gamma}\overline{M}$ for (b) cubic Nb(100) and for (c) (3 × 1)-folded Nb(100). Black lines represent phonon dispersions calculated for an effective 130-layer slab of Nb(100). The colormaps display the surface phonon density of states projected onto the top layer of atoms, and surface resonances are labeled for the shear-vertical (SV), shear-horizontal (SH), or longitudinal (L) in (b). The (3 × 1)-folded Nb(100) colormap in (c) displays only the SV mode to demonstrate the BZ folding process more clearly.

confirming the accuracy of the method used.[47] Phonon anomalies seen by the change in slope of the bottom-most resonances along the ΓH and ΓN directions are observed, as are dips in the higher resonance along ΓH and lower resonance along HP, and a resonance crossing near H along ΓH.[47,71] The bulk phonon modes are colored by their respective EPC constant strengths, λ_{qv}: by taking advantage of the MLWF basis, we are able to track the EPC of bulk Nb throughout the Brillouin

zone. The strongest coupling is seen near the Γ point for all resonances, which corresponds with lower phonon energies.

Next, we identified both surface-projected bulk phonon modes and surface modes for an effective 130-layer slab of Nb(100) by beginning with a 10-layer slab and inserting 120 bulk layers into its dynamical matrix. These results are shown in Figure 4.5(b) along symmetry directions $\bar{\Gamma}\bar{X}$ and $\bar{\Gamma}\bar{M}$ and are overlaid with a colormap of the top-layer surface phonon density of states (DOS). By examining the atomic displacements associated with the surface phonon modes, we identify polarizations and find that the longitudinal (L) and shear-horizontal (SH) modes dip below the shear-vertical (SV) mode and the bulk-projected band along both symmetry directions. The highest surface DOS is seen in the L+SH mode near $\bar{M}$. In Figure 4.5(c), we folded the effective 130-layer slab of cubic Nb(100) to represent a (3 × 1)-folded BZ equivalent to the BZ of (3 × 1)-O Nb(100). The folded BZ displays more apparent resonances at a given wavevector, both surface-projected bulk and strictly surface, as a result of the folding. For example, what once were acoustic modes can now, after folding, appear as optical modes. This process is illustrated in Figure 5(c): considering only the top-layer SV projected DOS for clarity, the DOS now disperses to higher phonon energies at shorter wavevectors. Accordingly, surface modes are folded to near the middle of the surface-projected bulk band, and the SV mode in particular is translated to about 10 meV at the $\bar{\Gamma}$-point.

Figure 4.6 shows the results from our calculated EPC strengths for bulk Nb projected on the SBZ, along with the coupling strengths for the bare Nb(100) and (3 × 1)-O Nb(100) surfaces. Values of surface EPC strengths are projected onto exponentially weighted z-displacements (see Equation 4.4), as these are what can be seen most readily with HAS. The first BZ for both the bare and (3 × 1)-O surfaces are folded to correspond with the ladder structure and allow for direct

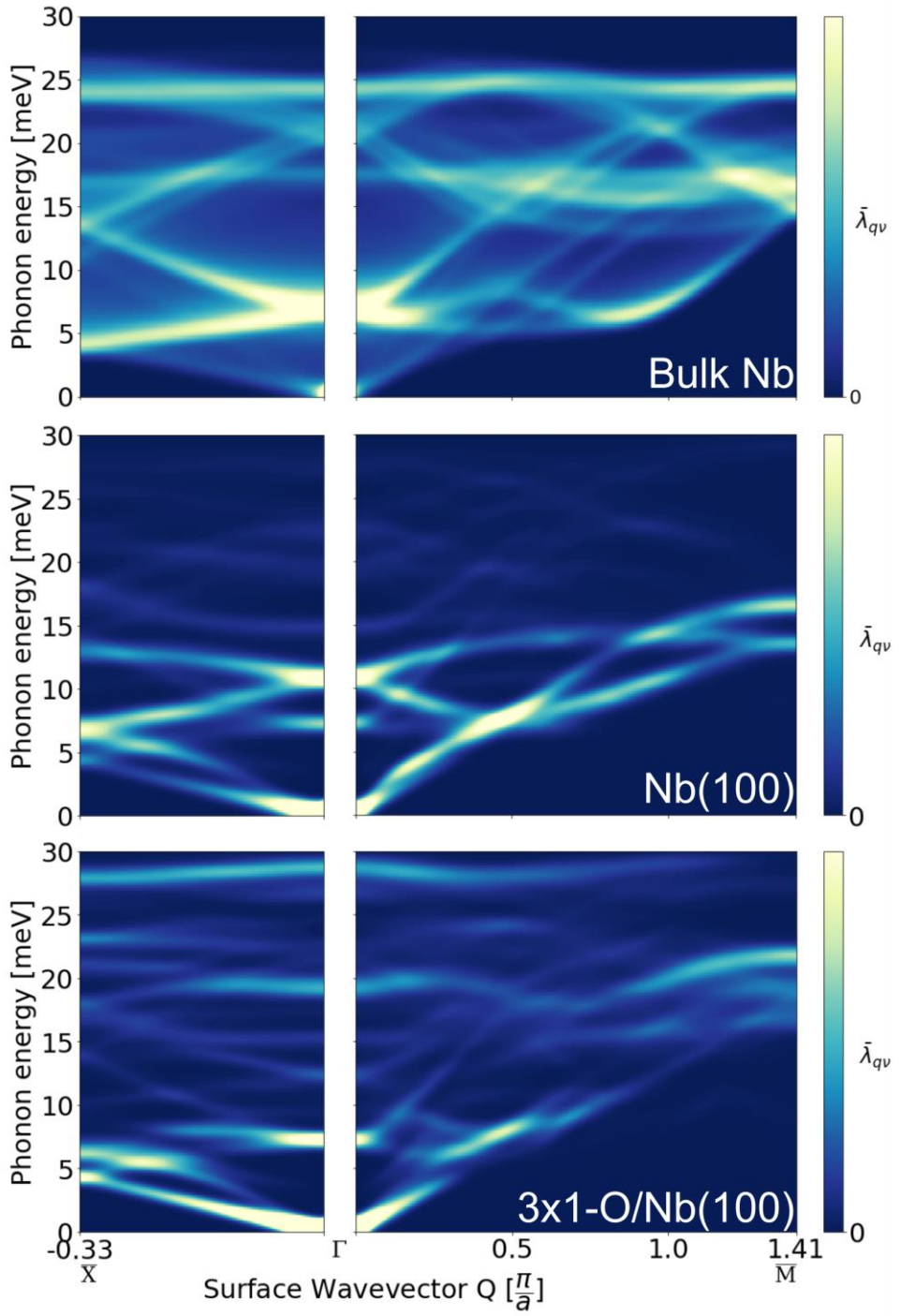

Figure 4.6: Surface EPC strengths along SBZ symmetry directions $\bar{\Gamma}\bar{X}$ (left column) and $\bar{\Gamma}\bar{M}$ (right column), projected from bulk Nb (top row) onto the SBZ and projected onto the exponentially weighted z-displacements using Equation 4.4 for (middle row) the bare Nb(100) surface and (bottom row) the (3 × 1)-O Nb(100) surface. Coupling strengths are indicated by brightness level, with brighter colors corresponding to stronger coupling.

comparison. The EPC for the Nb(100) surface is pronounced near the $\bar{\Gamma}$-point at low energies and near 11 meV, higher than it is for bulk Nb projected on the SBZ. Multiple resonances are seen along both directions for Nb(100), though most of the EPC strength is concentrated below 16 meV.

The electron-phonon interaction strength becomes much more dispersed for the oxide surface, with multiple new resonances appearing at higher phonon energies due to the addition of the less massive O atoms. The resonances at $\bar{\Gamma}$, approximately 11 meV for Nb(100), move higher, to about 13 meV, and lose significant relative strength for the oxide. The resonance at 7 meV appears more intense for the oxide, as are the lowest resonances along both symmetry directions. High-energy, optical modes also appear in the oxide, most notably near 28 meV. However, the strongest couplings for the bare Nb(100) and oxide surfaces are seen in approximately the same locations: in the acoustic modes near the $\bar{\Gamma}$ point for 0–3 meV; near the $\bar{X}$ point near 5 meV; and near 0.5 π/a along the $\bar{\Gamma}\bar{M}$ around 7 meV.

When a He atom scatters from a metal, it scatters from the surface electron density. The creation or annihilation of surface phonons occurs through these electrons, intrinsically linking HAS with EPC strengths.[2] In Figure 4.7, HAS phonon data are overlaid with the calculated dispersion plot for (3 × 1)-O Nb(100), where experimental data points are shown as white dots and EPC strength is indicated by brightness. Excellent agreement is seen between the experimental and theoretical results and demonstrates the importance of electron-phonon interactions in resonances visible with inelastic He scattering. The density of measured points is a convolution of experimental conditions and available phonon modes—where phonons were more easily resolved, more phonons were measured. The highest density of measured points, near $\bar{X}$ and 6 meV and near 0.25 π/a along $\bar{\Gamma}\bar{M}$ and 3 meV, corresponds with stronger EPC calculated by DFT. Along the $\bar{\Gamma}\bar{X}$ direction two modes can be seen with HAS, though their distinction is blurred at higher energies

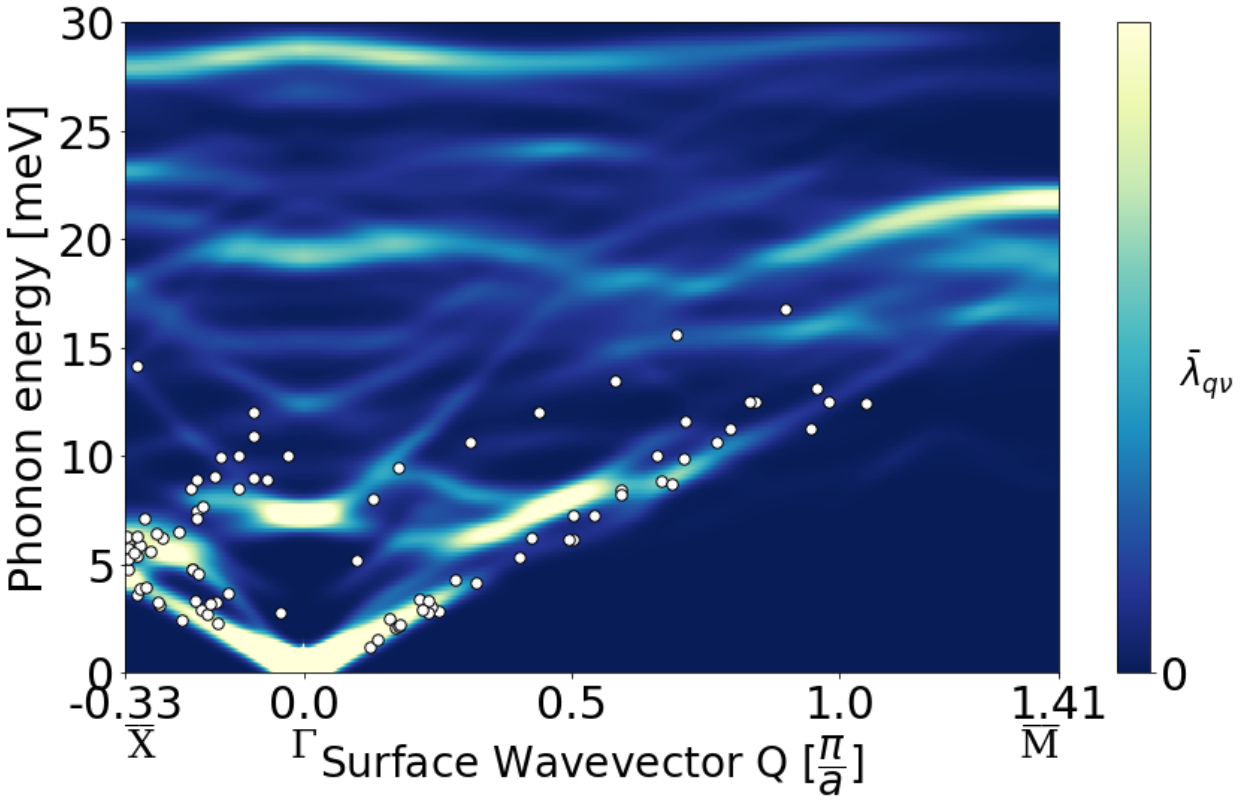

Figure 4.7: Phonons for the (3 × 1)-O Nb(100) surface measured with HAS (white dots), overlaid on DFT-calculated surface EPC strengths projected onto *z*-displacements, using Equation 4.4. Coupling strengths are indicated by brightness level, with brighter colors corresponding to stronger coupling. HAS data and theoretical predictions along $\bar{\Gamma}\bar{M}$ were translated back into the first BZ of cubic Nb(100), while the data along $\bar{\Gamma}\bar{X}$ was folded back to the (3 × 1)-folded BZ of the ladder structure.

by the folding of the first BZ. The lowest mode is the Raleigh mode while the upper is longitudinal, but as will be seen in Figure 4.8, towards the zone boundary there is a hybridization and mixing of SV and L displacements which blurs this distinction, a common feature of metal surfaces.[93]

There also are two modes measured with HAS along the $\bar{\Gamma}\bar{M}$ direction, with the lower mode again being the Rayleigh mode. By comparing the EPC strengths for Nb(100) and (3 × 1)-O Nb(100) in Figure 4.6, we attribute the upper measured mode primarily to the addition of the oxide on the surface. This corresponds with the trend seen in Figure 4.6, where the oxide disperses EPC,

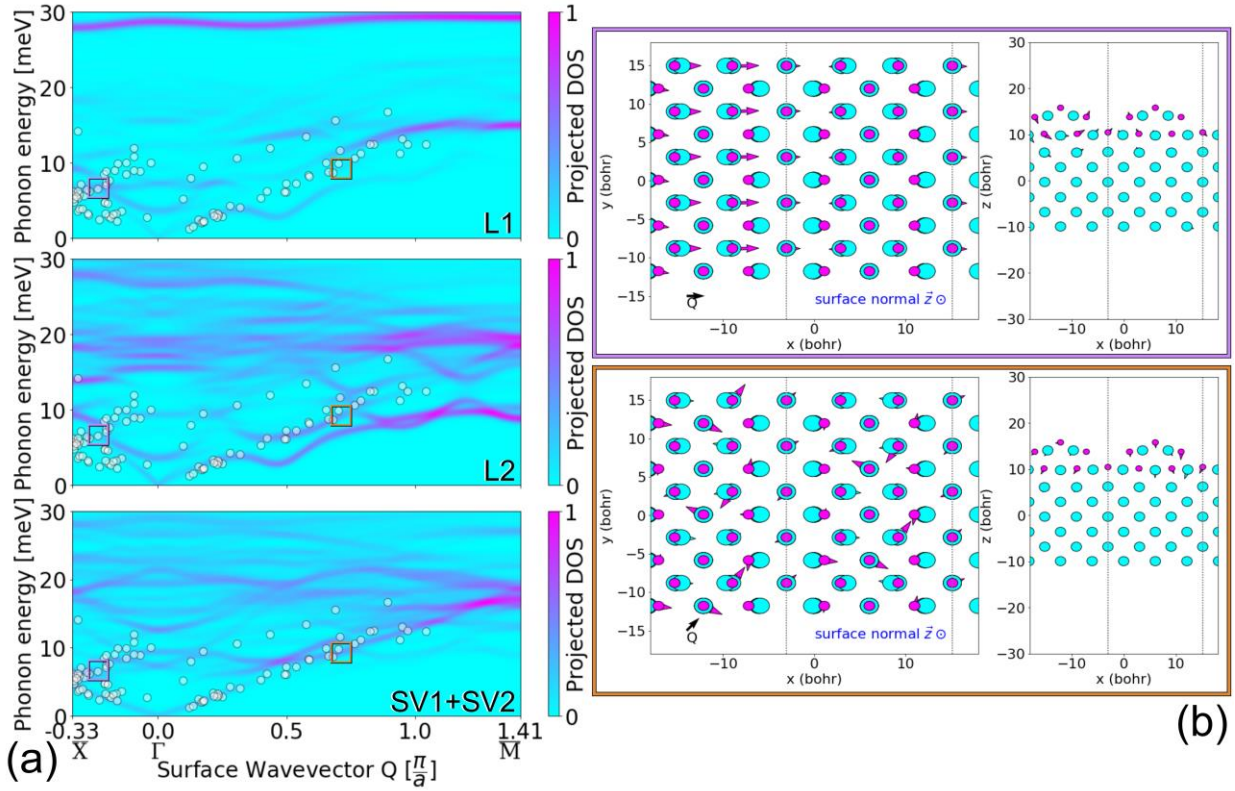

Figure 4.8: Top layer densities of states projected onto the SV or L displacements of the surface atoms of (3 × 1)-O Nb(100); from top to bottom: L displacements from layer one (L1) and from layer two (L2), and SV displacements from layers one and two (SV1+SV2), where layer one refers to the crest of the oxide and layer two denotes the planarly intact layer beneath the crest. Each white circle marks an HAS event (repeated from Figure 4.7). (b) Atomic displacements of the Nb atoms (larger teal circles) and O atoms (smaller magenta circles) for (3 × 1)-O Nb(100) calculated with DFT corresponding to the two boxed modes highlighted in (a). The displacements in the (upper) violet box correspond to the mode along $\bar{\Gamma}\bar{X}$ at 6.8 meV and the displacements in the (lower) orange box correspond to the mode along $\bar{\Gamma}\bar{M}$ at 9.3 meV. The arrows in (b) indicate directions of the atomic displacements and their relative magnitudes, viewing (left) down along surface normal and viewing (right) along the surface with the surface normal pointing up. The vertical dashed lines in (b) coincide with the troughs in the ladder structure.

and hence inelastic He-scattering intensity, to higher energies. An anomalous feature can be seen in the lowest longitudinal mode along $\bar{\Gamma}\bar{M}$, indicating a lattice instability which often is

accompanied by a symmetry breaking, and may be related to the oxide reconstruction but requires further analysis.[94]

Figure 4.8(a) shows the top layer DOS projected onto the SV or L displacements of (3 × 1)-O Nb(100) surface atoms. This allows us to assign the polarizations to the modes measured by HAS. Along $\bar{\Gamma}\bar{X}$, the lowest measured mode, or the Raleigh mode, is almost entirely SV, while the higher modes are mixed L and SV. Along $\bar{\Gamma}\bar{M}$, both measured modes appear mixed, though the higher mode is primarily L due to second-layer atoms (L2), while the lower mode mixes L1, L2, and SV1+SV2. The high-energy optical mode across the entire SBZ is seen to be almost entirely L due to the top layer of atoms—from the crests of the (3 × 1)-O Nb(100) ladder structure. This mode has the highest DOS for L1, has very little dispersion, and is near the top of the bulk-projected band seen in Figure 4.5(c).

Two specific phonons measured by HAS are examined in Figure 4.8(b): one along $\bar{\Gamma}\bar{X}$ (upper violet box) and one along $\bar{\Gamma}\bar{M}$ (lower orange box). Figure 4.8(b) shows the atomic displacement directions and magnitudes with arrows corresponding to O (smaller magenta circles) or Nb (larger teal circles) atoms, viewed along surface normal and viewed head-on with surface normal pointing up. For both phonons, the O atoms are much more active than the Nb. The phonon in the violet box is primarily L in the first layer of atoms, as indicated both by Figure 4.8(a) and by the direction of the arrows in Figure 4.8(b). The resonance in the orange box is a hybridization of L and SV, involving L displacements in the second layer of atoms and SV in both the first and second layers.

Figure 4.9 shows the pairwise interatomic force constants for bulk Nb, Nb(100), and (3 × 1)-O Nb(100). The addition of the oxide to the surface causes a significant increase in force constants, even between Nb atoms. The highest force recorded was the force a Nb atom feels on

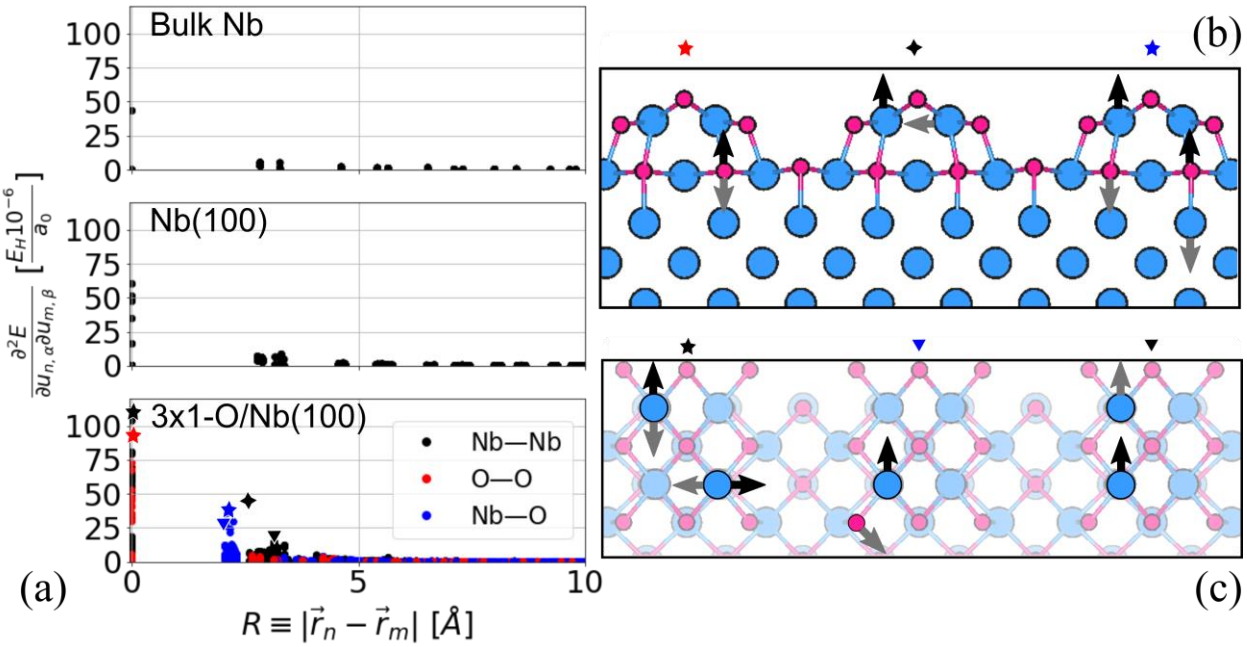

Figure 4.9: (a) Pairwise interatomic force constants in bulk Nb, Nb(100), and (3 × 1)-O Nb(100) all plotted on the same scale as a function of distance between the two atoms, with $R = 0$ corresponding to the force an atom feels on itself when perturbed. All interatomic force constants in bulk Nb and Nb(100) involve only Nb-Nb interactions (black circles), while (3 × 1)-O Nb(100) includes additional force constants between Nb-O (blue circles) and O-O (red circles). Noteworthy interatomic force constants in (3 × 1)-O Nb(100) are marked with distinct symbol shapes in (a) and then depicted in the crystal structures in either (b) a side view with surface normal pointing up or in (c) a top down view with surface normal pointing out of the page. In (b) and (c), Nb atoms are colored as larger blue circles and O as smaller magenta circles, and the black and gray arrows correspond to the atomic perturbation and responding forces, respectively.

itself when perturbed along the surface, which is labeled by a black, five-pointed star and illustrated in Figure 4.9(c). This force is almost twice the highest force seen for the bare Nb(100) surface, indicating that the oxide stabilizes the surface. Another notable feature is the Nb-Nb force increase caused by the oxide, which is labeled by the black, four-pointed star at approximately $R = 2.6$ Å. This is the surface-parallel force on one of the Nb atoms in the crest of the (3 × 1)-O Nb(100) ladder structure when another atom in the crest is disturbed along the surface-normal direction, as seen in Figure 4.9(b). A surface-parallel perturbation of a Nb atom within the crest

causes a relatively high response in a neighboring Nb atom 3.1 Å away, also in the surface-parallel direction (black triangle in Figure 4.9(c)). Most of the force constants that involve O atoms, shown by the red and black markers in Figure 4.9(a), are higher than the Nb-Nb force constants in bulk Nb and the bare Nb(100) surface. This feature occurs most prominently when Nb and O are near neighbors, separated by about $R = 2.1$ Å (the blue five-pointed star in Figure 4.9(b) and the blue triangle in Figure 4.9(c)).

Our work shows that the (3 × 1)-O superlattice structure significantly modifies the forces of bulk Nb and the unreconstructed, bare Nb(100) surface. The strong bonds introduced by the (3 × 1)-O superlattice make up the characteristic ladder crests and strongly oppose surface-normal and surface-parallel perturbations. This result explains the high-energy phonon resonances in the dispersion plot shown in Figure 4.7 and stabilizes the Nb surface, leading to Nb's strong affinity for O.[34,35] Additionally, the strengthened Nb-Nb bonds indicate a heightened Nb diffusion barrier at the surface.[95] The (3 × 1)-O structure could inhibit nucleation and alloying at the surface, raising surface melting temperatures and the alloying temperatures of relevant SRF materials such as Sn.[96–98]

Recent work by Farber et al. characterizes Sn adsorption and diffusion behavior on the (3 × 1)-O Nb(100) surface reconstruction.[99] Their results reveal that defects do not alter significantly either Sn adsorption or diffusion: these processes likely are dictated by the (3 × 1)-O superlattice structure. Our results support this interpretation of their data by indicating that the ladder crest features are strongly bonded and thus resistant to perturbation. Our results also explain their observed adsorption sites and preferential diffusion along the troughs of the ladder structure. An atomic-scale, theoretical characterization of the (3 × 1)-O Nb(100) surface alloying with Sn has not been completed. However, our results suggest that the ladder troughs are susceptible sites

for reactivity or alteration, while the ladder crests are strongly stabilizing and provide a barrier to treatments and corresponding reactions. Further atomic-scale studies of alloying on these surfaces will provide a more detailed picture.

4.5 Conclusion

We used HAS and DFT to map the surface phonon dispersions of the (3 × 1)-O Nb(100) reconstruction. A comparison between calculated resonances of the bare Nb(100) surface and the oxide surface show a large increase in phonon modes for the oxide, especially at higher energies. We explicitly calculated the electron-phonon interaction strengths at the surface and compared the results with inelastic He TOF data. The excellent agreement seen between experiment and theory allows us to identify the measured surface modes. The primary modes measured with HAS are caused largely by longitudinal and shear-vertical displacements of the top two layers of O and Nb atoms on the (3 × 1)-O surface, and these modes also display meaningful electron-phonon interaction strengths. DFT analysis of the force constants at the surface show significant increases in bonding forces between Nb atoms, as well as strong Nb-O and O-O bonds. These data further expound what is known about the oxide surface and will inform the development of new SRF cavity treatments by elucidating the dynamics of the oxide surface. While this collaborative work begins to reveal how the (3 × 1)-O superlattice structure alters EPC at the Nb(100) surface, it is only a piece of the picture. Beyond the differences in phonon resonances shown above, the significant modification of interatomic interactions could in turn affect surface superconductivity and SRF cavity behavior. Future experimental and theoretical studies investigating the EPC of these surfaces are currently underway.

Chapter 5

Conclusions and Future Directions

In this thesis, a combination of helium atom scattering (HAS) and complementary density-functional theory (DFT) was used to characterize the (3 × 1)-O Nb(100) surface reconstruction. **Chapter 3** makes use of elastic helium scattering to monitor surface stability as a function of surface temperature, while inelastic helium scattering and DFT are used in **Chapter 4** to explore the surface's phonon band structure and force constants. Both chapters contribute needed information about the oxide surface that can be used to improve existing tin deposition procedures for superconducting radiofrequency (SRF) cavities, while also paving the way for the development of other niobium-alloy materials. To further delve into the intricacies of the (3 × 1)-O Nb(100) surface, future HAS studies could include measuring the electron-phonon coupling (EPC) of the surface, as well as using quasielastic helium scattering to track diffusion across the surface. Monitoring the surface's EPC constant while introducing nitrogen, hydrogen, or additional oxygen would relate surface order and composition to SRF cavity performance, while surface diffusion of these gases would provide more information for SRF material fabrication.

5.1 Conclusions

Using a newly developed crystal mount, electron-beam heater, and detector-computer interface system, we cleaned and analyzed a Nb(100) crystal. The characteristic (3 × 1)-O ladder structure formed on the surface with an average domain size of 210 $\pm$ 10 Å, as determined by the width of measured specular peaks. We observe both primitive and superlattice diffraction peaks along the $<\bar{1}00>$, $\overline{\Gamma X}$ azimuthal direction, while only primitive peaks are seen along $<\bar{1}\bar{1}0>$, $\overline{\Gamma M}$.

By taking repeated diffraction scans, we tracked the stability of the surface through a wide temperature range. The superlattice peaks remain visible up to at least 1130 K, above which they are swallowed by increasing background signal. This does not necessarily mean that the superlattice disorders above this temperature. Instead, it implies that other methods are needed to determine stability above 1130 K. Specular peak analysis along the <$\overline{1}\overline{1}0$>, $\overline{\Gamma M}$ direction shows little to no change in peak width through 1210 K, which is confirmed by Auger electron spectroscopy. Given these results, we can conclude confidently that the (3 × 1)-O Nb(100) surface is stable up to at least 1130 K, and presumably through at least 1210 K.

We then turned our attention to surface dynamics. Using He time-of-flight (TOF) measurements, we determined the energies and wavevectors of single phonons across the surface Brillouin zone, along both the $\overline{\Gamma X}$ and $\overline{\Gamma M}$ directions. Complementary DFT calculations confirmed peak locations and provided addition details pertaining to the phonon resonances. HAS revealed two resonances along each direction. Along $\overline{\Gamma X}$, the upper mode measured is hybridized longitudinal (L) and shear-vertical (SV), while the lower mode is almost entirely SV. Along $\overline{\Gamma M}$, both the upper and lower modes measured are mixed L and SV. The higher mode primarily involves the atoms in the second layer from the surface, while the lower includes the first- and second-layer atoms. In addition to assigning polarizations to measured resonances, DFT calculations also show that the less-massive oxygen atoms move more than the niobium atoms and create high-energy optical phonon modes. Pairwise interatomic force constants calculated with DFT reiterate the effect of the oxygen on the niobium surface: oxygen strengthens the bonds at the surface, passivating and stabilizing it.

Through all of this, the oxygen is shown to play an important role in the structure, stability, and dynamics of the (3 × 1)-O Nb(100) surface. Its stabilizing effect could limit diffusion across

the surface and alter the way in which tin, or other metals, can adsorb on and eventually alloy with the niobium. This should inform existing and new procedures for the creation of niobium-alloy materials for SRF cavities.

5.2 Future Directions

There are many exciting future directions for HAS and the (3 × 1)-O Nb(100) surface. Recent theory work has revealed a direct connection between elastic helium scattering intensity and EPC constants,[90] which builds on past work showing a correlation between EPC strength and inelastic helium scattering intensity.[89] Helium scattering involves an exchange of energy with surface phonons that is mediated by free electrons, giving it an intrinsic ability to measure EPC strength. Manson et al. showed that the EPC constant, λ, is directly proportional to the Debye-Waller (DW) exponent.[90] The DW exponent, in turn, is a measure of how much an increase in surface temperature attenuates elastic helium scattering signal, and it is determined by analyzing the intensity decay of a diffraction peak over a range of temperatures. This connection between the DW factor and EPC constants has been used to explore various surfaces, from metallic overlayers to topological insulators and two-dimensional materials.[100–102] However, to our knowledge, HAS has yet to be used to determine the EPC constants of niobium and niobium alloys.

With the crystal preparation techniques learned and explained in **Chapter 2**, diffraction intensity from the (3 × 1)-O Nb(100) surface could become high enough to compare specular intensities accurately, without interference from background. The DW factor then could be determined, and the surface's EPC constant obtained. This technique can be used with a variety of surface conditions and alterations. Leaking nitrogen, hydrogen, or oxygen into the chamber before scattering would cause surface adsorbates, overlayers, and disorder; the EPC constants of these

surfaces would inform the SRF community of the impact surface disorder has on a SRF cavity's superconducting properties and performance.

Surface diffusion is another interesting property that HAS can explore. When an atom or molecule diffuses across a surface, it creates a moving target for the helium atom. This causes slight variations in the helium atom's velocity as it scatters from the surface.[103] Since most diffusion happens on a timescale amenable to the resolution of HAS instruments, TOF measurements will pick up these variations through a broadening of the specular peak. This broadening, once instrument resolution is accounted for, can be used to characterize the type and extent of surface diffusion: this technique is called quasielastic helium atom scattering (QHAS). The relationship between energy broadening and surface momentum transfer indicates whether diffusion occurs continuously or through jumps. While experimental results can be rather difficult to interpret since the broadening can be small, a combination of QHAS and molecular dynamics simulations would reveal the full picture.[103]

Going forward, QHAS can be used to determine how oxygen diffuses across the (3 × 1)-O Nb(100) surface at elevated temperatures, as well as how additional adsorbed oxygen diffuses. Another interesting experiment would be to evaporate a very small amount of tin onto the (3 × 1)-O Nb(100) surface and use QHAS to characterize the initial diffusion that occurs during tin deposition procedures.

And finally, as niobium-tin alloying techniques continue to improve and the creation single-crystal Nb_3Sn samples becomes feasible, all of the powerful techniques available to HAS can be used to explore this surface thoroughly. Elastic scattering can monitor surface structure and stability; inelastic scattering can determine phonon band structures; DW experiments can look at EPC constants; and QHAS can track the diffusion of atoms and molecules across the surface. This

will reveal further how physical processes occur in nature while also impacting the construction and performance of SRF cavities and accelerators.

Appendix A

Rapid Laser-Induced Temperature Jump Decomposition of the Nerve Agent Simulant Diisopropyl Methylphosphonate under Atmospheric Conditions

This appendix presents work done in collaboration with members of the Sibener group at The University of Chicago: it examines the destruction of the nerve agent simulant diisopropyl methylphosphonate (DIMP) by laser heating under atmospheric conditions. My role in this project was to construct the instrument used to perform the experiments. In summary, the instrument consists of an atmospheric chamber in which the DIMP, on a graphite substrate, was ablated by a Nd:YAG laser. A capillary leads from the atmospheric chamber to a vacuum chamber containing a quadrupole mass spectrometer (QMS). The atmospheric chamber can be filled with N_2 through a leak valve, creating an O_2-deprived environment. A detailed description of the instrument is included in Section A.2 in a modified version of the published manuscript for this project.

Abstract

We present work detailing the destruction of the nerve agent simulant DIMP via rapid laser heating under atmospheric conditions. Following Nd:YAG laser ablation of liquid DIMP deposited on a graphite substrate, both parent and product fragments are transmitted via capillary from an atmospheric chamber to a vacuum chamber containing a high-resolution mass spectrometer (MS). This allows for real-time measurements of product distributions under a variety of temperature and atmospheric conditions. Ex-situ Fourier transform infrared (FTIR) spectroscopy analysis of the same chamber contents provides complementary information about product identities and fragmentation pathways. Results demonstrate that product distributions depend on heating rate,

surface temperature, and atmospheric oxygen content. In the destruction of DIMP, the relative production of alkene products depends significantly on laser power: smaller products are relatively more abundant at higher ablation temperatures. We also show that in the absence of atmospheric oxygen, the concentration of oxygenated products decreases sharply relative to alkene and alkane products. This suggests that under high-temperature conditions, atmospheric oxygen is incorporated directly into the products of the fragmented simulant. This project significantly extends our understanding of the fundamental chemistry of these dangerous compounds under atmospheric and rapidly changing thermal conditions. The results have critical implications for the development of effective chemical warfare agent decontamination and destruction strategies.

A.1 Introduction

Due to the threat chemical warfare agents (CWAs) pose to the global community, there is considerable interest in detecting, destroying existing stockpiles of, and decontaminating areas affected by these compounds.[104,105] Current large-scale destruction techniques include incineration[106] and neutralization by base hydrolysis, but these strategies come with additional challenges regarding safe transport and toxic byproducts.[107] Therefore, it remains necessary to continue developing new strategies and understanding the exact chemistry of agents' destruction in both vapor and condensed phases. Of particular interest are the extremely dangerous organophosphonate nerve agents soman and sarin.[108] Sarin, for example, has a high estimated toxicity of 35 mg min m^{-3} in humans via vapor inhalation.[109] Even beyond these dangerous compounds, many less toxic organophosphonates have found widespread industrial use as plasticizers, flame retardants, fire-resistant fluids and lubricants, and pesticides.[110,111] Consequently, it is important to characterize environmental impacts and remediation strategies for

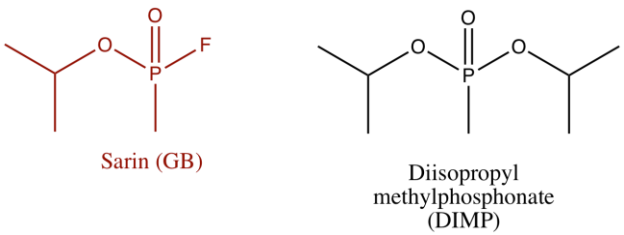

Figure A.1: The chemical structures of the nerve agent sarin (red) and the simulant DIMP (black) differ only in the replacement of fluorine with an additional O and isopropyl group.

organophosphonate contaminants more broadly. This study adds to our fundamental understanding of the primary chemical kinetics and physical processes occurring when these compounds are exposed to rapid heating under atmospheric conditions.

This appendix presents a detailed investigation of the laser-induced, high temperature rapid heating destruction of the nerve agent simulant DIMP (Figure A.1).[112–114] DIMP was selected from among the class of organophosphonate simulants for two reasons. First, DIMP shares key structural similarities with the nerve agent sarin, which is a compound of particular interest due in part to its use in urban terror attacks in Japan and its exposure to US troops abroad.[107,112] Second, it has been shown in a number of pyrolytic and thermal studies that a significant organophosphonate destruction channel yields substituted and unsubstituted carbon products resulting from the alkoxy moiety.[114–121] This gaseous product array is easily detectible and differentiable via mass spectrometry and FTIR analyses, which enables a robust investigation of the impact of laser heating rate, surface temperature, and atmospheric pressure on simulant destruction.

In addition to experimental and theoretical work on the thermal decomposition and combustion of these compounds,[114,115,120,122,123] this work is an extension of previous studies examining oxidative[124,125] and laser destruction[126] of adsorbed chemical nerve agent simulants under UHV conditions. The oxidative destruction of DIMP and dimethyl methylphosphonate

(DMMP) progress at similar rates and yield O- and carbonyl-containing oligomeric product species.[124,125] Laser desorption and destruction studies of a number of sarin simulants (DIMP, DMMP, and diethyl ethylphosphonate) demonstrated lower temperature thresholds for the destruction of simulants with relatively larger phosphonate side chains.[126] On the basis of these results, we expect that the majority of gas phase products in this study will include a variety of one, two, and three-C products generated from the DIMP isopropyl group, with possible incorporation of atmospheric O.

Using a unique atmospheric pressure ablation chamber, rapid laser heating of 10^{11} K s^{-1}, and in-situ mass spectrometry, the experiments in this appendix probe the reaction products in the prompt destruction of DIMP under atmospheric and, for the first time, O-depleted atmospheric conditions. In addition to identifying product branching ratios as a function of laser power, the manipulation of O content allows us to elucidate the mechanistic role of O in simulant destruction. This basic understanding is critical for practical decontamination strategies that involve, for example, flame incineration, as these conditions often lead to significant O depletion in the local environment.[127]

In the laser-induced thermal destruction of DIMP, we demonstrate that the resulting product distribution is dependent on both surface-temperature rise and atmospheric O composition. More specifically, the relative production of small alkene products depends on laser power: the relative yield of smaller substituted products is higher when the sample is ablated with higher laser powers. Likewise, under O-depleted conditions, the relative amount of oxygenated products decreases sharply relative to alkene and alkane products. This suggests that under extreme high-temperature conditions, atmospheric O is incorporated directly into the products of the fragmented simulant. Such findings are relevant directly to producing novel chemical warfare agent mitigation

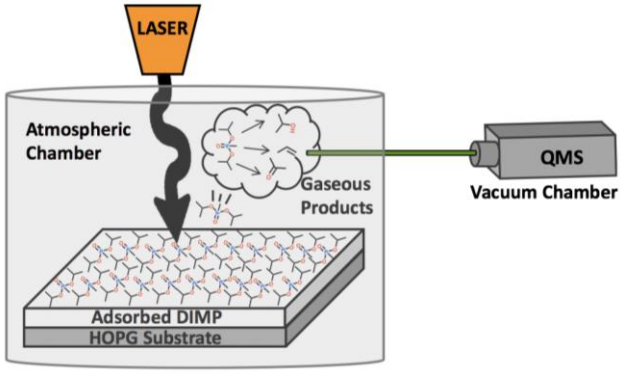

Figure A.2: Laser ablation experiments were conducted in a joint atmospheric and high vacuum apparatus. A Nd:YAG laser was used to ablate DIMP simulant films in an atmospheric chamber; gaseous products were transported via capillary (green) to a high-vacuum chamber containing a QMS for analysis.

strategies and maintaining national security.

A.2 Experimental

All experiments in this appendix were conducted in a newly constructed atmospheric-mass spectrometry apparatus, shown in Figure A.2. Additional measurements were collected via ex-situ FTIR analysis. In short, a QMS (UTI 100) occupies a high-vacuum chamber reaching base pressures of 10^{-9} Torr, pumped by a 90 L/s turbo pump (Leybold, Turbovac 90 i) backed by a 24 m^3/h rotary vein pump (Pfeiffer, Duo20M). The QMS is controlled through LabVIEW^{TM} software (National Instruments, LabVIEW^{TM} 2015). This chamber samples, via a 20 cm fused silica capillary with a 25 μm inner diameter, the gaseous products produced in a small, adjacent atmospheric chamber used for laser ablation trials. A second identical inlet capillary in the atmospheric chamber ensures that atmospheric pressure is maintained during experimental sampling. The volume of the atmospheric sampling chamber is small (approximately 40 cm^3), which enables rapid diffusion of vapor products; changes in chamber contents are detected by the

MS within 300 ms. We do note that the capillary is not heated, so there is a possibility for vapor condensation of DIMP or associated products during transport. Gas phase products, however, are expected to thermalize rapidly in the atmospheric chamber, so we do not expect condensation in the capillary to be a major pathway. The large pressure differential between the two chambers also ensures consistent gas flow through the capillary, and repeated use of the same capillary showed no blockage, indicating that condensation was not happening on a large scale.

In order to prepare DIMP samples for ablation, we routinely purged the atmospheric chamber and re-opened to atmosphere between trials. The substrate for all experiments was a highly ordered pyrolytic graphite crystal (HOPG, Bruker). In addition to purging the chamber, we exfoliated the HOPG surface between trials to ensure reproducible surface quality and composition. To begin each experiment, we deposited 10 μL of DIMP (Alfa Aesar) on the HOPG surface and sealed the chamber. A background mass scan was then collected; final product analysis was performed on the background-subtracted spectra collected following ablation.

We ablated DIMP films with a Nd:YAG laser (Quanta-Ray, GCR 130) producing near-IR photons at 1064 nm. To estimate the surface temperature on the HOPG substrate induced by the laser pulse, the following calculation was carried out for one-dimensional heat flow into a semi-infinite slab of material (transverse propagation of the beam is large compared to the depth of heat conduction into the film). Assuming that the optical absorption coefficient of HOPG is large (on the order of 10^4–10^6 cm^{-1}),[128–131] the surface temperature of the HOPG surface at time t can be calculated as:[132]

$$T(0,t) = \frac{2F_0}{K}\left(\frac{\kappa t}{\pi}\right)^{1/2}. \quad \text{(A.1)}$$

In Equation A.1, F_0 is the absorbed incident flux from the laser; K is the thermal conductivity and κ is the thermal diffusivity of HOPG, reported as 290 W m^{-1} K^{-1} and 0.000165 m^2 s, respectively.[133]

In practice, we first measure the total pulsed laser power with a calorimeter (Scientech, Model 38-0101). This output is converted to pulse energy by incorporating the pulse frequency (20 Hz) and scaling to the duration of individual pulses (8 ns): pulse energies in this study range from 0.103 J to 0.244 J. We further scale the total flux to the reflection coefficient of HOPG (reported as 0.21 at 300 K).[128] With this model, peak laser powers raise the crystal temperature to approximately 2830 ± 110 K at a heating rate of 3.2×10^{11} K s^{-1}. The error cited for temperature is a standard propagation including error from the calorimeter measurement, pulse width, and HOPG reflection coefficient. We note that simulant films were ablated for 2 minutes at 20 Hz in order to generate sufficient product signal for analysis. However, product signals (propene at $m/z = 41$, for example) were detected for single pulse ablations, and thermocouple measurements of the HOPG crystal show a steady-state temperature rise of only approximately 350 K from the extended ablation. We therefore assume that the modest temperature rise caused by extended ablation is negligible compared to the high temperature rise during each individual pulse.

Mass spectra analyses involved a series of steps illustrated with representative data in Figure A.3. To begin, background spectra were subtracted from post-ablation spectra (Figure A.3(a)). Next, the MALDIquant R package was used for data smoothing (using a 7-point Savitzky-Golay-filter, Figure A.3(b)) and peak detection.[134,135] In order to deconvolve the spectra into individual product contributions, it first was necessary to build a library of fragmentation patterns for the proposed products. To this end, mass spectra were collected for propene (Sigma Aldrich), acetone (Fisher Scientific), and isopropyl alcohol (IPA, Fisher Scientific). The spectra for additional products, ethylene and acetylene, were obtained from reference data from the National Institute of Standards and Technology (NIST).[136] Once this library was complete, the relative product contributions for the ablated spectra were determined using a least-squares analysis

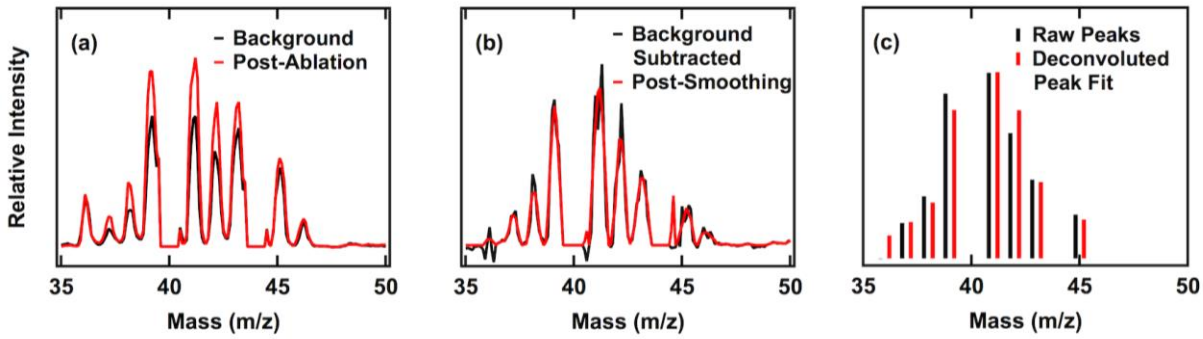

Figure A.3: Representative analysis of ablated DIMP mass spectra. First, background spectra are subtracted from post-ablation spectra (a). These background-subtracted spectra are smoothed (red, (b)) and peaks are detected (black bars, (c)). A least-squares procedure is used to determine relative product yields and reproduce the ablated spectra (red bars, (c)).

(Figure A.3(c)). We note that though present in the background-subtracted spectra, large peaks associated with atmospheric gases like N_2, O_2, Ar, etc., were excluded from this deconvolution procedure due to the difficulty of separating trace product signals from atmospheric contributions. The omission of $m/z = 27$ and 28 in particular made it difficult to distinguish ethylene and acetylene. Therefore, all discussions herein will group these two-C products together.

In addition to mass spectrometry, a second modular chamber was used for concurrent ex-situ FTIR analysis of ablated products. To begin these experiments, we purged a 150 cm^3 IR cell with ZnSe windows to approximately 25 mTorr. We then connected this chamber via leak valve to an analogous atmospheric chamber for simulant ablation. Following the ablation procedure, the valve was opened, allowing the evolved gaseous products to escape into the purged chamber. The contents of the unheated chamber were analyzed using an infrared spectrophotometer (Thermo Fisher, Nicolet iS50) and a liquid-nitrogen-cooled MCT/A detector. We averaged all such FTIR spectra over 200 scans at 4 cm^{-1} resolution; peak fitting analysis utilized Gaussian peaks atop cubic baselines.

A.3 Results and Discussion

A.3.1 FTIR Product Analysis

Previous investigations into the thermal destruction of DIMP consistently have identified a number of products, including propene, IPA, and ethylene. These studies include destruction via pyrolysis, combustion, exposure to a corona discharge, dissociative adsorption, laser ablation, and so on.[104,114,115,137–139] While this provides a reasonable set of products to look for, the work in this appendix represents the first direct study of rapid laser heating (on the order of 10^{11} K s^{-1}) of adsorbed liquid DIMP under atmospheric pressure and O-depleted conditions. It therefore is necessary to establish firmly the full range of products before attempting to assess branching ratios; this was done using ex-situ FTIR. Representative spectra of ablated DIMP in Figure A.4 show clear evidence of propene, ethylene, acetylene, as well as contributions from unreacted DIMP or other partially decomposed organophosphonate fragments such as isopropyl methylphosphonate (IMP). In addition to the prominent phosphonate P-O-C stretching modes at 995 and 1020 cm^{-1}, we observe significant signal intensity from propene's $=CH_2$ wagging mode (912 cm^{-1}) and the bending modes of acetylene and ethylene (730 cm^{-1} and 949 cm^{-1}, respectively). All peaks referenced herein are consistent with those reported for the corresponding molecules in the gas phase.[113,136,140–145] CO also is observed, but this is difficult to assign uniquely to either DIMP or HOPG ablation. Additionally, other small product peaks are observed in the spectra beyond those highlighted in Figure A.4, but we were not able to clearly establish their identities using FTIR alone.

In both FTIR and the following MS analyses, we note that the scope of our experiment did not include direct quantification of condensed-phase products, or of parent molecules remaining on the HOPG substrate or in the atmospheric chamber. Similar to other studies, however, our gas-

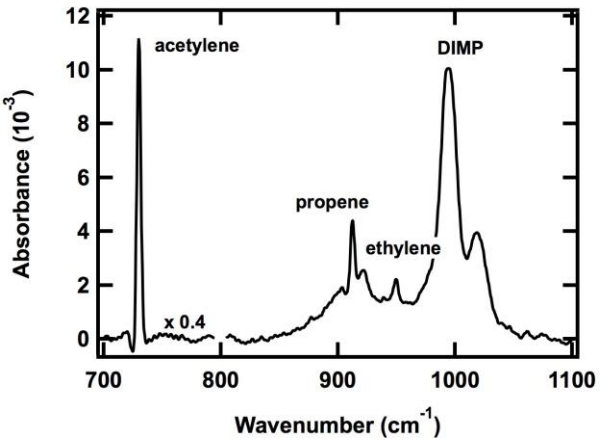

Figure A.4: A representative FTIR spectrum of DIMP ablated to approximately 2720 K, showing clear evidence of residual DIMP as well as acetylene, propene, and ethylene products.

phase product analysis suggests that it is primarily phosphorus-containing products that remain following thermal destruction.[114,146] In addition to unreacted DIMP, these products likely include IMP and methylphosphonic acid (MPA).

As laser power (and thereby HOPG surface temperature) is increased, an interesting trend emerges in the relative distribution of products. When spectra are normalized to the height of the propene peak, there is a corresponding relative increase in the height of ethylene (Figure A.5(a)). If the relative areas of these two peaks are plotted as a function of HOPG surface temperature (Figure A.5(b)), it becomes clear that as the ablation temperature increases, ethylene production increases relative to propene. The same trend is observed for relative propene and acetylene production. Without precise absorption cross-sections for these compounds, it is difficult to quantify the absolute amount of each product formed. It is clear, however, that higher temperatures lead to a higher yield of smaller substituted C products.

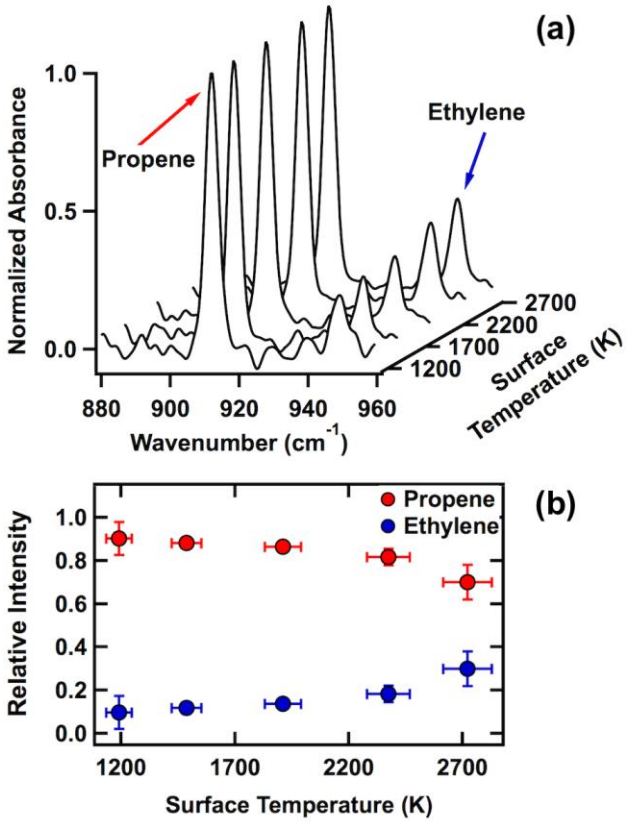

Figure A.5: Relative production of ethylene and propene as a function of laser ablation power. FTIR spectra normalized to propene height (a) demonstrate increases in relative ethylene production as surface ablation temperature increases. Baseline and other product peaks have been subtracted for clarity. The relative integrated areas of the associated peaks (b) show that this trend is observed throughout the temperature range explored in this study (error bars represent the standard deviation of at least three trials at each ablation temperature).

A.3.2 Effects of Varying Surface Temperature

The results described in the preceding section were replicated easily with in-situ mass spectrometry. However, it is important to note that the mass spectra data reveal some additional minor products unidentified in the FTIR data. FTIR spectra provided no conclusive evidence of oxygenated ablation products, despite their suggested presence in other pyrolytic and thermal decomposition studies of DIMP.[115,137,138] Background subtracted mass spectra of ablated DIMP, however, show clear increases in $m/z = 43$ and $m/z = 45$ (acetone and IPA, respectively). The

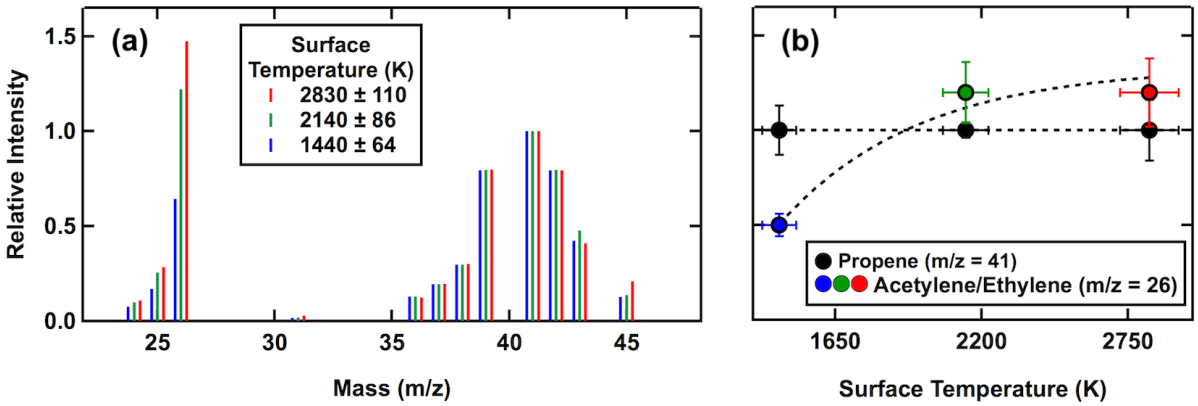

Figure A.6: Reproduced representative mass spectra (a) from a least-squares fit of the data (normalized to the propene signal at $m/z = 41$) show an increase in low molecular weight products (ethylene and acetylene) as laser power is increased. This also can be seen in the normalized relative intensities of propene and acetylene/ethylene ($m/z = 26$) averaged across all trials (b). Ablation surface temperatures are 1440 K (blue), 2140 K (green), and 2830 K (red). The dotted line is drawn to guide the eye.

yield of both of these products consistently is small relative to propene and ethylene/acetylene, so their absence in FTIR spectra may simply be due to a lack of sensitivity. Therefore, mass spectra are deconvoluted into contributions from four observed products: propene, ethylene/acetylene, acetone, and IPA. Figure A.6 shows the least-squares fit for the data collected in three representative trials at different ablation powers. When the data are normalized to the propene signal ($m/z = 41$), there is a clear corresponding relative increase in the amount of the smaller acetylene and ethylene products. In other words, these results again suggest that peak surface temperatures impact the extent of bond cleavage and identity of destruction products.

A.3.3 Effects of Varying Atmospheric Oxygen

In order to probe the role of atmospheric O in DIMP destruction, we performed a series of experiments with variable partial pressures of O. Following simulant deposition, the sampling

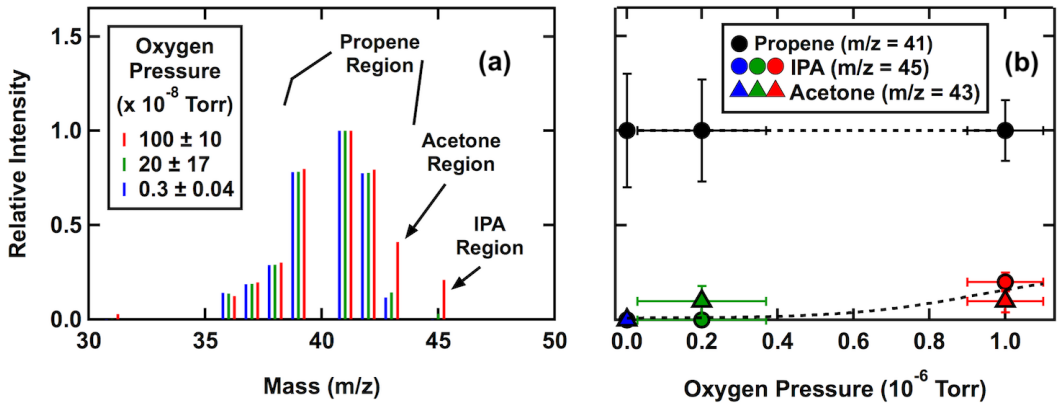

Figure A.7: Reproduced representative mass spectra (a) from a least-squares fit of the data (normalized to propene signal at $m/z = 41$) show a sharp decrease in oxygenated products as available O decreases. This also can be seen in the normalized relative intensities of propene, IPA ($m/z = 45$), and acetone ($m/z = 43$) averaged across all trials (b). Recorded O pressures in the QMS chamber were 1×10^{-6} Torr under atmospheric ablation conditions (red), 2×10^{-7} Torr under low O conditions (green), and 3×10^{-9} Torr under O-depleted conditions (blue). The dotted line is drawn to guide the eye.

chamber was purged carefully with N_2 until a desired O pressure was reached (as measured with the QMS). The chamber, however, was still maintained at atmospheric pressure. After ablation at the highest laser powers, the results in Figure A.7 show that the presence of oxygenated products plummets nearly to zero when atmospheric O is reduced. Signals associated with both acetone ($m/z = 43$) and IPA ($m/z = 45$) decrease sharply relative to propene ($m/z = 41$). This observation is of critical importance: it demonstrates clearly that atmospheric O is incorporated directly into the fragmenting DIMP molecule.

A.3.4 Mechanism of Destruction

The effects of varying both ablation surface temperature and atmospheric composition are summarized in Table A.1. Each entry represents the average of at least three similar trials. In brief,

Chamber Conditions		Relative Product Contributions			
Oxygen (Torr)	***Surface Temp (K)***	***IPA***	***Acetone***	***Propene***	***Ethylene/Acetylene***
$(1 \pm 0.1) \times 10^{-6}$	2830 ± 110	0.2 ± 0.05	0.1 ± 0.06	1 ± 0.16	1.2 ± 0.18
$(1 \pm 0.1) \times 10^{-6}$	2140 ± 86	0.2 ± 0.03	0.1 ± 0.12	1 ± 0.04	1.2 ± 0.16
$(1 \pm 0.1) \times 10^{-6}$	1440 ± 64	0.1 ± 0.08	0.4 ± 0.13	1 ± 0.13	0.5 ± 0.06
$(1 \pm 0.1) \times 10^{-6}$	2830 ± 110	0.2 ± 0.05	0.1 ± 0.06	1 ± 0.16	1.2 ± 0.18
$(2 \pm 1.7) \times 10^{-7}$	2830 ± 110	0 ± 0.03	0.1 ± 0.08	1 ± 0.27	4.2 ± 0.86
$(3 \pm 0.4) \times 10^{-9}$	2830 ± 110	0 ± 0.0	0 ± 0.0	1 ± 0.3	7 ± 1.49

Table A.1: Summary of all DIMP ablation experiments performed, normalized to propene production. As surface temperature is increased, the relative ratio of ethylene and acetylene to propene increases. As available O is decreased, the relative production of IPA and acetone decreases.

we observe that higher ablation temperatures lead to an increase in the relative production of shorter chain substituted products (ethylene/acetylene vs. propene). Additionally, a reduction in available atmospheric O leads to a decrease in the relative production of oxygenated products (acetone and IPA vs. propene). These results inform the following discussion of the mechanisms underlying the thermal destruction of condensed-phase DIMP.

To begin, it has been proposed experimentally and theoretically that the primary pyrolytic destruction step for DIMP and other similar molecules is a unimolecular decomposition to IMP and propene via a six-membered ring transition state.[114,147–149] Moreover, propene production has been observed under a variety of high temperature conditions, beginning with temperatures as low as 700 K, which is lower than the ablation range studied here.[114,126] In vacuum studies, propene is also produced as a result of dissociative adsorption of DIMP.[116,139] Essentially, many studies agree that a major step in DIMP destruction involves the formation of propene. On the other hand, few studies have identified direct mechanisms that yield smaller substituted products from DIMP's initial dissociation (and indeed no single initial bond scission is enough to yield a two-C product

from DIMP directly). Instead, it is likely that the smaller products (ethylene, acetylene, methane, etc.) are produced as secondary destruction products of propene.[150,151] The results of this work present evidence that propene likely is one of the first products, and that higher ablation temperatures increase the relative extent of further fragmentation.

The results of the O study add interesting detail to the existing mechanistic picture. Zegers and Fisher proposed a two-step pyrolysis mechanism for DIMP, beginning with the unimolecular decomposition that yields propene. The second step involves transfer of a H from the phosphorous hydroxyl group to the O of the isopropoxy group, yielding IPA and methyl dioxophosphorane.[114,115] Our observations suggest, however, that this intermolecular step may not be the primary mechanism for IPA formation at these high-temperature, fast-heating, and condensed-phase conditions. Instead, atmospheric O_2 or radicals formed from thermal dissociation may abstract hydrogens or break bonds in the DIMP molecule directly. For example, if an alkyl radical forms upon scission of the P-O-C bond, atmospheric O_2 can add readily to generate an alkoxy radical. This species, in turn, is expected to react or decompose to form both the observed acetone and IPA.[152–154] The direct incorporation of O from the atmosphere in this proposed mechanism would account for the observed dependence on O pressure in the ablation chamber in the production of oxygenated products.

A.4 Conclusion

Building on work investigating pyrolysis, dissociative adsorption, and laser ablation of chemical warfare agents and their simulants, this study presents a comprehensive look at rapid thermal ablation of condensed DIMP, a simulant of sarin, under atmospheric pressure conditions. Decomposition products observed include propene, ethylene, acetylene, IPA, and acetone, which

are well in line with existing literature on thermal destruction of organophosphonates. Product distributions varied significantly when both laser power (HOPG surface temperature) and O content were altered: higher ablation powers led to higher temperatures, which increased the extent of secondary fragmentation in alkene and alkyne products observed. Lower O partial pressures led to a sharp decrease in oxygenated products, suggesting that a dominating mechanism in this system involves direct incorporation of atmospheric O_2 into product fragments.

Though sarin, unlike DIMP, includes a fluorine substituent on the central phosphorus atom, there is reason to believe that the results highlighted here have direct relevance for sarin's thermal destruction. Experimental work with simulants and nerve agents has shown significant correlation between bond frequency and desorption energies, suggesting that simulants like DIMP are indeed appropriate for modeling the chemistry of toxic agents.[112] Perhaps more importantly, pyrolytic simulations of sarin have confirmed that thermal destruction begins with the same six-center intermediate that leads to propene elimination.[115] Therefore, we expect that the chemistry observed in these temperature-jump experiments is relatively generalizable to sarin and other large organophosphonates.

In addition to validating the applicability of these results on live nerve agents, extensions of this work may include tracking the destruction temperature thresholds and product distributions for additional simulants and simulant mixtures, as well as the impact of incorporating less absorptive or reactive substrates. In general, this work continues to shed light on the basic mechanisms of organophosphonate thermal destruction, related to those encountered under high temperature rapid heating blast conditions. These results are critical for the accurate modeling of environmental persistence and the implementation of mitigation strategies for chemical warfare agents and other organophosphonate pesticides.

Appendix B

Raw Data

The following appendix contains the raw data for all figures used in this thesis. The naming system is as follows: ‘B’, followed by the chapter where the data is used in a figure (i.e. ‘3’), followed by a period and then the number of the raw-data figure in the order it appears in the appendix (i.e. ‘.1’ for the first, ‘.2’ for the second, etc.). This number does not necessarily correspond with the number of the associated figure in the thesis.

The thesis figure in which the raw data is used is listed in the appendix figure’s caption.

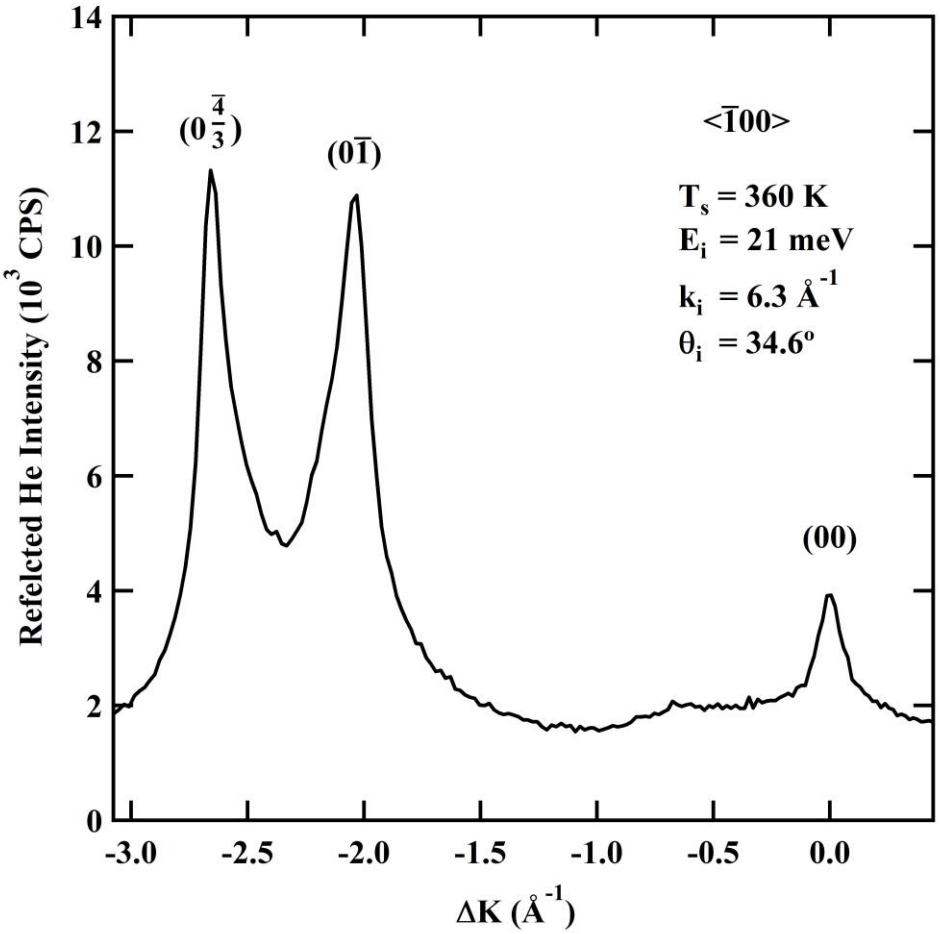

Figure B3.1: He diffraction scan from the (3 × 1)-O Nb(100) surface along the $\overline{\Gamma X}$ axis, used to create Figure 3.1.

Experiment file: Figure B3.1.pxp

Raw data file: 021720_03

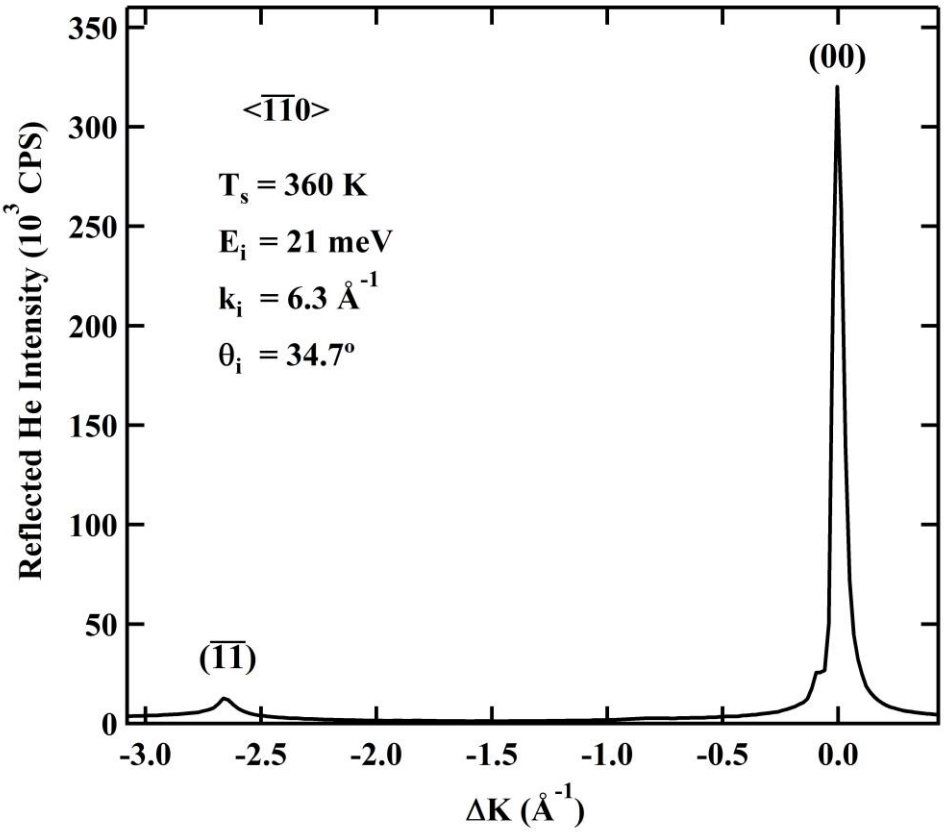

Figure B3.2: He diffraction scan from the (3 × 1)-O Nb(100) surface along the $\overline{\Gamma M}$ axis, used to create Figure 3.2.

Experiment file: Figure B3.2.pxp

Raw data file: 021820_03

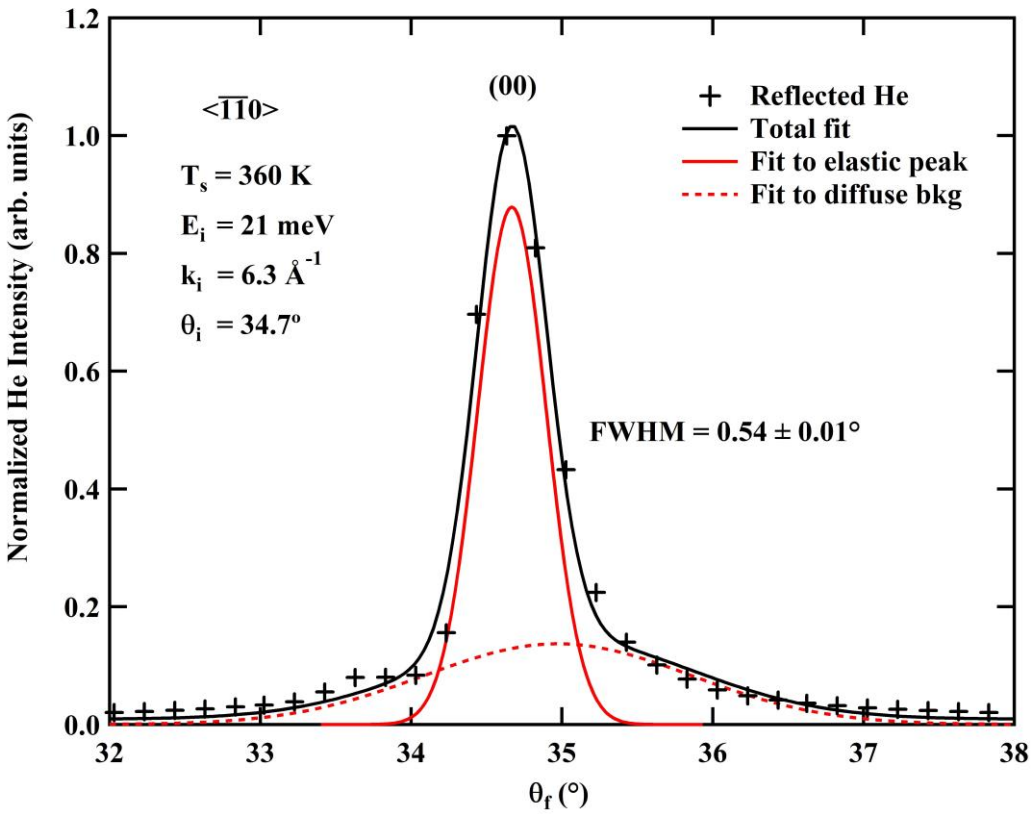

Figure B3.3: He diffraction scan from the (3 × 1)-O Nb(100) surface along the $\overline{\Gamma X}$ axis, used to create Figure 3.3. The FWHM was used as a point in Figure 3.6; Gaussian fits were found as described in Chapter 3.

Experiment file: Figure B3.3.pxp

Raw data file: 021820_03

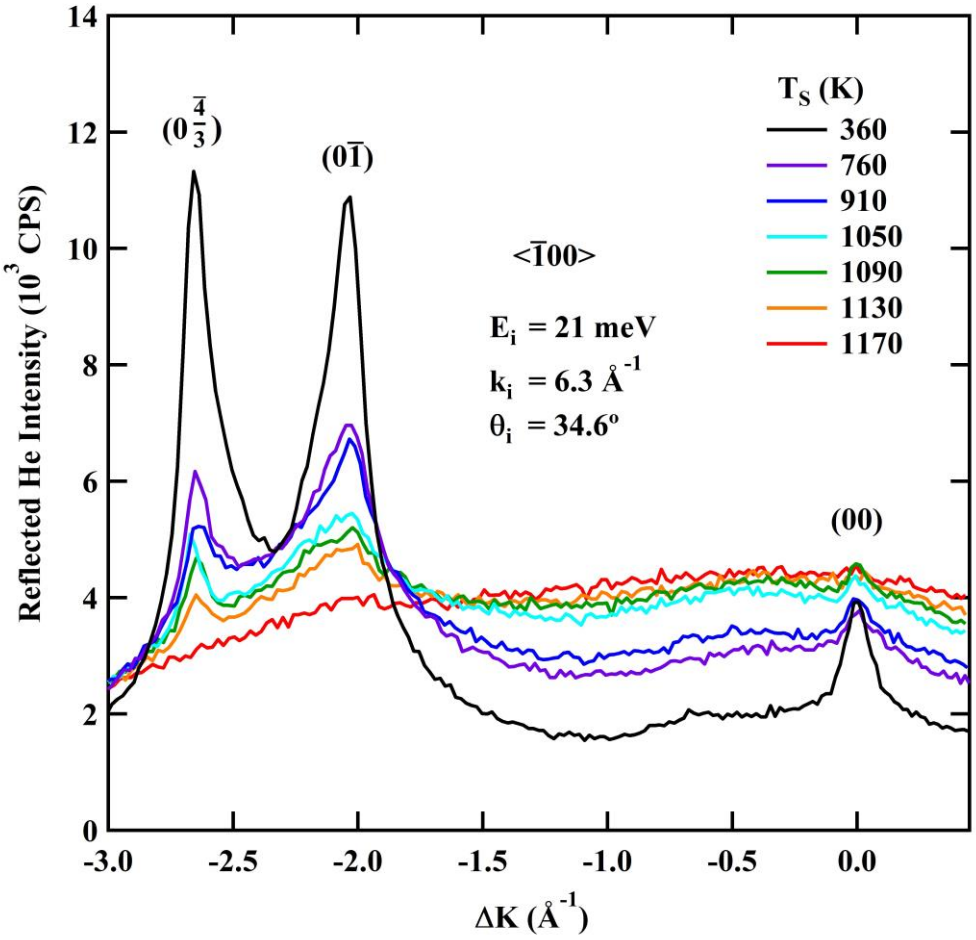

Figure B3.4: He diffraction scans from the (3 × 1)-O Nb(100) surface along the $\overline{\Gamma X}$ axis, used to create Figure 3.4.

Experiment file: Figure B3.4.pxp

Raw data files: 021720_03, 021720_05, 021720_07, 021720_09, 021720_12, 021720_14, and 021720_16

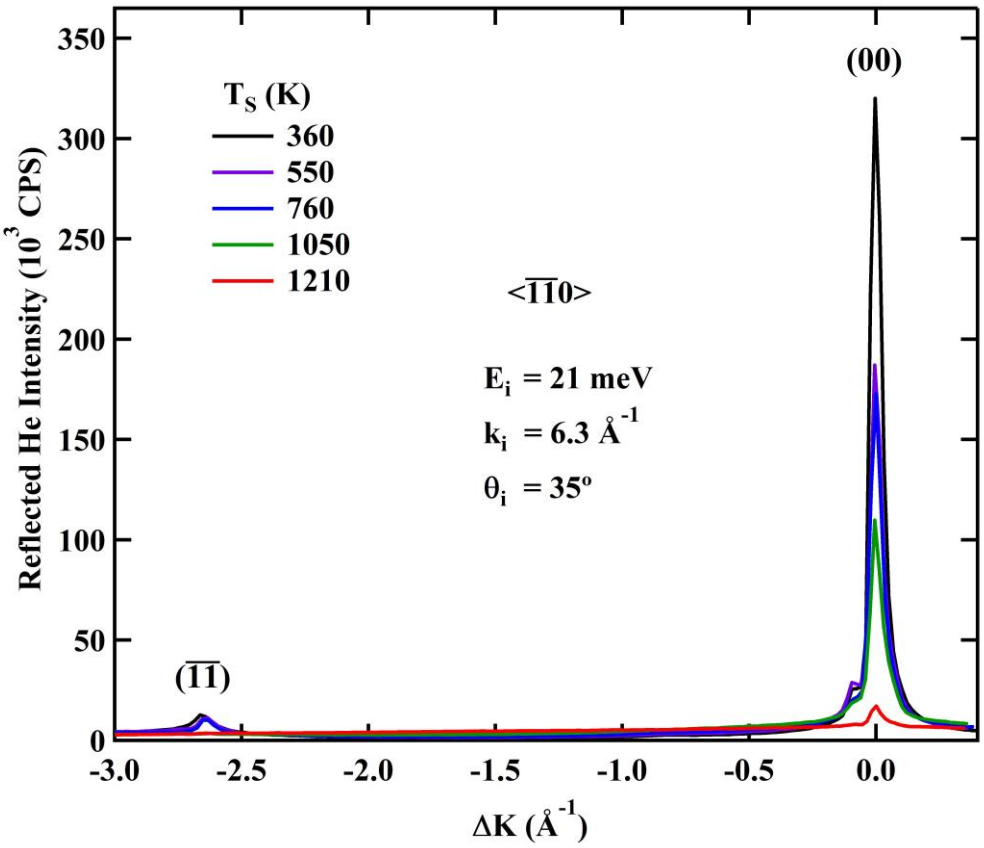

Figure B3.5: He diffraction scans from the (3 × 1)-O Nb(100) surface along the $\overline{\Gamma M}$ axis, used to create Figure 3.5.

Experiment file: Figure B3.5.pxp

Raw data files: 021820_03, 021820_04, 021820_05, 021820_06, and 021820_09

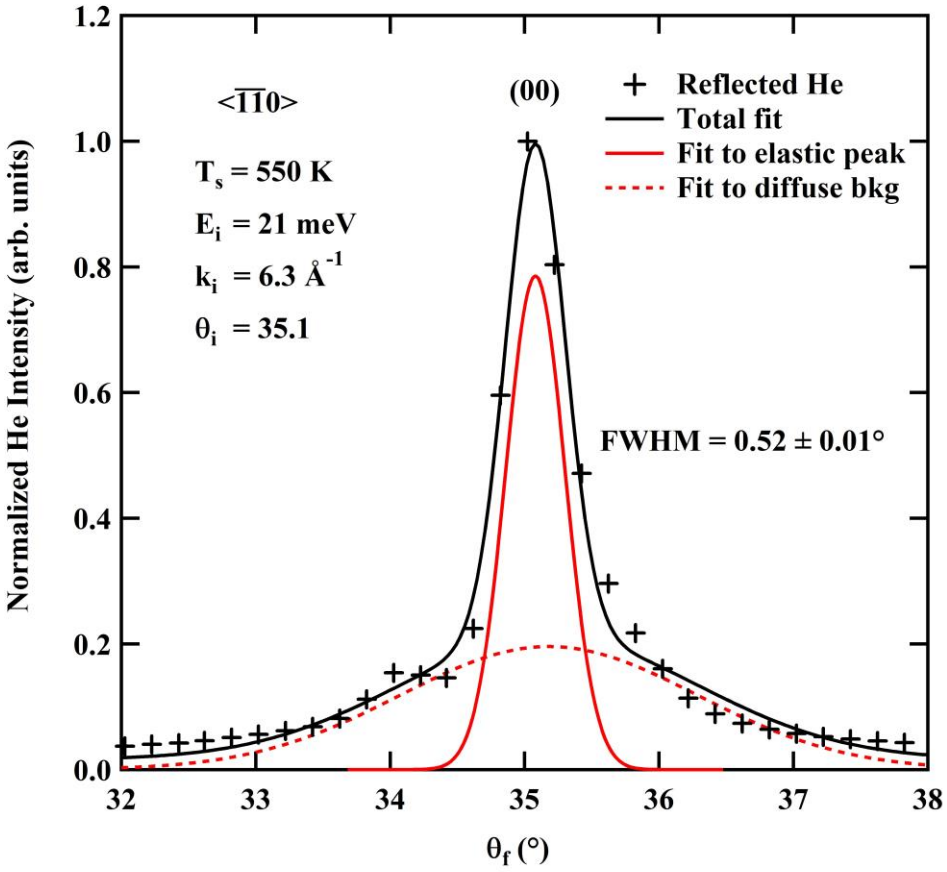

Figure B3.6: He diffraction scan from the (3 × 1)-O Nb(100) surface along the $\overline{\Gamma X}$ axis. The FWHM is used as a point in Figure 3.6; Gaussian fits were found as described in Chapter 3.

Experiment file: Figures B3.6-B3.9.pxp

Raw data file: 021821_09

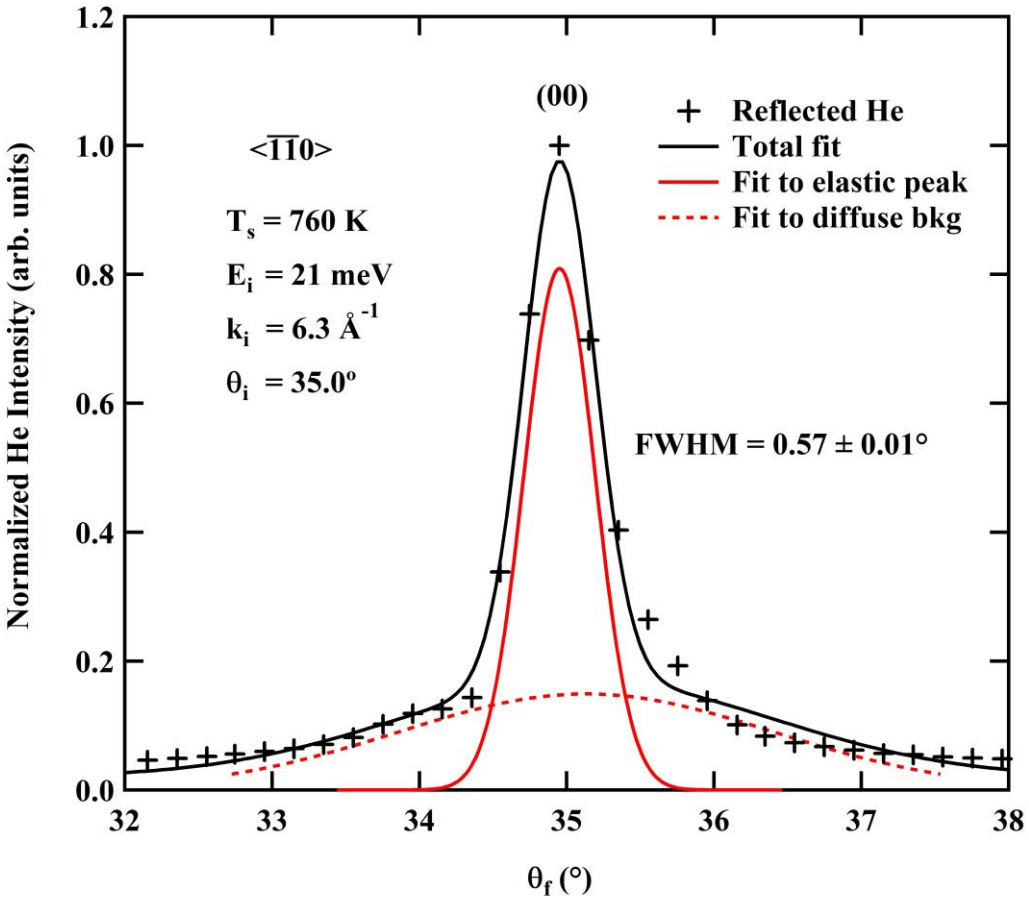

Figure B3.7: He diffraction scan from the (3 × 1)-O Nb(100) surface along the $\overline{\Gamma X}$ axis. The FWHM is used as a point in Figure 3.6; Gaussian fits were found as described in Chapter 3.

Experiment file: Figures B3.6-B3.9.pxp

Raw data file: 021821_04

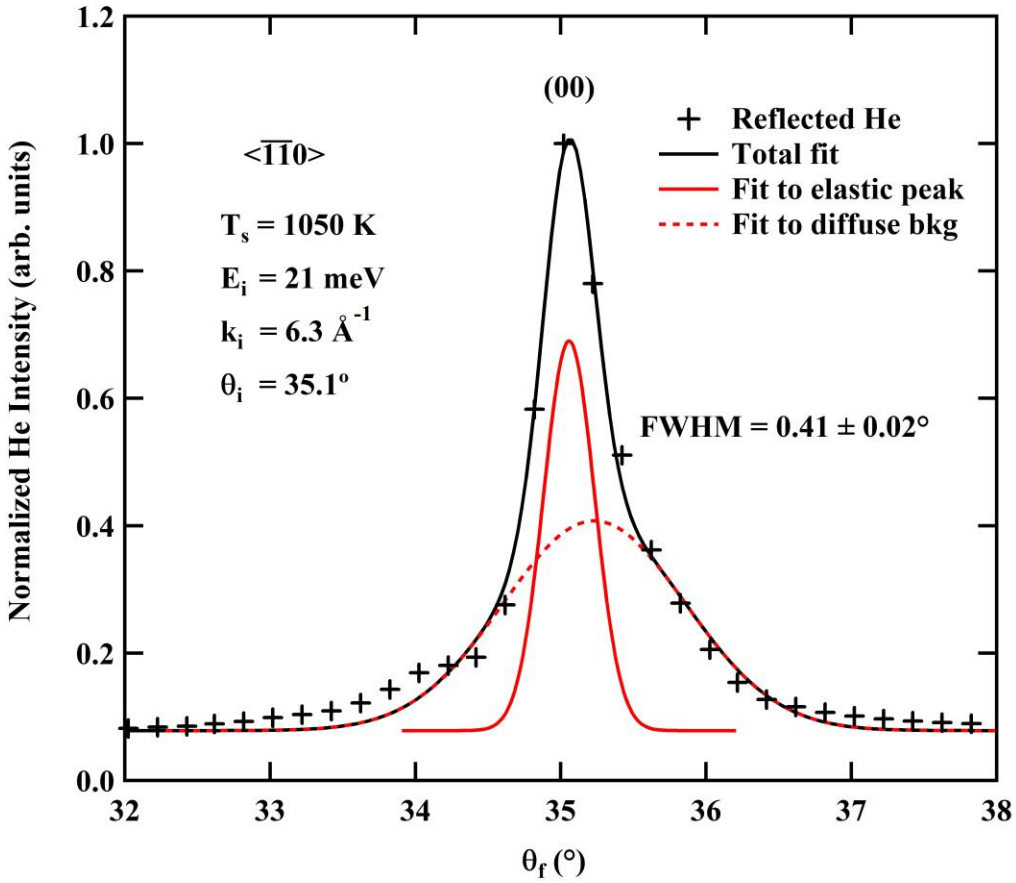

Figure B3.8: He diffraction scan from the (3 × 1)-O Nb(100) surface along the $\overline{\Gamma X}$ axis. The FWHM is used as a point in Figure 3.6; Gaussian fits were found as described in Chapter 3.

Experiment file: Figures B3.6-B3.9.pxp

Raw data file: 021821_05

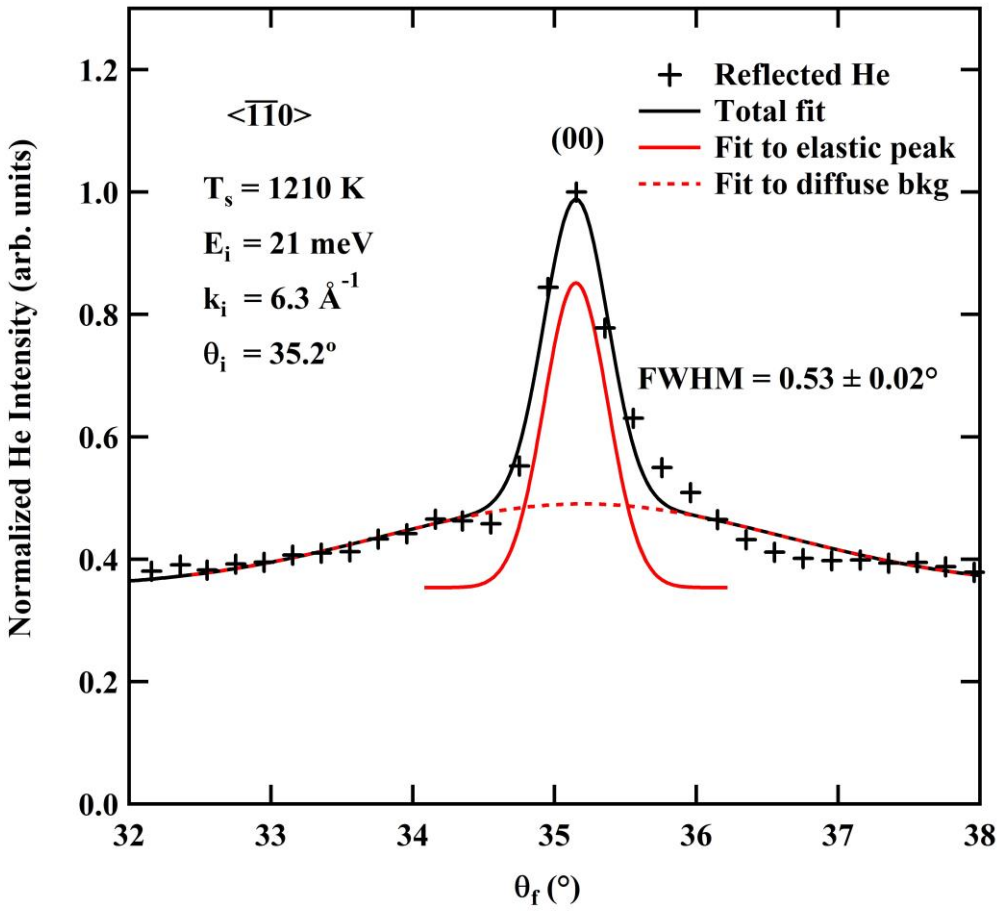

Figure B3.9: He diffraction scan from the (3 × 1)-O Nb(100) surface along the $\overline{\Gamma X}$ axis. The FWHM is used as a point in Figure 3.6; Gaussian fits were found as described in Chapter 3.

Experiment file: Figures B3.6-B3.9.pxp

Raw data file: 021821_06

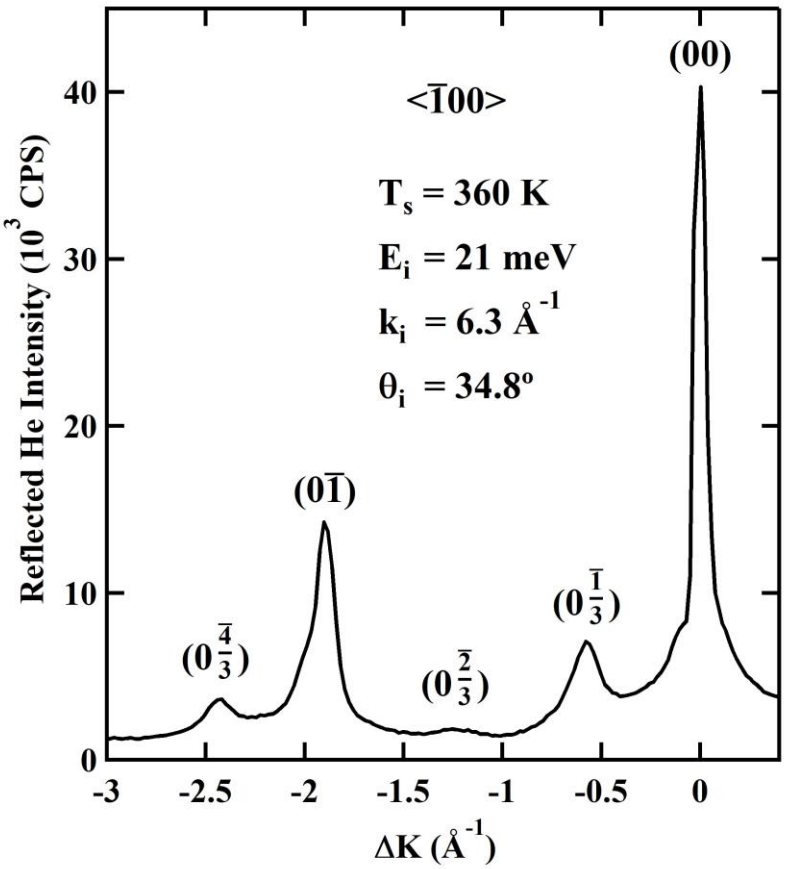

Figure B4.1: He diffraction scan from the (3 × 1)-O Nb(100) surface along the $\overline{\Gamma X}$ axis, used to create Figure 4.1(a)

Experiment file: Figures B4.1-B4.2.pxp

Raw data file: 100920_07

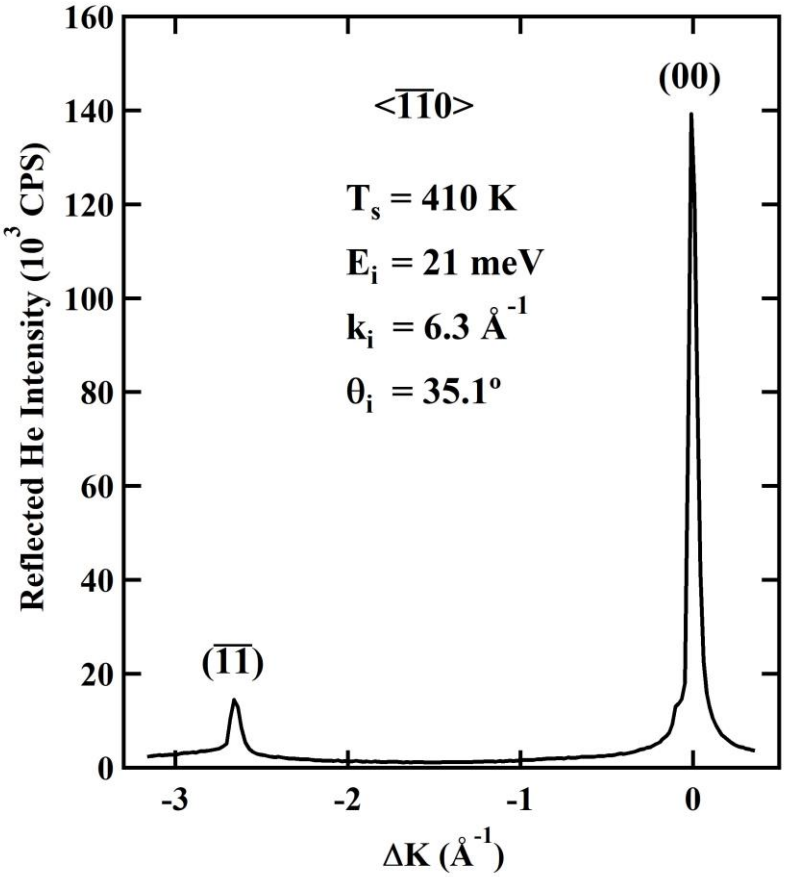

Figure B4.2: He diffraction scan from the (3 × 1)-O Nb(100) surface along the $\overline{\Gamma X}$ axis, used to create Figure 4.1(b)

Experiment file: Figures B4.1-B4.2.pxp

Raw data file: 080620_13

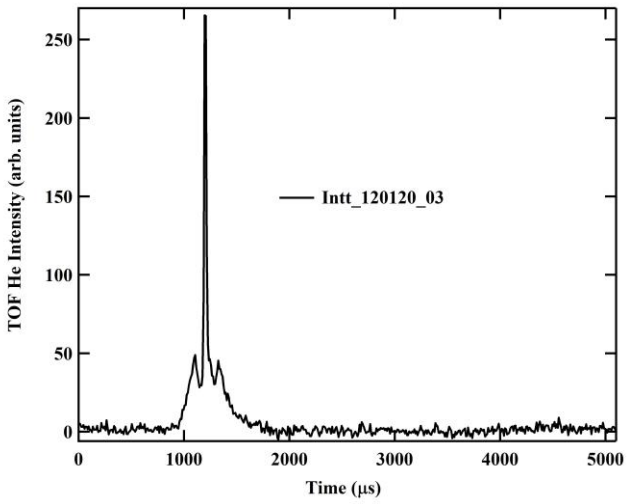

Figure B4.3: Raw He inelastic time-of-flight from the (3 × 1)-O Nb(100) surface along the $\overline{\Gamma X}$ axis; used to create Figure 4.2(a) and contributes two data points to Figures 4.4(a), 4.7, and 4.8(a). Cross-correlation spectrum taken with T_S = 670 K, E_i = 16 meV, θ_i = 27.2°, and θ_f = 38.1°.

Experiment file: Figures B4.3-B4.6.pxp

Raw data file: 120120_03

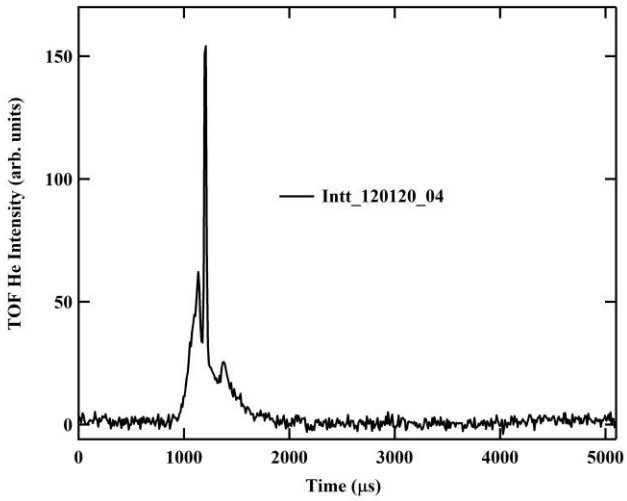

Figure B4.4: Raw He inelastic time-of-flight from the (3 × 1)-O Nb(100) surface along the $\overline{\Gamma X}$ axis; used to create Figure 4.2(a) and contributes two data points to Figures 4.4(a), 4.7, and 4.8(a). Cross-correlation spectrum taken with T_S = 670 K, E_i = 16 meV, θ_i = 27.2°, and θ_f = 42.1°.

Experiment file: Figures B4.3-B4.6.pxp

Raw data file: 120120_04

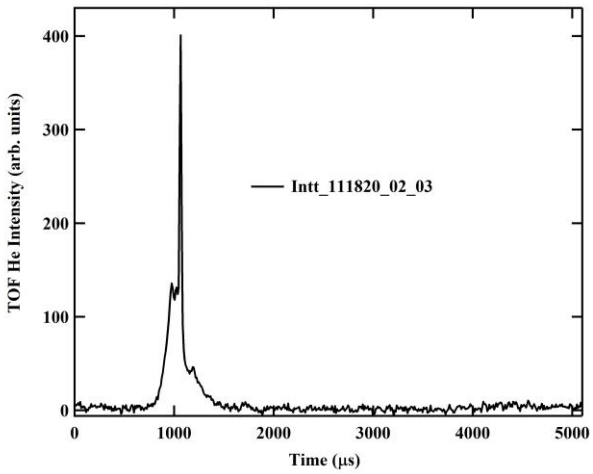

Figure B4.5: Raw He inelastic time-of-flight from the (3 × 1)-O Nb(100) surface along the $\overline{\Gamma X}$ axis; used to create Figure 4.2(b) and contributes three data points to Figures 4.4(a), 4.7, and 4.8(a). Two cross-correlation spectra taken with T_S = 670 K, E_i = 21 meV, θ_i = 34.7°, and θ_f = 23.6° and then added.

Experiment file: Figures B4.3-B4.6.pxp

Raw data files: 111820_02 and 111820_03

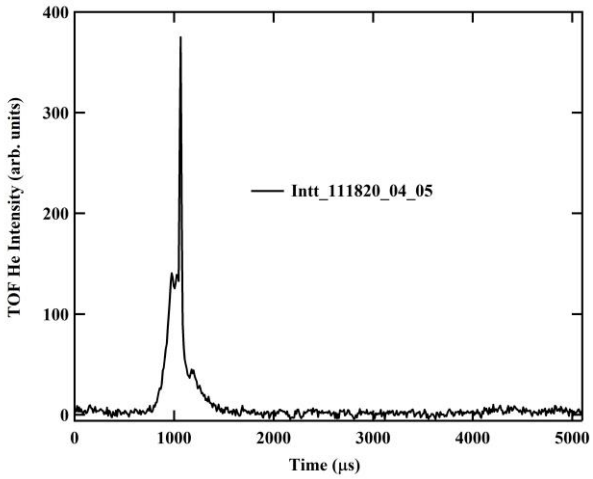

Figure B4.6: Raw He inelastic time-of-flight from the (3 × 1)-O Nb(100) surface along the $\overline{\Gamma X}$ axis; used to create Figure 4.2(b) and contributes three data points to Figures 4.4(a), 4.7, and 4.8(a). Two cross-correlation spectra taken with T_S = 670 K, E_i = 21 meV, θ_i = 34.7°, and θ_f = 24.6° and then added.

Experiment file: Figures B4.3-B4.6.pxp

Raw data files: 111820_04 and 111820_05

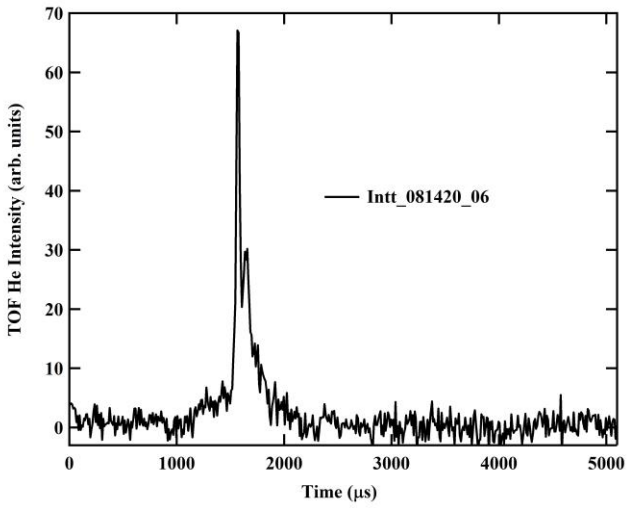

Figure B4.7: Raw He inelastic time-of-flight from the (3 × 1)-O Nb(100) surface along the $\overline{\Gamma M}$ axis; used to create Figure 4.3(a) and contributes one data point to Figures 4.4(b), 4.7, and 4.8(a). Cross-correlation spectrum taken with T_S = 410 K, E_i = 10 meV, θ_i = 21.1°, and θ_f = 25.2°.

Experiment file: Figures B4.7-B4.13.pxp

Raw data file: 081420_06

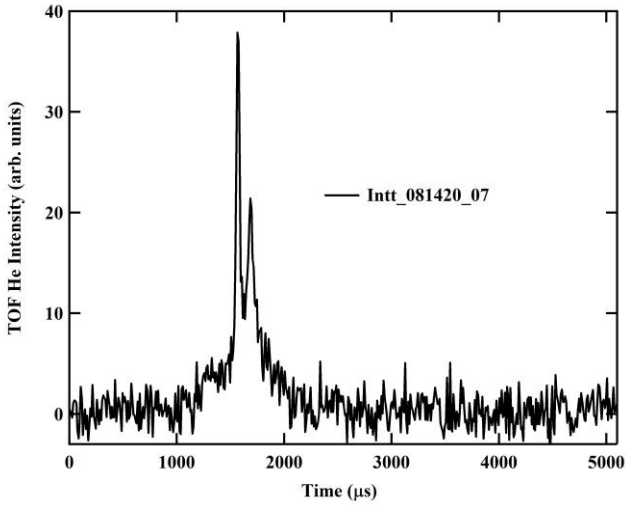

Figure B4.8: Raw He inelastic time-of-flight from the (3 × 1)-O Nb(100) surface along the $\overline{\Gamma M}$ axis; used to create Figure 4.3(a) and contributes one data point to Figures 4.4(b), 4.7, and 4.8(a). Cross-correlation spectrum taken with T_S = 410 K, E_i = 10 meV, θ_i = 21.1°, and θ_f = 27.2°.

Experiment file: Figures B4.7-B4.13.pxp

Raw data file: 081420_07

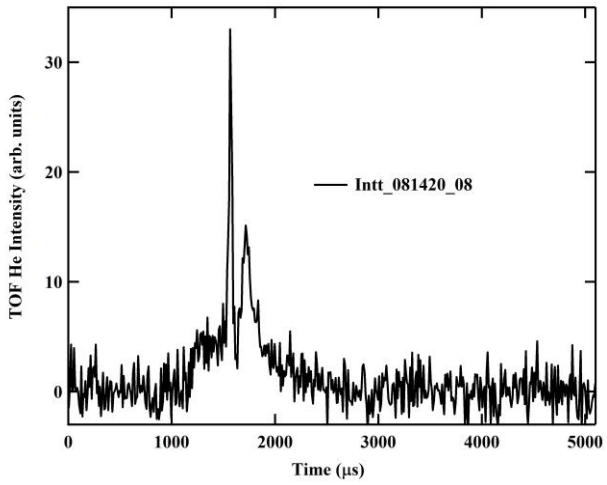

Figure B4.9: Raw He inelastic time-of-flight from the (3 × 1)-O Nb(100) surface along the $\overline{\Gamma M}$ axis; used to create Figure 4.3(a) and contributes one data point to Figures 4.4(b), 4.7, and 4.8(a). Cross-correlation spectrum taken with T_S = 410 K, E_i = 10 meV, θ_i = 21.1°, and θ_f = 29.2°.

Experiment file: Figures B4.7-B4.13.pxp

Raw data file: 081420_07

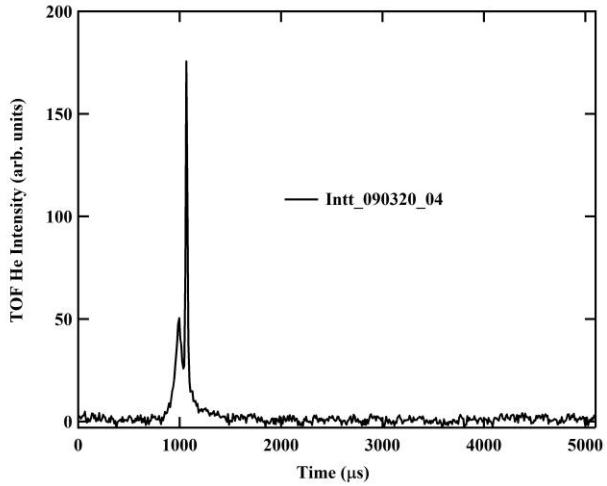

Figure B4.10: Raw He inelastic time-of-flight from the (3 × 1)-O Nb(100) surface along the $\overline{\Gamma M}$ axis; used to create Figure 4.3(b) and contributes one data point to Figures 4.4(b), 4.7, and 4.8(a). Cross-correlation spectrum taken with T_S = 300 K, E_i = 21 meV, θ_i = 27.2°, and θ_f = 19.1°.

Experiment file: Figures B4.7-B4.13.pxp

Raw data file: 090320_04

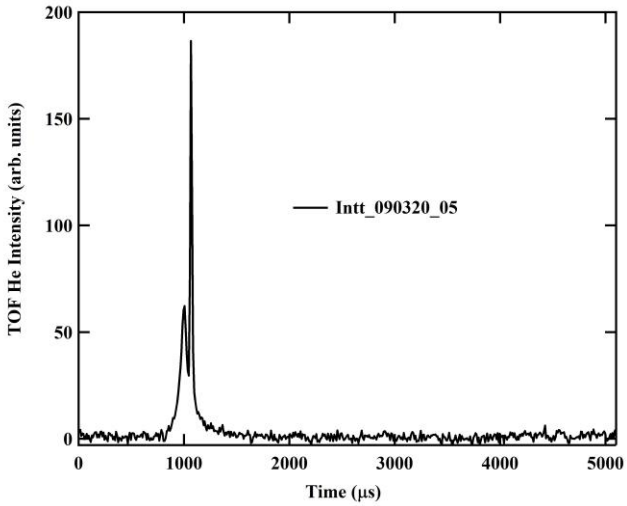

Figure B4.11: Raw He inelastic time-of-flight from the (3 × 1)-O Nb(100) surface along the $\overline{\Gamma M}$ axis; used to create Figure 4.3(b) and contributes one data point to Figures 4.4(b), 4.7, and 4.8(a). Cross-correlation spectrum taken with T_S = 300 K, E_i = 21 meV, θ_i = 27.2°, and θ_f = 20.1°.

Experiment file: Figures B4.7-B4.13.pxp

Raw data file: 090320_05

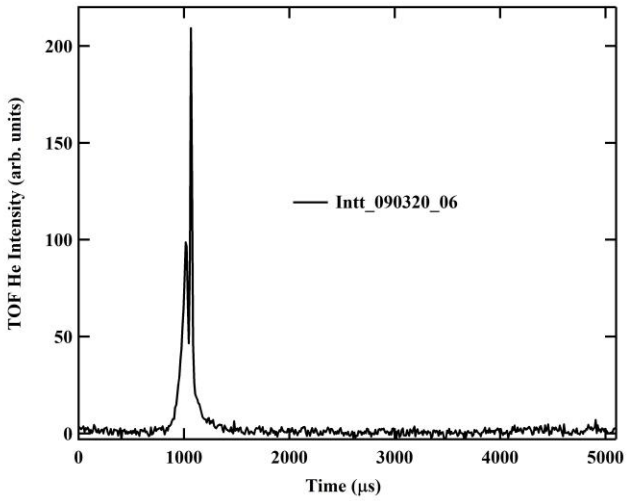

Figure B4.12: Raw He inelastic time-of-flight from the (3 × 1)-O Nb(100) surface along the $\overline{\Gamma M}$ axis; used to create Figure 4.3(b) and contributes one data point to Figures 4.4(b), 4.7, and 4.8(a). Cross-correlation spectrum taken with T_S = 300 K, E_i = 21 meV, θ_i = 27.2°, and θ_f = 22.1°.

Experiment file: Figures B4.7-B4.13.pxp

Raw data file: 090320_06

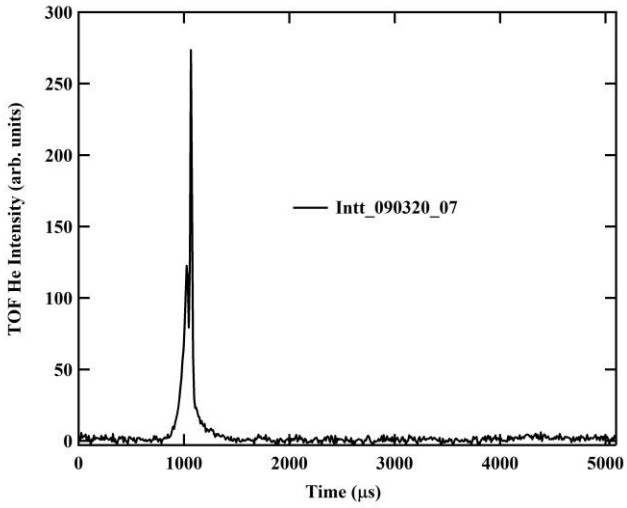

Figure B4.13: Raw He inelastic time-of-flight from the (3 × 1)-O Nb(100) surface along the $\overline{\Gamma M}$ axis; used to create Figure 4.3(b) and contributes one data point to Figures 4.4(b), 4.7, and 4.8(a). Cross-correlation spectrum taken with T_S = 300 K, E_i = 21 meV, θ_i = 27.2°, and θ_f = 23.1°.

Experiment file: Figures B4.7-B4.13.pxp

Raw data file: 090320_07

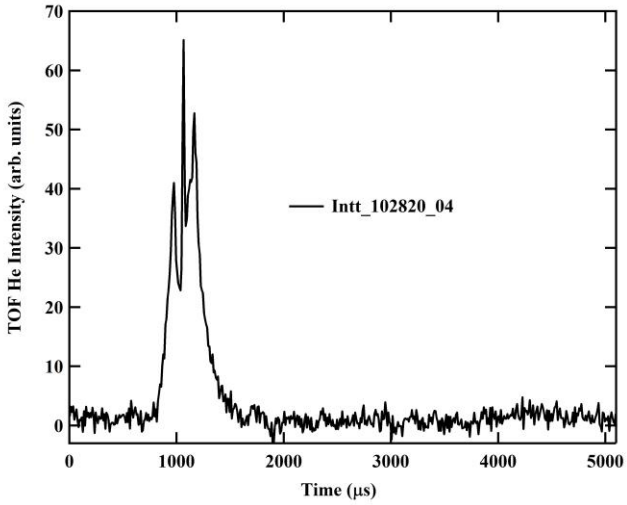

Figure B4.14: Raw He inelastic time-of-flight from the (3 × 1)-O Nb(100) surface along the $\overline{\Gamma X}$ axis; contributes two data points to Figures 4.4(a), 4.7, and 4.8(a). Cross-correlation spectrum taken with T_S = 670 K, E_i = 21 meV, θ_i = 27.4°, and θ_f = 36.9°.

Experiment file: Figures B4.14-B4.34.pxp

Raw data file: 102820_04

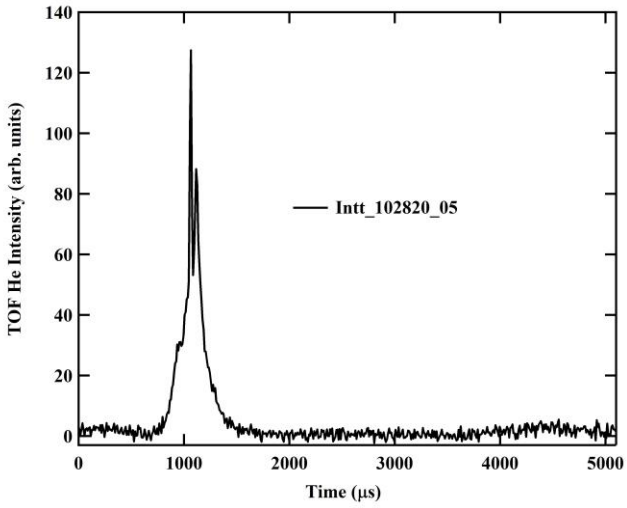

Figure B4.15: Raw He inelastic time-of-flight from the (3 × 1)-O Nb(100) surface along the $\overline{\Gamma X}$ axis; contributes one data point to Figures 4.4(a), 4.7, and 4.8(a). Cross-correlation spectrum taken with T_S = 670 K, E_i = 21 meV, θ_i = 27.4°, and θ_f = 31.9°.

Experiment file: Figures B4.14-B4.34.pxp

Raw data file: 102820_05

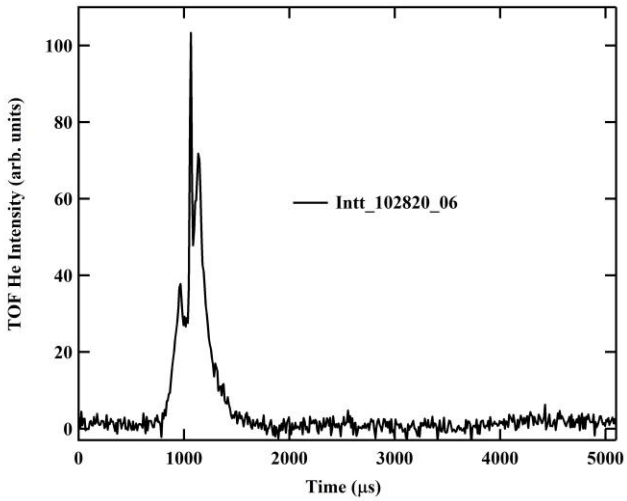

Figure B4.16: Raw He inelastic time-of-flight from the (3 × 1)-O Nb(100) surface along the $\overline{\Gamma X}$ axis; contributes two data points to Figures 4.4(a), 4.7, and 4.8(a). Cross-correlation spectrum taken with T_S = 670 K, E_i = 21 meV, θ_i = 27.4°, and θ_f = 33.9°.

Experiment file: Figures B4.14-B4.34.pxp

Raw data file: 102820_06

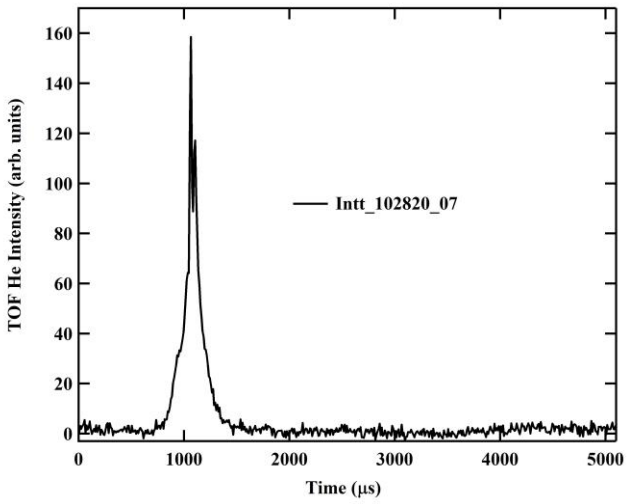

Figure B4.17: Raw He inelastic time-of-flight from the (3 × 1)-O Nb(100) surface along the $\overline{\Gamma X}$ axis; contributes one data point to Figures 4.4(a), 4.7, and 4.8(a). Cross-correlation spectrum taken with T_S = 670 K, E_i = 21 meV, θ_i = 27.4°, and θ_f = 29.9°.

Experiment file: Figures B4.14-B4.34.pxp

Raw data file: 102820_07

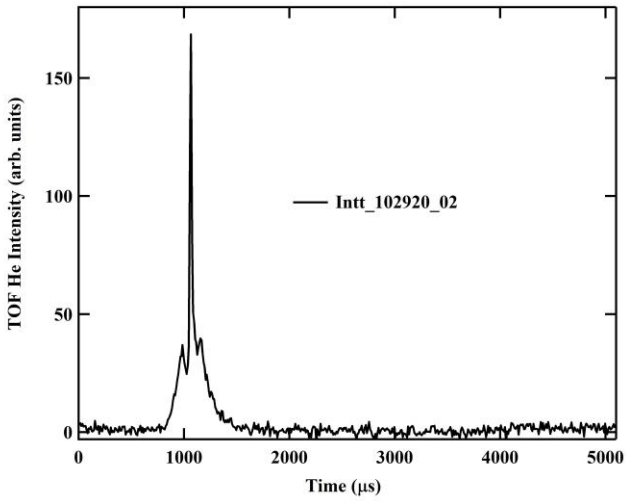

Figure B4.18: Raw He inelastic time-of-flight from the (3 × 1)-O Nb(100) surface along the $\overline{\Gamma X}$ axis; contributes one data point to Figures 4.4(a), 4.7, and 4.8(a). Cross-correlation spectrum taken with T_S = 670 K, E_i = 21 meV, θ_i = 27.2°, and θ_f = 37.1°.

Experiment file: Figures B4.14-B4.34.pxp

Raw data file: 102920_02

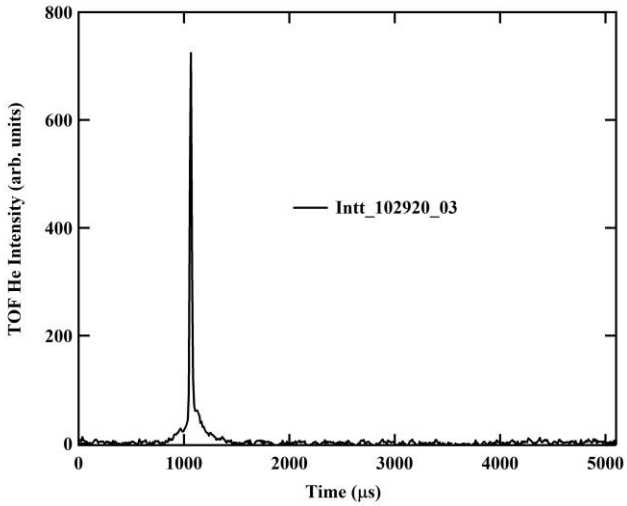

Figure B4.19: Raw He inelastic time-of-flight from the (3 × 1)-O Nb(100) surface along the $\overline{\Gamma X}$ axis; contributes one data point to Figures 4.4(a), 4.7, and 4.8(a). Cross-correlation spectrum taken with T_S = 670 K, E_i = 21 meV, θ_i = 27.2°, and θ_f = 34.1°.

Experiment file: Figures B4.14-B4.34.pxp

Raw data file: 102920_03

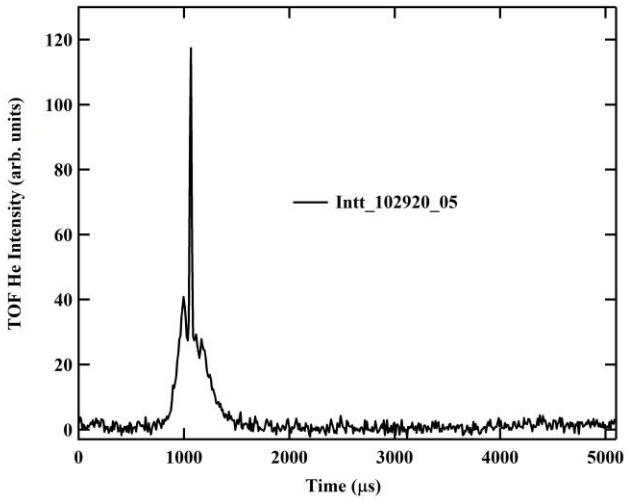

Figure B4.20: Raw He inelastic time-of-flight from the (3 × 1)-O Nb(100) surface along the $\overline{\Gamma X}$ axis; contributes two data points to Figures 4.4(a), 4.7, and 4.8(a). Cross-correlation spectrum taken with T_S = 670 K, E_i = 21 meV, θ_i = 27.2°, and θ_f = 39.1°.

Experiment file: Figures B4.14-B4.34.pxp

Raw data file: 102920_05

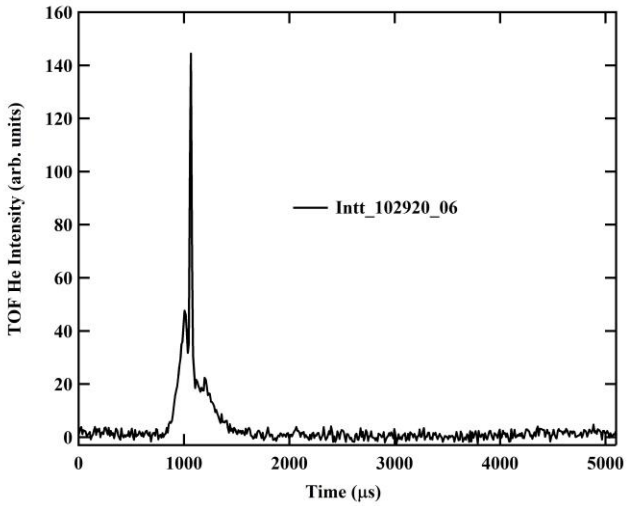

Figure B4.21: Raw He inelastic time-of-flight from the (3 × 1)-O Nb(100) surface along the $\overline{\Gamma X}$ axis; contributes two data points to Figures 4.4(a), 4.7, and 4.8(a). Cross-correlation spectrum taken with T_S = 670 K, E_i = 21 meV, θ_i = 27.2°, and θ_f = 41.1°.

Experiment file: Figures B4.14-B4.34.pxp

Raw data file: 102920_06

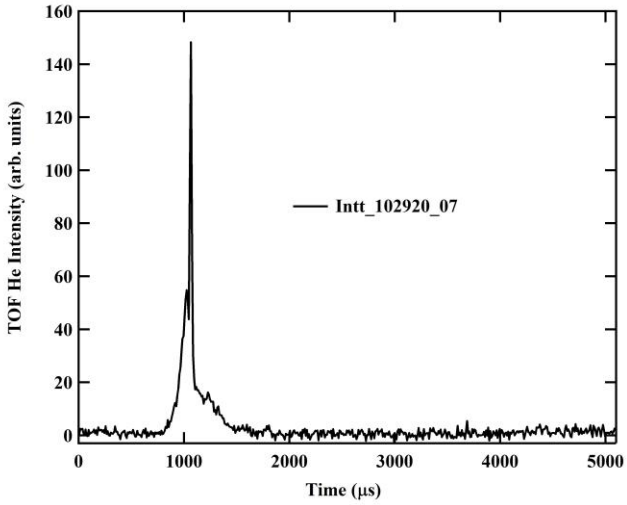

Figure B4.22: Raw He inelastic time-of-flight from the (3 × 1)-O Nb(100) surface along the $\overline{\Gamma X}$ axis; contributes two data points to Figures 4.4(a), 4.7, and 4.8(a). Cross-correlation spectrum taken with T_S = 670 K, E_i = 21 meV, θ_i = 27.2°, and θ_f = 43.1°.

Experiment file: Figures B4.14-B4.34.pxp

Raw data file: 102920_07

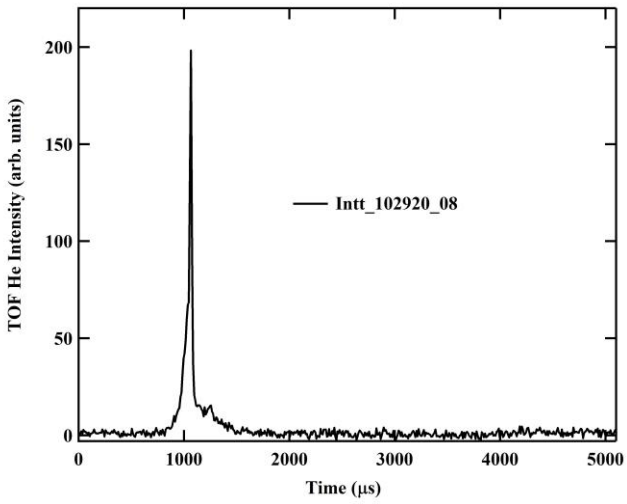

Figure B4.23: Raw He inelastic time-of-flight from the (3 × 1)-O Nb(100) surface along the $\overline{\Gamma X}$ axis; contributes one data point to Figures 4.4(a), 4.7, and 4.8(a). Cross-correlation spectrum taken with T_S = 670 K, E_i = 21 meV, θ_i = 27.2°, and θ_f = 45.1°.

Experiment file: Figures B4.14-B4.34.pxp

Raw data file: 102920_08

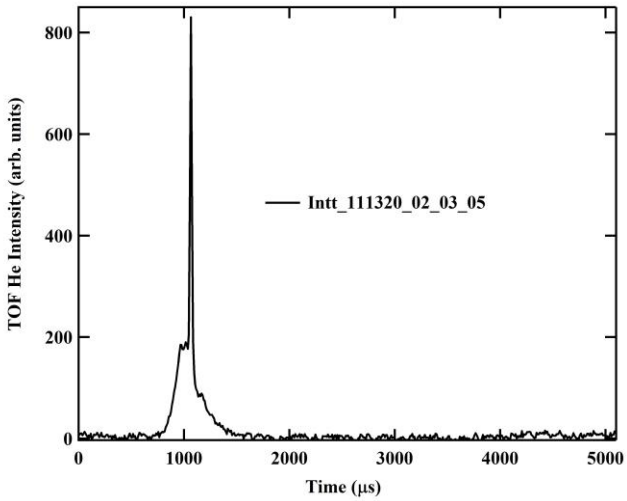

Figure B4.24: Raw He inelastic time-of-flight from the (3 × 1)-O Nb(100) surface along the $\overline{\Gamma X}$ axis; contributes three data points to Figures 4.4(a), 4.7, and 4.8(a). Three cross-correlation spectra taken with T_S = 670 K, E_i = 21 meV, θ_i = 34.8°, and θ_f = 22.5° and then added.

Experiment file: Figures B4.14-B4.34.pxp

Raw data files: 111320_02, 111320_03, and 111320_05

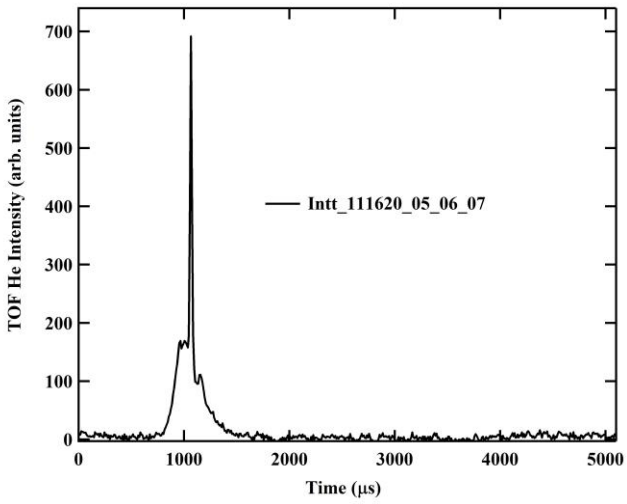

Figure B4.25: Raw He inelastic time-of-flight from the (3 × 1)-O Nb(100) surface along the $\overline{\Gamma X}$ axis; contributes three data points to Figures 4.4(a), 4.7, and 4.8(a). Three cross-correlation spectra taken with T_S = 670 K, E_i = 21 meV, θ_i = 34.7°, and θ_f = 21.7° and then added.

Experiment file: Figures B4.14-B4.34.pxp

Raw data files: 111620_05, 111620_06, and 111620_07

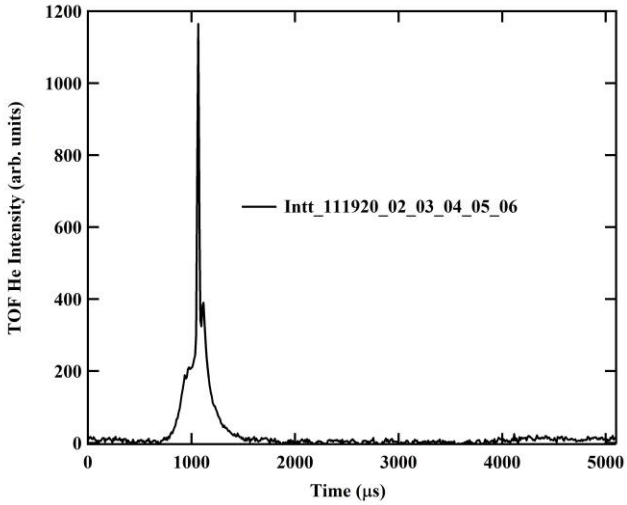

Figure B4.26: Raw He inelastic time-of-flight from the (3 × 1)-O Nb(100) surface along the $\overline{\Gamma X}$ axis; contributes three data points to Figures 4.4(a), 4.7, and 4.8(a). Five cross-correlation spectra taken with T_S = 670 K, E_i = 21 meV, θ_i = 34.7°, and θ_f = 18.6° and then added.

Experiment file: Figures B4.14-B4.34.pxp

Raw data files: 111920_02, 111920_03, 111920_04, 111920_05, and 111920_06

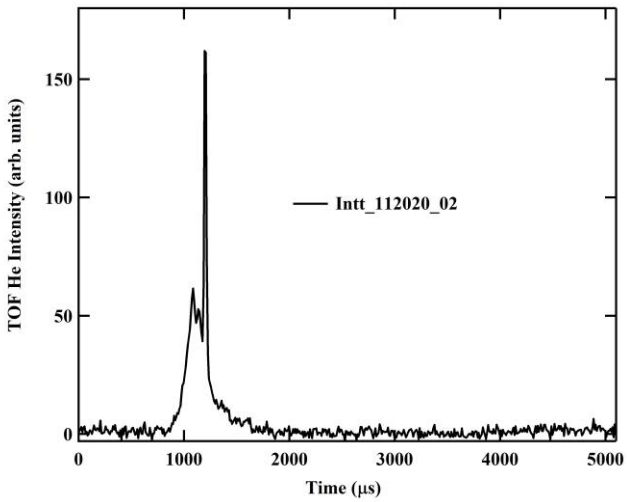

Figure B4.27: Raw He inelastic time-of-flight from the (3 × 1)-O Nb(100) surface along the $\overline{\Gamma X}$ axis; contributes two data points to Figures 4.4(a), 4.7, and 4.8(a). Cross-correlation spectrum taken with T_S = 670 K, E_i = 16 meV, θ_i = 34.6°, and θ_f = 22.7°.

Experiment file: Figures B4.14-B4.34.pxp

Raw data file: 112020_02

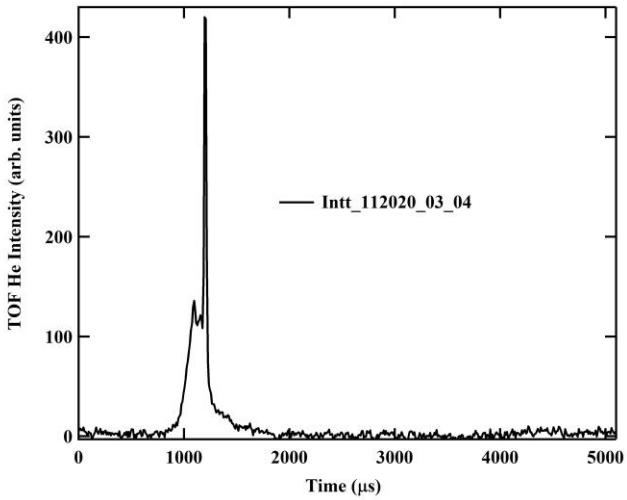

Figure B4.28: Raw He inelastic time-of-flight from the (3 × 1)-O Nb(100) surface along the $\overline{\Gamma X}$ axis; contributes two data points to Figures 4.4(a), 4.7, and 4.8(a). Two cross-correlation spectra taken with T_S = 670 K, E_i = 16 meV, θ_i = 34.7°, and θ_f = 23.7° and then added.

Experiment file: Figures B4.14-B4.34.pxp

Raw data files: 112020_03 and 112020_04

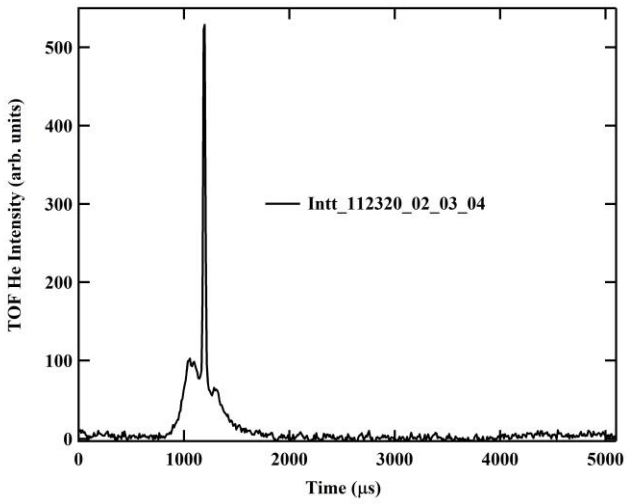

Figure B4.29: Raw He inelastic time-of-flight from the (3 × 1)-O Nb(100) surface along the $\overline{\Gamma X}$ axis; contributes three data points to Figures 4.4(a), 4.7, and 4.8(a). Three cross-correlation spectra taken with T_S = 670 K, E_i = 17 meV, θ_i = 34.6°, and θ_f = 19.7° and then added.

Experiment file: Figures B4.14-B4.34.pxp

Raw data files: 112320_02, 112320_03, and 112320_04

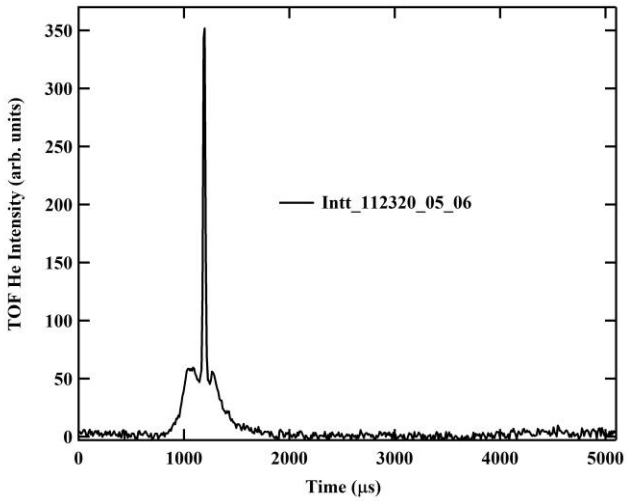

Figure B4.30: Raw He inelastic time-of-flight from the (3 × 1)-O Nb(100) surface along the $\overline{\Gamma X}$ axis; contributes one data point to Figures 4.4(a), 4.7, and 4.8(a). Two cross-correlation spectra taken with T_S = 670 K, E_i = 17 meV, θ_i = 34.6°, and θ_f = 18.7° and then added.

Experiment file: Figures B4.14-B4.34.pxp

Raw data files: 112320_05 and 112320_06

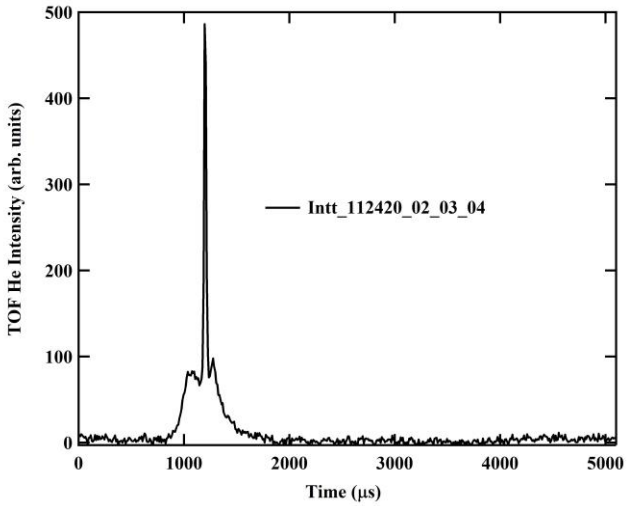

Figure B4.31: Raw He inelastic time-of-flight from the (3 × 1)-O Nb(100) surface along the $\overline{\Gamma X}$ axis; contributes one data point to Figures 4.4(a), 4.7, and 4.8(a). Three cross-correlation spectra taken with T_S = 670 K, E_i = 16 meV, θ_i = 34.6°, and θ_f = 17.7° and then added.

Experiment file: Figures B4.14-B4.34.pxp

Raw data files: 112420_02, 112420_03, and 112420_04

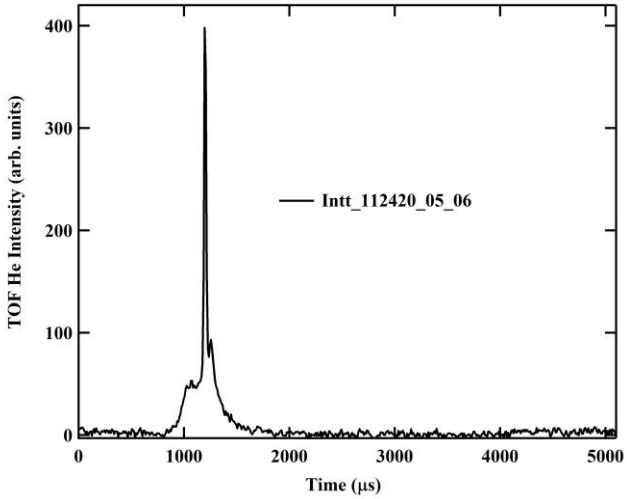

Figure B4.32: Raw He inelastic time-of-flight from the (3 × 1)-O Nb(100) surface along the $\overline{\Gamma X}$ axis; contributes one data point to Figures 4.4(a), 4.7, and 4.8(a). Two cross-correlation spectra taken with T_S = 670 K, E_i = 16 meV, θ_i = 34.6°, and θ_f = 16.7° and then added.

Experiment file: Figures B4.14-B4.34.pxp

Raw data files: 112420_05 and 112420_06

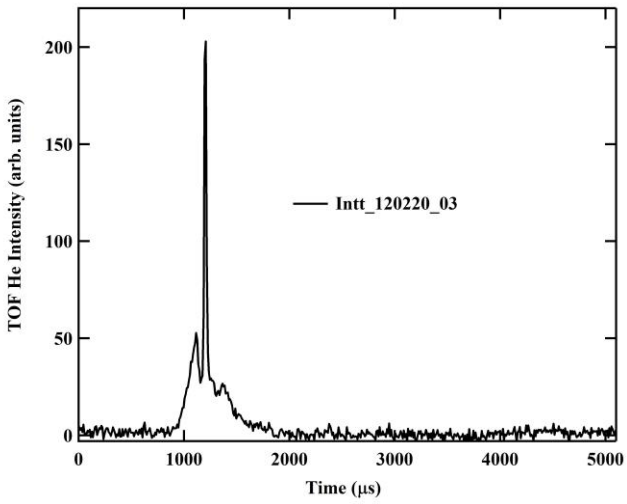

Figure B4.33: Raw He inelastic time-of-flight from the (3 × 1)-O Nb(100) surface along the $\overline{\Gamma X}$ axis; contributes one data point to Figures 4.4(a), 4.7, and 4.8(a). Cross-correlation spectrum taken with T_S = 670 K, E_i = 16 meV, θ_i = 20.6°, and θ_f = 33.7°.

Experiment file: Figures B4.14-B4.34.pxp

Raw data file: 120220_03

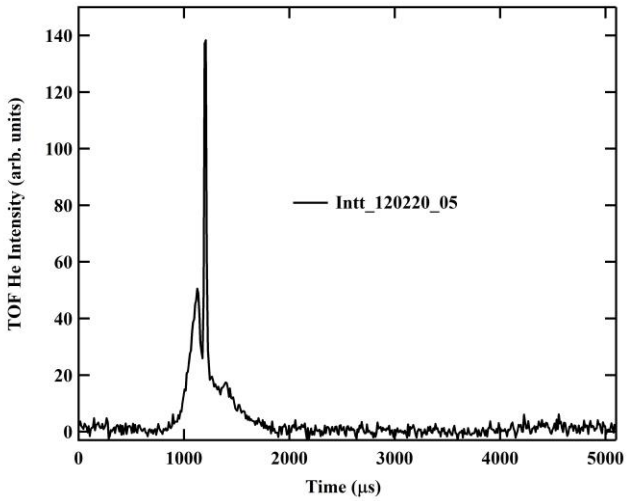

Figure B4.34: Raw He inelastic time-of-flight from the (3 × 1)-O Nb(100) surface along the $\overline{\Gamma X}$ axis; contributes one data point to Figures 4.4(a), 4.7, and 4.8(a). Cross-correlation spectrum taken with T_S = 670 K, E_i = 16 meV, θ_i = 20.6°, and θ_f = 35.7°.

Experiment file: Figures B4.14-B4.34.pxp

Raw data file: 120220_05

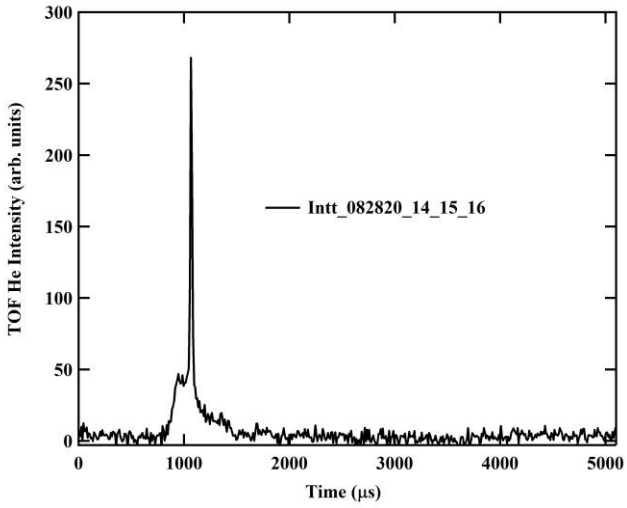

Figure B4.35: Raw He inelastic time-of-flight from the (3 × 1)-O Nb(100) surface along the $\overline{\Gamma M}$ axis; contributes one data point to Figures 4.4(b), 4.7, and 4.8(a). Three cross-correlation spectra taken with T_S = 300 K, E_i = 21 meV, θ_i = 27.2°, and θ_f = 13.1° and then added.

Experiment file: Figures B4.35-B4.66.pxp

Raw data files: 082820_14, 082820_15, and 082820_16

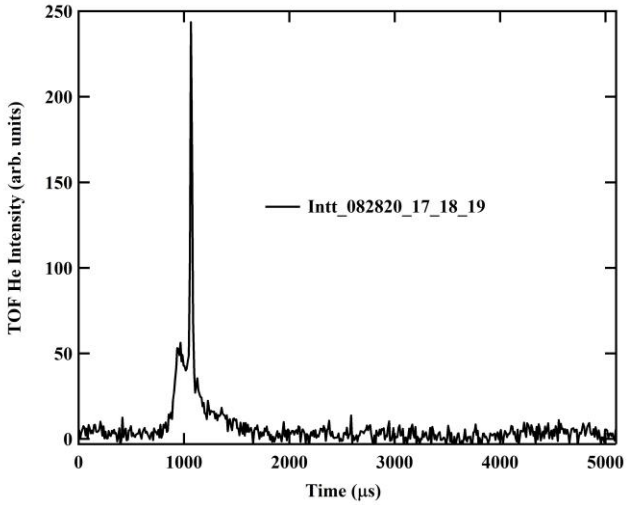

Figure B4.36: Raw He inelastic time-of-flight from the (3 × 1)-O Nb(100) surface along the $\overline{\Gamma M}$ axis; contributes one data point to Figures 4.4(b), 4.7, and 4.8(a). Three cross-correlation spectra taken with T_S = 300 K, E_i = 21 meV, θ_i = 27.2°, and θ_f = 13.1° and then added.

Experiment file: Figures B4.35-B4.66.pxp

Raw data files: 082820_17, 082820_18, and 082820_19

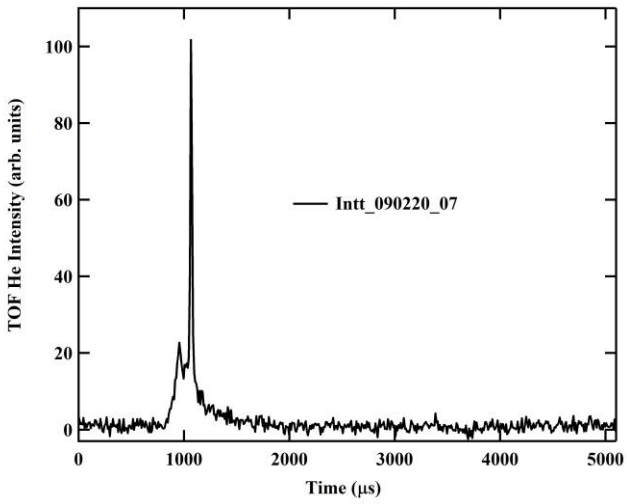

Figure B4.37: Raw He inelastic time-of-flight from the (3 × 1)-O Nb(100) surface along the $\overline{\Gamma M}$ axis; contributes one data point to Figures 4.4(b), 4.7, and 4.8(a). Cross-correlation spectrum taken with T_S = 300 K, E_i = 21 meV, θ_i = 27.2°, and θ_f = 15.1°.

Experiment file: Figures B4.35-B4.66.pxp

Raw data file: 090220_07

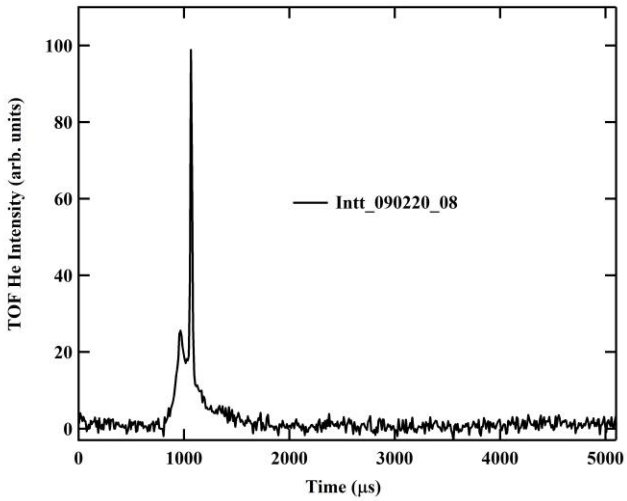

Figure B4.38: Raw He inelastic time-of-flight from the (3 × 1)-O Nb(100) surface along the $\overline{\Gamma M}$ axis; contributes one data point to Figures 4.4(b), 4.7, and 4.8(a). Cross-correlation spectrum taken with T_S = 300 K, E_i = 21 meV, θ_i = 27.2°, and θ_f = 16.1°.

Experiment file: Figures B4.35-B4.66.pxp

Raw data file: 090220_08

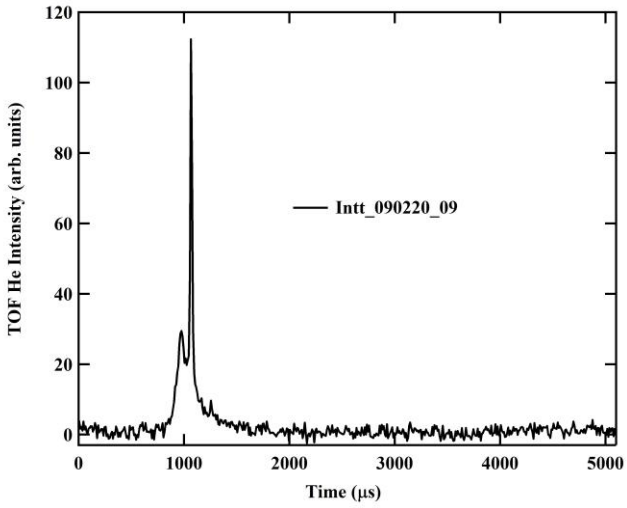

Figure B4.39: Raw He inelastic time-of-flight from the (3 × 1)-O Nb(100) surface along the $\overline{\Gamma M}$ axis; contributes one data point to Figures 4.4(b), 4.7, and 4.8(a). Cross-correlation spectrum taken with T_S = 300 K, E_i = 21 meV, θ_i = 27.2°, and θ_f = 17.1°.

Experiment file: Figures B4.35-B4.66.pxp

Raw data file: 090220_09

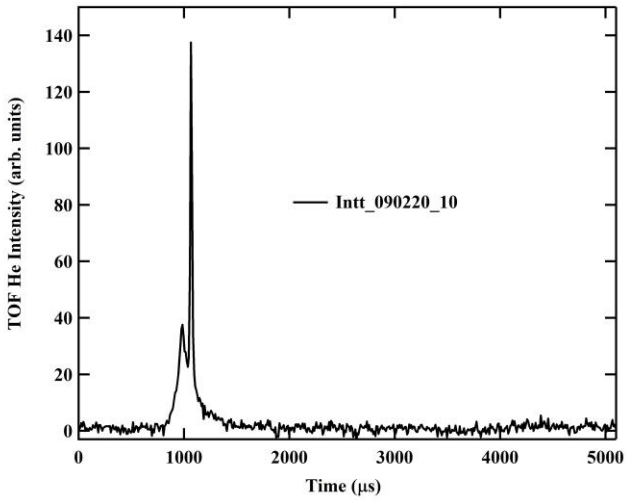

Figure B4.40: Raw He inelastic time-of-flight from the (3 × 1)-O Nb(100) surface along the $\overline{\Gamma M}$ axis; contributes one data point to Figures 4.4(b), 4.7, and 4.8(a). Cross-correlation spectrum taken with T_S = 300 K, E_i = 21 meV, θ_i = 27.2°, and θ_f = 18.1°.

Experiment file: Figures B4.35-B4.66.pxp

Raw data file: 090220_10

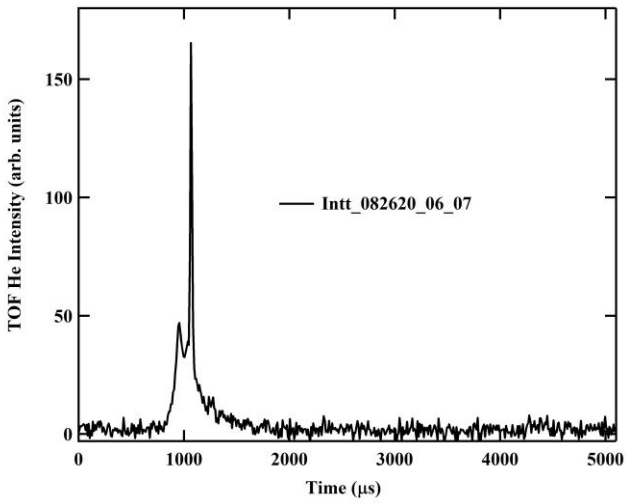

Figure B4.41: Raw He inelastic time-of-flight from the (3 × 1)-O Nb(100) surface along the $\overline{\Gamma M}$ axis; contributes one data point to Figures 4.4(b), 4.7, and 4.8(a). Two cross-correlation spectra taken with T_S = 300 K, E_i = 21 meV, θ_i = 27.1°, and θ_f = 15.2° and then added.

Experiment file: Figures B4.35-B4.66.pxp

Raw data files: 082620_06 and 082620_07

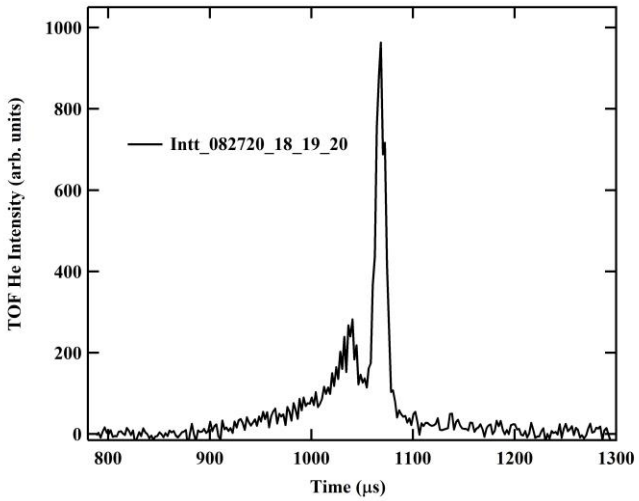

Figure B4.42: Raw He inelastic time-of-flight from the (3 × 1)-O Nb(100) surface along the $\overline{\Gamma M}$ axis; contributes one data point to Figures 4.4(b), 4.7, and 4.8(a). Three single-shot spectra taken with T_S = 300 K, E_i = 21 meV, θ_i = 27.2°, and θ_f = 24.1° and then added.

Experiment file: Figures B4.35-B4.66.pxp

Raw data files: 082720_18, 082720_19, and 082720_20

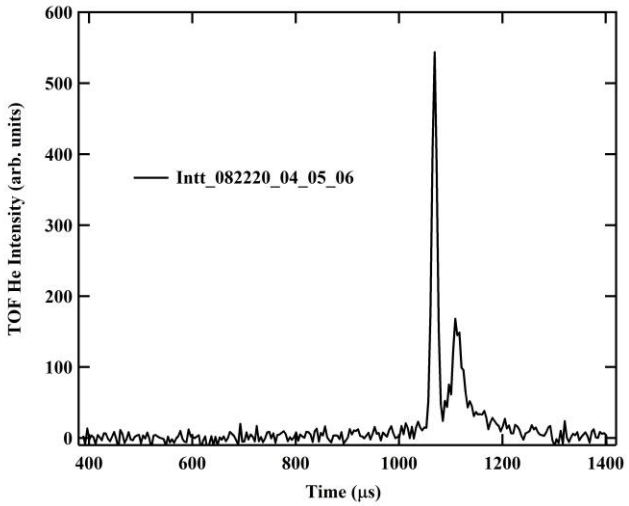

Figure B4.43: Raw He inelastic time-of-flight from the (3 × 1)-O Nb(100) surface along the $\overline{\Gamma M}$ axis; contributes one data point to Figures 4.4(b), 4.7, and 4.8(a). Three single-shot spectra taken with T_S = 300 K, E_i = 21 meV, θ_i = 27.1°, and θ_f = 32.2° and then added.

Experiment file: Figures B4.35-B4.66.pxp

Raw data files: 082220_04, 082220_05, and 082220_06

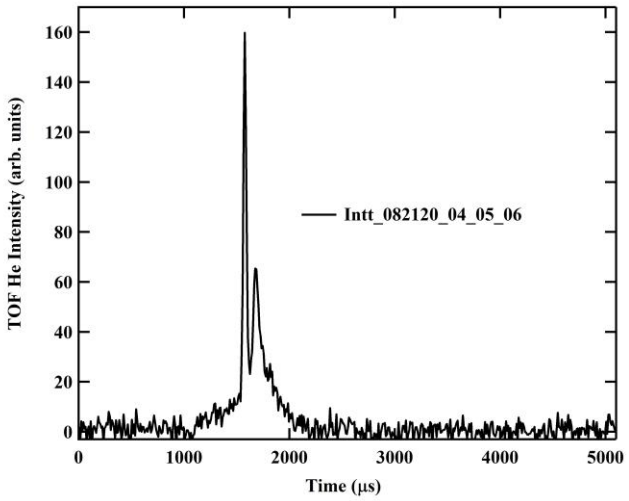

Figure B4.44: Raw He inelastic time-of-flight from the (3 × 1)-O Nb(100) surface along the $\overline{\Gamma M}$ axis; contributes one data point to Figures 4.4(b), 4.7, and 4.8(a). Three cross-correlation spectra taken with T_S = 300 K, E_i = 10 meV, θ_i = 27.3°, and θ_f = 34.0° and then added.

Experiment file: Figures B4.35-B4.66.pxp

Raw data files: 082120_04, 082120_05, and 082120_06

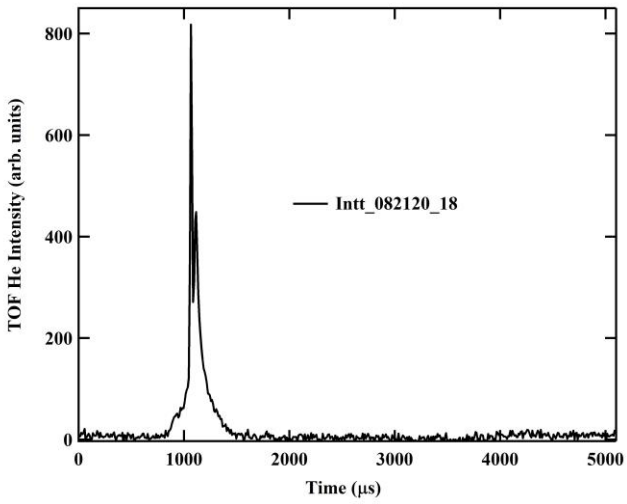

Figure B4.45: Raw He inelastic time-of-flight from the (3 × 1)-O Nb(100) surface along the $\overline{\Gamma M}$ axis; contributes one data point to Figures 4.4(b), 4.7, and 4.8(a). Cross-correlation spectrum taken with T_S = 300 K, E_i = 21 meV, θ_i = 27.1°, and θ_f = 32.2°.

Experiment file: Figures B4.35-B4.66.pxp

Raw data file: 082120_18

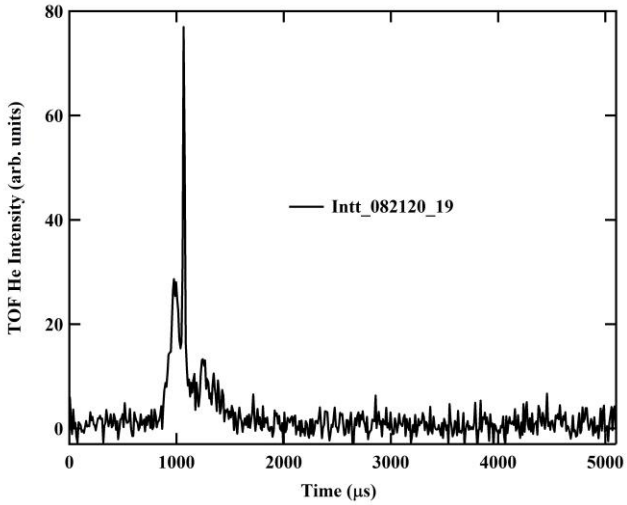

Figure B4.46: Raw He inelastic time-of-flight from the (3 × 1)-O Nb(100) surface along the $\overline{\Gamma M}$ axis; contributes two data points to Figures 4.4(b), 4.7, and 4.8(a). Cross-correlation spectrum taken with T_S = 300 K, E_i = 21 meV, θ_i = 27.1°, and θ_f = 47.2°.

Experiment file: Figures B4.35-B4.66.pxp

Raw data file: 082120_19

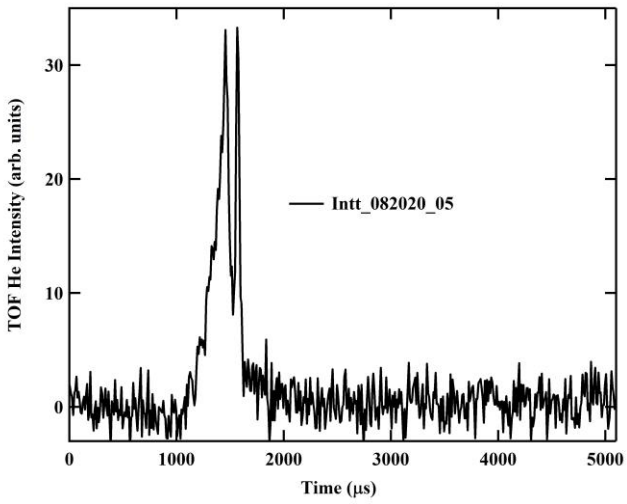

Figure B4.47: Raw He inelastic time-of-flight from the (3 × 1)-O Nb(100) surface along the $\overline{\Gamma M}$ axis; contributes one data point to Figures 4.4(b), 4.7, and 4.8(a). Cross-correlation spectrum taken with T_S = 410 K, E_i = 10 meV, θ_i = 27.2°, and θ_f = 20.4°.

Experiment file: Figures B4.35-B4.66.pxp

Raw data file: 082020_05

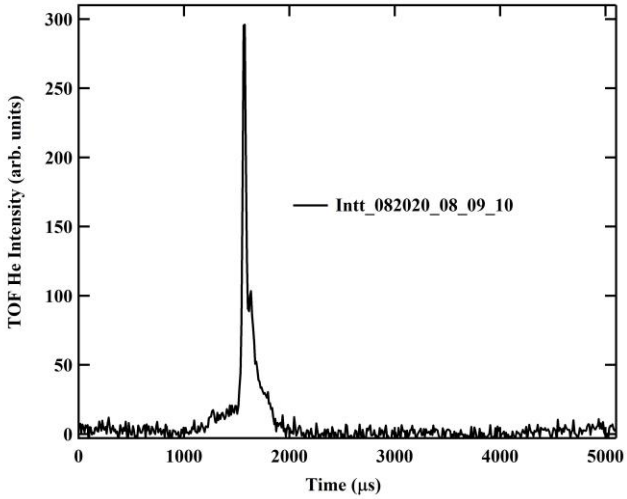

Figure B4.48: Raw He inelastic time-of-flight from the (3 × 1)-O Nb(100) surface along the $\overline{\Gamma M}$ axis; contributes one data point to Figures 4.4(b), 4.7, and 4.8(a). Three cross-correlation spectra taken with T_S = 410 K, E_i = 10 meV, θ_i = 27.2°, and θ_f = 31.1° and then added.

Experiment file: Figures B4.35-B4.66.pxp

Raw data files: 082020_08, 082020_09, and 082020_10

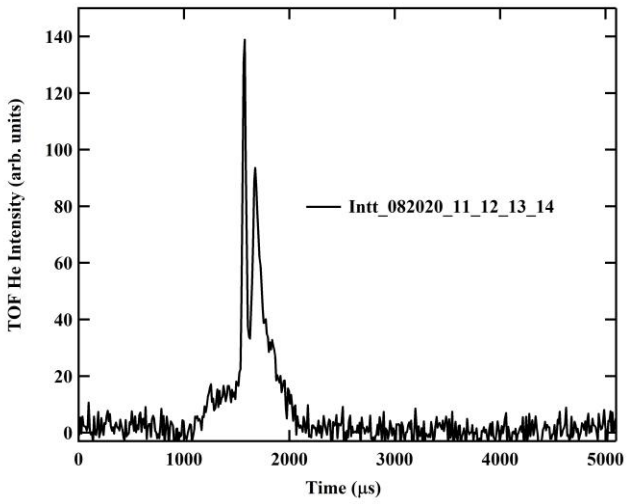

Figure B4.49: Raw He inelastic time-of-flight from the (3 × 1)-O Nb(100) surface along the $\overline{\Gamma M}$ axis; contributes one data point to Figures 4.4(b), 4.7, and 4.8(a). Four cross-correlation spectra taken with T_S = 410 K, E_i = 10 meV, θ_i = 27.2°, and θ_f = 34.1° and then added.

Experiment file: Figures B4.35-B4.66.pxp

Raw data files: 082020_11, 082020_12, 082020_13, and 082020_14

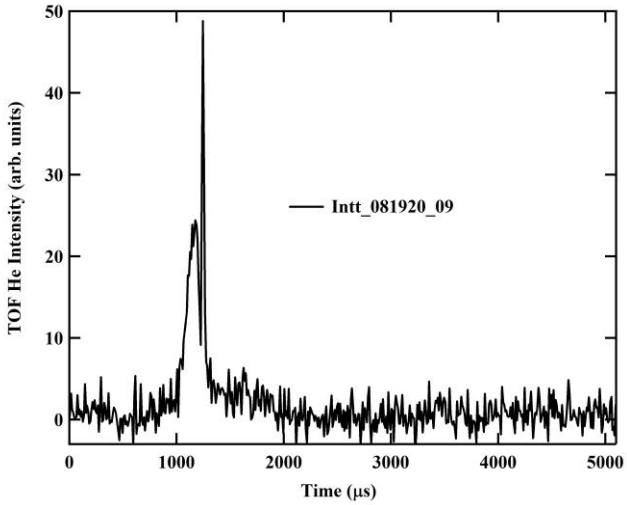

Figure B4.50: Raw He inelastic time-of-flight from the (3 × 1)-O Nb(100) surface along the $\overline{\Gamma M}$ axis; contributes one data point to Figures 4.4(b), 4.7, and 4.8(a). Cross-correlation spectrum taken with T_S = 410 K, E_i = 15 meV, θ_i = 20.7°, and θ_f = 48.6°.

Experiment file: Figures B4.35-B4.66.pxp

Raw data file: 081920_09

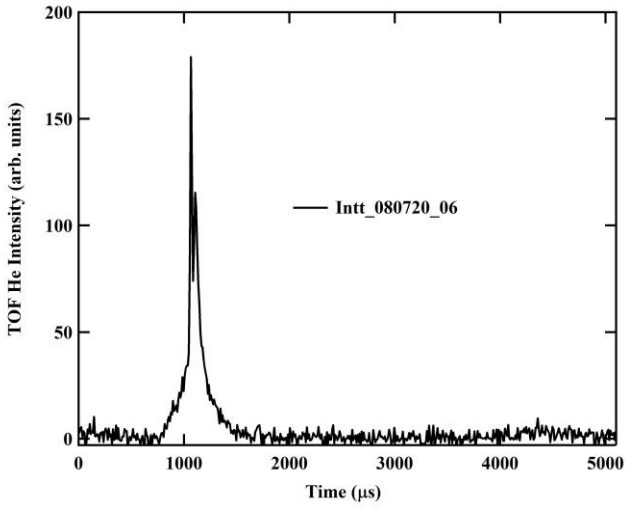

Figure B4.51: Raw He inelastic time-of-flight from the (3 × 1)-O Nb(100) surface along the $\overline{\Gamma M}$ axis; contributes one data point to Figures 4.4(b), 4.7, and 4.8(a). Cross-correlation spectrum taken with T_S = 410 K, E_i = 21 meV, θ_i = 20.7°, and θ_f = 24.6°.

Experiment file: Figures B4.35-B4.66.pxp

Raw data file: 080720_06

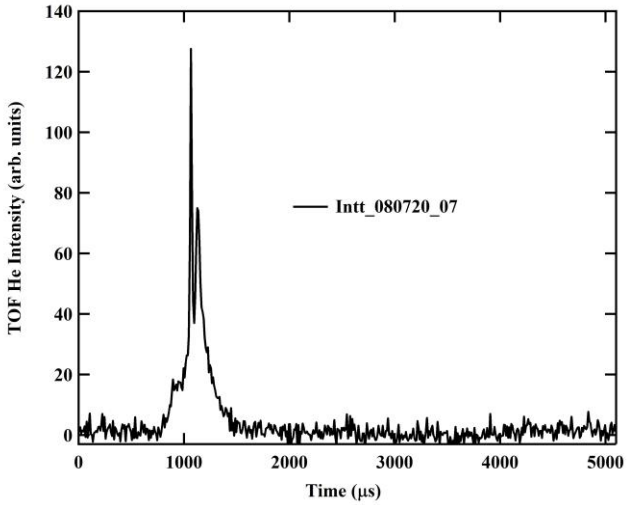

Figure B4.52: Raw He inelastic time-of-flight from the (3 × 1)-O Nb(100) surface along the $\overline{\Gamma M}$ axis; contributes one data point to Figures 4.4(b), 4.7, and 4.8(a). Cross-correlation spectrum taken with T_S = 410 K, E_i = 21 meV, θ_i = 20.7°, and θ_f = 26.6°.

Experiment file: Figures B4.35-B4.66.pxp

Raw data file: 080720_07

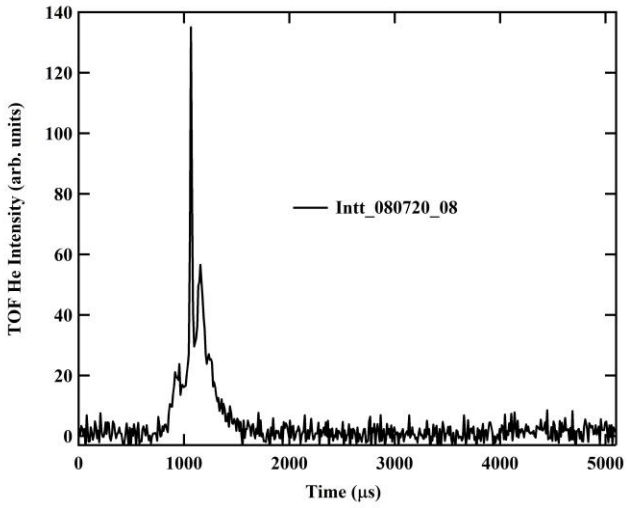

Figure B4.53: Raw He inelastic time-of-flight from the (3 × 1)-O Nb(100) surface along the $\overline{\Gamma M}$ axis; contributes two data points to Figures 4.4(b), 4.7, and 4.8(a). Cross-correlation spectrum taken with T_S = 410 K, E_i = 21 meV, θ_i = 20.7°, and θ_f = 28.6°.

Experiment file: Figures B4.35-B4.66.pxp

Raw data file: 080720_08

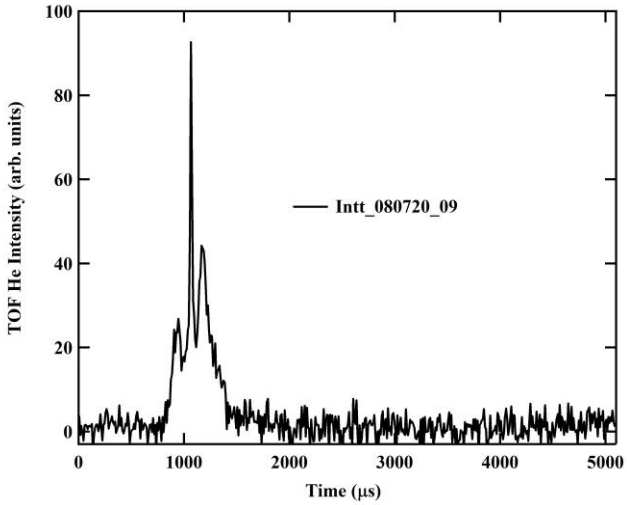

Figure B4.54: Raw He inelastic time-of-flight from the (3 × 1)-O Nb(100) surface along the $\overline{\Gamma M}$ axis; contributes one data point to Figures 4.4(b), 4.7, and 4.8(a). Cross-correlation spectrum taken with T_S = 410 K, E_i = 21 meV, θ_i = 20.7°, and θ_f = 30.6°.

Experiment file: Figures B4.35-B4.66.pxp

Raw data file: 080720_09

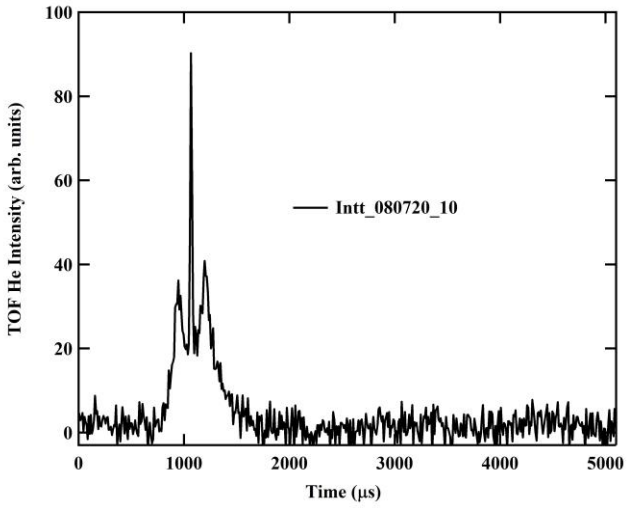

Figure B4.55: Raw He inelastic time-of-flight from the (3 × 1)-O Nb(100) surface along the $\overline{\Gamma M}$ axis; contributes two data points to Figures 4.4(b), 4.7, and 4.8(a). Cross-correlation spectrum taken with T_S = 410 K, E_i = 21 meV, θ_i = 20.7°, and θ_f = 32.6°.

Experiment file: Figures B4.35-B4.66.pxp

Raw data file: 080720_10

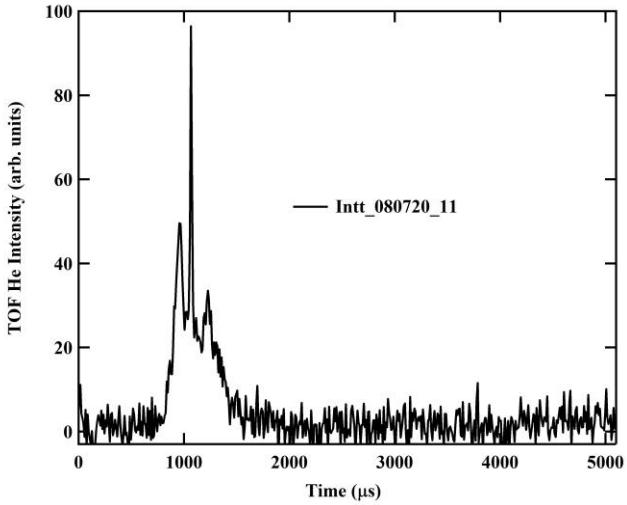

Figure B4.56: Raw He inelastic time-of-flight from the (3 × 1)-O Nb(100) surface along the $\overline{\Gamma M}$ axis; contributes two data points to Figures 4.4(b), 4.7, and 4.8(a). Cross-correlation spectrum taken with T_S = 410 K, E_i = 21 meV, θ_i = 20.7°, and θ_f = 34.6°.

Experiment file: Figures B4.35-B4.66.pxp

Raw data file: 080720_11

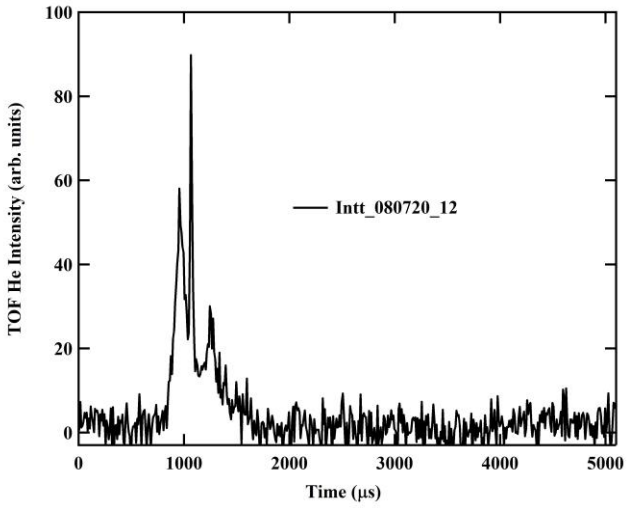

Figure B4.57: Raw He inelastic time-of-flight from the (3 × 1)-O Nb(100) surface along the $\overline{\Gamma M}$ axis; contributes one data point to Figures 4.4(b), 4.7, and 4.8(a). Cross-correlation spectrum taken with T_S = 410 K, E_i = 21 meV, θ_i = 20.7°, and θ_f = 36.6°.

Experiment file: Figures B4.35-B4.66.pxp

Raw data file: 080720_12

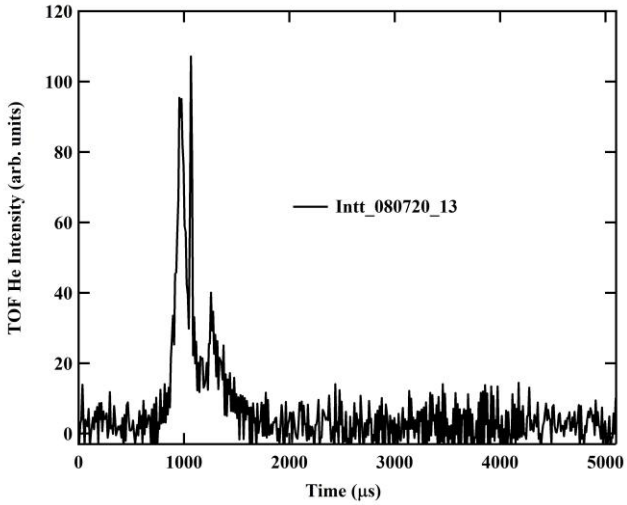

Figure B4.58: Raw He inelastic time-of-flight from the (3 × 1)-O Nb(100) surface along the $\overline{\Gamma M}$ axis; contributes one data point to Figures 4.4(b), 4.7, and 4.8(a). Cross-correlation spectrum taken with T_S = 410 K, E_i = 21 meV, θ_i = 20.7°, and θ_f = 38.6°.

Experiment file: Figures B4.35-B4.66.pxp

Raw data file: 080720_13

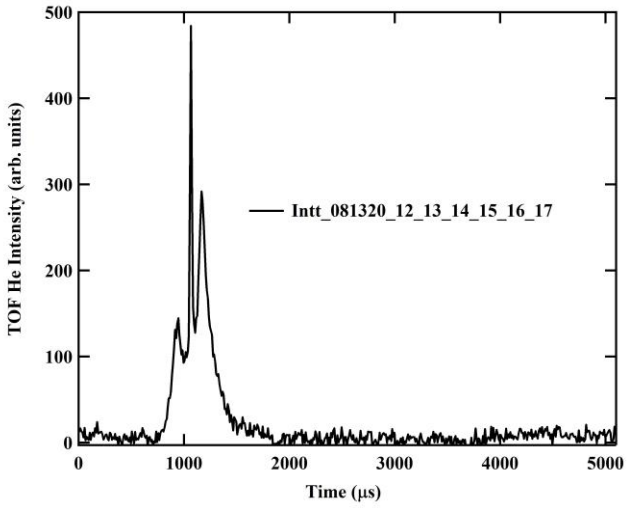

Figure B4.59: Raw He inelastic time-of-flight from the (3 × 1)-O Nb(100) surface along the $\overline{\Gamma M}$ axis; contributes two data points to Figures 4.4(b), 4.7, and 4.8(a). Six cross-correlation spectra taken with T_S = 410 K, E_i = 21 meV, θ_i = 20.7°, and θ_f = 30.6°.

Experiment file: Figures B4.35-B4.66.pxp

Raw data files: 081320_12, 081320_13, 081320_14, 081320_15, 081320_16, and 081320_17

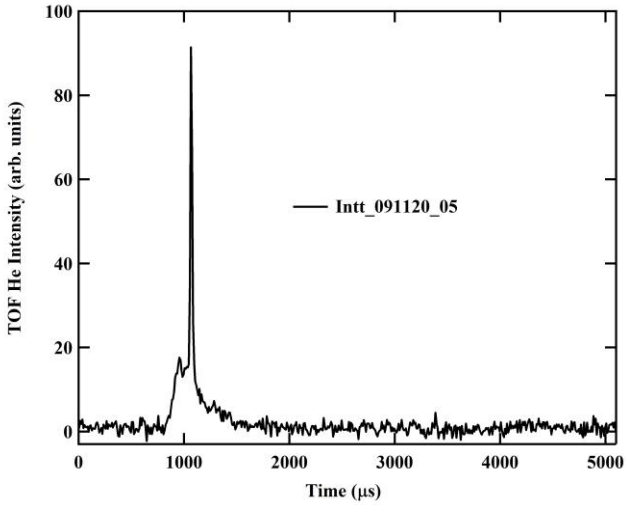

Figure B4.60: Raw He inelastic time-of-flight from the (3 × 1)-O Nb(100) surface along the $\overline{\Gamma M}$ axis; contributes one data point to Figures 4.4(b), 4.7, and 4.8(a). Cross-correlation spectrum taken with T_S = 300 K, E_i = 21 meV, θ_i = 27.2°, and θ_f = 13.6°.

Experiment file: Figures B4.35-B4.66.pxp

Raw data file: 091120_05

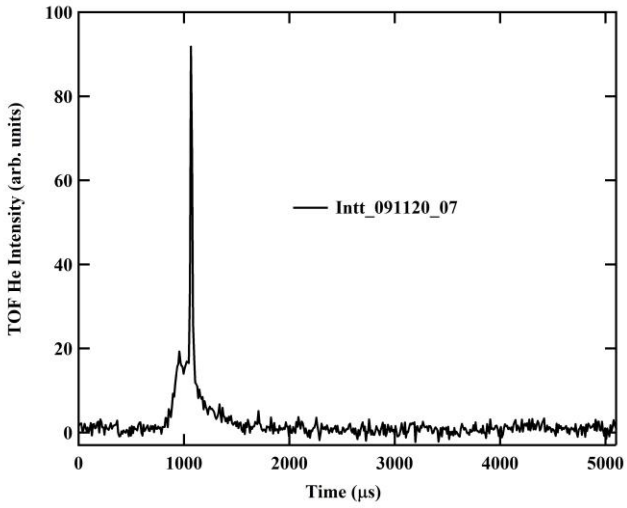

Figure B4.61: Raw He inelastic time-of-flight from the (3 × 1)-O Nb(100) surface along the $\overline{\Gamma M}$ axis; contributes one data point to Figures 4.4(b), 4.7, and 4.8(a). Cross-correlation spectrum taken with T_S = 300 K, E_i = 21 meV, θ_i = 27.2°, and θ_f = 14.1°.

Experiment file: Figures B4.35-B4.66.pxp

Raw data file: 091120_07

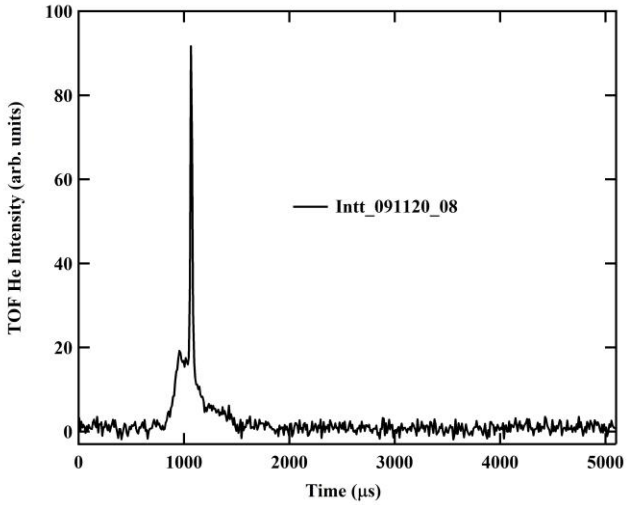

Figure B4.62: Raw He inelastic time-of-flight from the (3 × 1)-O Nb(100) surface along the $\overline{\Gamma M}$ axis; contributes one data point to Figures 4.4(b), 4.7, and 4.8(a). Cross-correlation spectrum taken with T_S = 300 K, E_i = 21 meV, θ_i = 27.2°, and θ_f = 14.6°.

Experiment file: Figures B4.35-B4.66.pxp

Raw data file: 091120_08

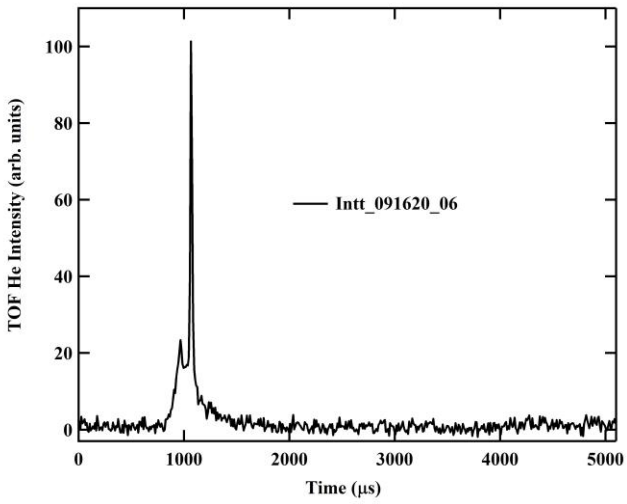

Figure B4.63: Raw He inelastic time-of-flight from the (3 × 1)-O Nb(100) surface along the $\overline{\Gamma M}$ axis; contributes one data point to Figures 4.4(b), 4.7, and 4.8(a). Cross-correlation spectrum taken with T_S = 300 K, E_i = 21 meV, θ_i = 27.1°, and θ_f = 16.2°.

Experiment file: Figures B4.35-B4.66.pxp

Raw data file: 091620_06

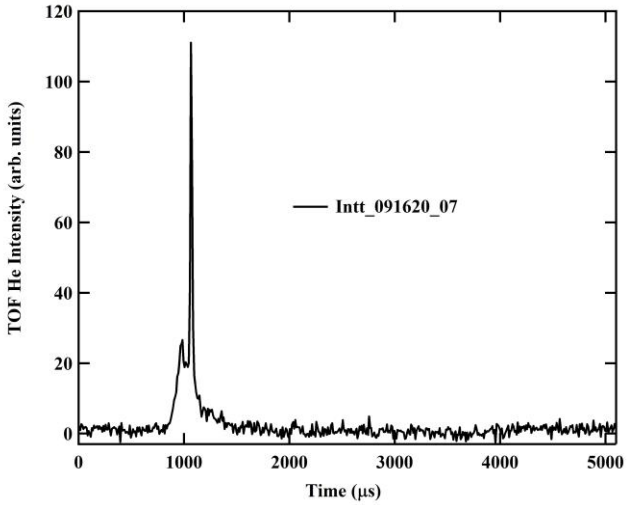

Figure B4.64: Raw He inelastic time-of-flight from the (3 × 1)-O Nb(100) surface along the $\overline{\Gamma M}$ axis; contributes one data point to Figures 4.4(b), 4.7, and 4.8(a). Cross-correlation spectrum taken with T_S = 300 K, E_i = 21 meV, θ_i = 27.1°, and θ_f = 17.2°.

Experiment file: Figures B4.35-B4.66.pxp

Raw data file: 091620_07

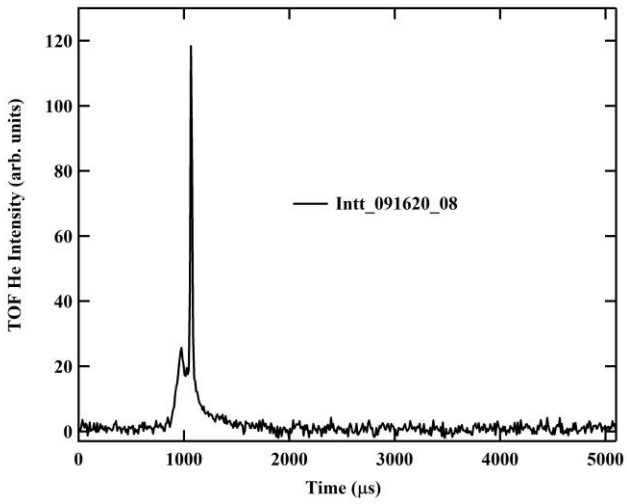

Figure B4.65: Raw He inelastic time-of-flight from the (3 × 1)-O Nb(100) surface along the $\overline{\Gamma M}$ axis; contributes one data point to Figures 4.4(b), 4.7, and 4.8(a). Cross-correlation spectrum taken with T_S = 300 K, E_i = 21 meV, θ_i = 27.1°, and θ_f = 16.7°.

Experiment file: Figures B4.35-B4.66.pxp

Raw data file: 091620_08

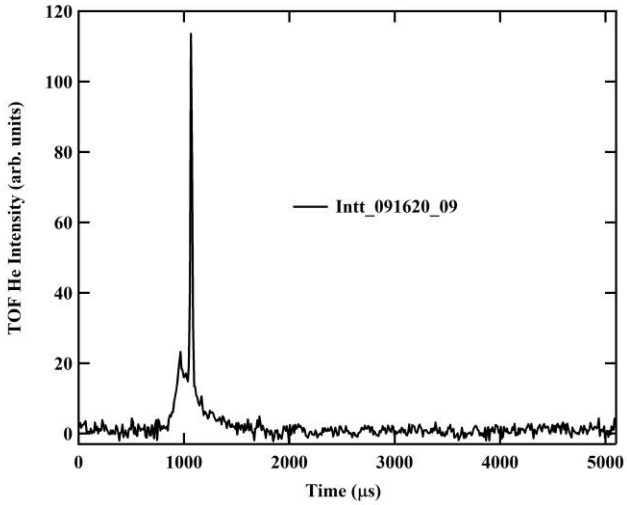

Figure B4.66: Raw He inelastic time-of-flight from the (3 × 1)-O Nb(100) surface along the $\overline{\Gamma M}$ axis; contributes one data point to Figures 4.4(b), 4.7, and 4.8(a). Cross-correlation spectrum taken with T_S = 300 K, E_i = 21 meV, θ_i = 27.1°, and θ_f = 15.7°.

Experiment file: Figures B4.35-B4.66.pxp

Raw data file: 091620_09

Filename	E_i (meV)	k_i (Å^{-1})	θ_i (°)	θ_f (°)	t_0 (μs)	t_{obs} (μs)	k_f (Å^{-1})	ΔK (Å^{-1})	ΔE (meV)
102820_07	21	6.3	27.4	29.9	1063	1104	5.9	0.0	-2.7
102820_05	21	6.3	27.4	31.9	1064	1120	5.8	0.1	-3.6
102820_06	21	6.3	27.4	33.9	1064	963	7.7	1.4	10.0
102820_06	21	6.3	27.4	33.9	1064	1142	5.6	0.2	-4.8
102920_02	21	6.3	27.2	37.1	1064	1159	5.4	0.4	-5.6
102920_05	21	6.3	27.2	39.1	1064	998	7.2	1.6	5.9
102920_05	21	6.3	27.2	39.1	1064	1108	5.9	0.8	-2.9
102920_05	21	6.3	27.2	39.1	1064	1179	5.3	0.4	-6.5
102820_04	21	6.3	27.4	36.9	1064	972	7.6	1.6	8.9
102820_04	21	6.3	27.4	36.9	1064	1168	5.4	0.3	-6.0
102920_03	21	6.3	27.2	34.1	1064	964	7.7	1.4	9.9
102920_06	21	6.3	27.2	41.1	1064	1009	7.0	1.7	4.7
102920_06	21	6.3	27.2	41.1	1064	1203	5.1	0.4	-7.4
111820_02_03	21	6.3	34.7	23.6	1064	972	7.6	-0.6	8.9
111820_02_03	21	6.3	34.7	23.6	1064	1027	6.8	-0.9	3.1
111820_02_03	21	6.3	34.7	23.6	1064	1195	5.1	-1.5	-7.1
111820_04_05	21	6.3	34.7	24.6	1065	972	7.6	-0.5	8.9
111820_04_05	21	6.3	34.7	24.6	1065	1031	6.7	-0.8	2.7
111820_04_05	21	6.3	34.7	24.6	1065	1195	5.2	-1.5	-7.1
102920_07	21	6.3	27.2	43.1	1065	1025	6.8	1.8	3.3
102920_07	21	6.3	27.2	43.1	1065	1233	4.9	0.4	-8.5
111920_02_03_04_05_06	21	6.3	34.7	18.6	1065	936	8.2	-1.0	14.2
111920_02_03_04_05_06	21	6.3	34.7	18.6	1065	972	7.6	-1.2	9.0
111920_02_03_04_05_06	21	6.3	34.7	18.6	1065	1114	5.8	-1.7	-3.2
102920_08	21	6.3	27.2	45.1	1065	1250	4.8	0.5	-9.0
111320_02_03_05	21	6.3	34.8	22.5	1065	964	7.7	-0.7	10.0
111320_02_03_05	21	6.3	34.8	22.5	1065	1022	6.9	-1.0	3.6
111320_02_03_05	21	6.3	34.8	22.5	1065	1176	5.3	-1.6	-6.3
111620_05_06_07	21	6.3	34.7	21.6	1066	959	7.8	-0.7	10.9
111620_05_06_07	21	6.3	34.7	21.6	1066	1005	7.1	-1.0	5.3
111620_05_06_07	21	6.3	34.7	21.6	1066	1165	5.4	-1.6	-5.7

Table B4.1: Filenames, He scattering conditions, and phonon data for TOF spectra taken along the $\overline{\Gamma X}$ axis.

Filename	E_i (meV)	k_i (Å^{-1})	θ_i (°)	θ_f (°)	t_0 (μs)	t_{obs} (μs)	k_f (Å^{-1})	ΔK (Å^{-1})	ΔE (meV)
112320_05_06	17	5.7	34.6	18.7	1192	1282	5.0	-1.6	-3.9
112320_02_03_04	17	5.7	34.6	19.7	1192	1041	7.4	-0.7	12.0
112320_02_03_04	17	5.7	34.6	19.7	1192	1098	6.6	-1.0	6.3
112320_02_03_04	17	5.7	34.6	19.7	1192	1309	4.8	-1.6	-4.8
112420_05_06	16	5.6	34.6	16.7	1200	1254	5.2	-1.7	-2.4
112420_02_03_04	16	5.6	34.6	17.7	1201	1275	5.0	-1.7	-3.3
120120_03	16	5.6	27.2	38.1	1201	1106	6.6	1.5	6.2
120120_03	16	5.6	27.2	38.1	1201	1336	4.6	0.3	-5.2
112020_03_04	16	5.6	34.6	23.7	1202	1091	6.8	-0.5	7.6
112020_03_04	16	5.6	34.6	23.7	1202	1162	6.0	-0.8	2.3
120220_03	16	5.6	20.6	33.7	1202	1116	6.5	1.6	5.5
120220_05	16	5.6	20.6	35.7	1202	1128	6.3	1.7	4.6
120120_04	16	5.6	27.2	42.1	1202	1137	6.2	1.6	3.9
120120_04	16	5.6	27.2	42.1	1202	1381	4.4	0.4	-6.4
112020_02	16	5.6	34.6	22.7	1202	1081	6.9	-0.5	8.5
112020_02	16	5.6	34.6	22.7	1202	1146	6.2	-0.8	3.3

Table B4.1 (continued): Filenames, He scattering conditions, and phonon data for TOF spectra taken along the $\overline{\Gamma X}$ axis.

Filename	E_i (meV)	k_i (Å^{-1})	θ_i (°)	θ_f (°)	t_0 (μs)	t_{obs} (μs)	k_f (Å^{-1})	ΔK (Å^{-1})	ΔE (meV)
081320_12_13_14_15_16_17	21	6.3	20.7	30.6	1066	927	8.4	2.0	15.6
081320_12_13_14_15_16_17	21	6.3	20.7	30.6	1066	1173	5.3	0.5	-6.1
080720_06	21	6.3	20.7	24.6	1067	1111	5.9	0.2	-2.9
080720_07	21	6.3	20.7	26.6	1067	1133	5.7	0.3	-4.1
080720_08	21	6.3	20.7	28.6	1067	922	8.5	1.8	16.8
080720_08	21	6.3	20.7	28.6	1067	1156	5.5	0.4	-5.3
080720_09	21	6.3	20.7	30.6	1067	1176	5.3	0.5	-6.1
080720_11	21	6.3	20.7	34.6	1067	952	7.9	2.3	12.0
080720_11	21	6.3	20.7	34.6	1067	1229	4.9	0.6	-8.2
080720_10	21	6.3	20.7	32.6	1067	942	8.1	2.1	13.5
080720_10	21	6.3	20.7	32.6	1067	1204	5.1	0.5	-7.3
082120_18	21	6.3	27.1	32.2	1067	1114	5.8	0.2	-3.0
080720_13	21	6.3	20.7	38.6	1068	970	7.6	2.5	9.5
090320_07	21	6.3	27.2	23.1	1068	1026	6.8	-0.2	3.4
090320_04	21	6.3	27.2	19.1	1068	989	7.3	-0.5	7.2
090320_05	21	6.3	27.2	20.1	1068	998	7.2	-0.4	6.2
080720_12	21	6.3	20.7	36.6	1068	962	7.8	2.4	10.6
082620_06_07	21	6.3	27.1	15.2	1068	949	8.0	-0.8	12.5
090320_06	21	6.3	27.2	22.1	1068	1017	6.9	-0.3	4.3
090220_10	21	6.3	27.2	18.1	1068	979	7.5	-0.6	8.4
082720_18_19_20	21	6.3	27.2	24.1	1068	1037	6.7	-0.2	2.5
091120_07	21	6.3	27.2	14.1	1068	949	8.0	-0.9	12.5
090220_07	21	6.3	27.2	15.1	1068	949	8.0	-0.8	12.5
082820_14_15_16	21	6.3	27.2	13.1	1068	948	8.0	-1.1	12.7
082820_17_18_19	21	6.3	27.2	14.1	1068	945	8.1	-0.9	13.1
082120_19	21	6.3	27.1	47.2	1068	983	7.4	2.6	8.0
082120_19	21	6.3	27.1	47.2	1068	1249	4.8	0.6	-8.8
090220_08	21	6.3	27.2	16.1	1068	962	7.8	-0.7	10.6
090220_09	21	6.3	27.2	17.1	1068	967	7.7	-0.6	10.0
091620_06	21	6.3	27.1	16.2	1069	955	7.9	-0.7	11.6
091620_08	21	6.3	27.1	16.7	1069	968	7.7	-0.7	9.9
091620_07	21	6.3	27.1	17.2	1069	977	7.5	-0.7	8.7

Table B4.2: Filenames, He scattering conditions, and phonon data for TOF spectra taken along the $\overline{\Gamma M}$ axis.

Filename	E_i (meV)	k_i (Å^{-1})	θ_i (°)	θ_f (°)	t_0 (μs)	t_{obs} (μs)	k_f (Å^{-1})	ΔK (Å^{-1})	ΔE (meV)
082220_04_05_06	21	6.3	27.1	32.2	1069	1112	5.9	0.2	-2.9
091620_09	21	6.3	27.1	15.7	1069	958	7.8	-0.8	11.2
091120_05	21	6.3	27.2	13.6	1069	950	8.0	-1.0	12.4
091120_08	21	6.3	27.2	14.6	1069	958	7.8	-0.9	11.2
081920_09	15	5.4	20.7	48.6	1247	1157	6.3	2.8	5.2
081420_08	10	4.3	21.1	29.2	1569	1723	3.6	0.2	-2.8
081420_06	10	4.3	21.1	25.2	1570	1644	3.9	0.1	-1.5
081420_07	10	4.3	21.1	27.2	1570	1688	3.8	0.2	-2.2
082020_05	10	4.3	27.2	20.4	1571	1456	5.0	-0.2	3.3
082020_08_09_10	10	4.3	27.2	31.1	1571	1629	4.0	0.1	-1.2
082020_11_12_13_14	10	4.3	27.2	34.1	1572	1682	3.8	0.2	-2.1
082120_04_05_06	10	4.3	27.3	34.0	1577	1685	3.8	0.2	-2.0

Table B4.2 (continued): Filenames, He scattering conditions, and phonon data for TOF spectra taken along the $\overline{\Gamma M}$ axis.

Appendix C

Copyright Attribution

Chapter 3 is an adapted version of the article, McMillan, A. A.; Graham, J. D.; Willson, S. A.; Farber, R. G.; Thompson, C. J.; Sibener, S. J. Persistence of the Nb(100) Surface Oxide Reconstruction at Elevated Temperatures. *Superconductor Science and Technology* **2020**, *33*, 105012, before peer review or editing, as submitted by A. A. McMillan to *Superconductor Science and Technology*. IOP Publishing Ltd is not responsible for any errors or omissions in this version of the manuscript or any version derived from it. The Version of Record is available online at https://iopscience.iop.org/article/10.1088/1361-6668/abaec0.[66]

Chapter 4 is a modified version of an article submitted for publication to *The Journal of Chemical Physics*.

Appendix A is adapted with permission from Thompson, R. S.; Brann, M. R.; Purdy, E. H.; Graham, J. D.; McMillan, A. A.; Sibener, S. J. Rapid Laser-Induced Temperature Jump Decomposition of the Nerve Agent Simulant Diisopropyl Methylphosphonate under Atmospheric Conditions. *The Journal of Physical Chemistry C* **2019**, *123*, 21564–21570. Copyright 2019 American Chemical Society.[155]

References

(1) Somorjai, G. A.; Li, Y. Impact of Surface Chemistry. *PNAS* **2011**, *108*, 917–924.

(2) Benedek, G.; Toennies, J. P. *Atomic Scale Dynamics at Surfaces*; Springer Series in Surface Sciences; Springer-Verlag: Berlin, 2018; Vol. 63.

(3) *Atomic and Molecular Beam Methods, Vol. 1*; Scoles, G., Ed.; Oxford University Press: New York, 1988.

(4) Farías, D.; Rieder, K.-H. Atomic Beam Diffraction from Solid Surfaces. *Reports Prog. Phys.* **1998**, *61*, 1575–1664.

(5) Posen, S.; Liepe, M. Advances in Development of Nb_3Sn Superconducting Radio-Frequency Cavities. *Phys. Rev. Spec. Top. - Accel. Beams* **2014**, *17*, 112001.

(6) Hamm, R. W.; Hamm, M. E. *Industrial Accelerators and Their Applications*; World Scientific: Singapore, 2012.

(7) Posen, S.; Hall, D. L. Nb_3Sn Superconducting Radiofrequency Cavities: Fabrication, Results, Properties, and Prospects. *Supercond. Sci. Technol.* **2017**, *30*, 033004.

(8) Hulpke, E. *Helium Atom Scattering from Surfaces*; Hulpke, E., Ed.; Springer Series in Surface Science; Springer-Verlag: Berlin, 1992; Vol. 27.

(9) Kittel, C. *Introduction to Solid State Physics*, 8th ed.; Wiley: New York, 2005.

(10) Ashcroft, N. W.; Mermin, N. D. *Solid State Physics*; Cengage Learning: Delhi, 1976.

(11) Dove, M. T. *Introduction to Lattice Dynamics*; Cambridge University Press: Cambridge, 1993.

(12) Estermann, I.; Stern, O. Beugung Yon Molekularstrahlen. *Zeitschrift für Phys.* **1930**, *61*, 95–125.

(13) Morse, M. D. 2. Supersonic Beam Sources. *Experimental Methods in the Physical Sciences*. 1996, pp 21–47.

(14) Atkins, P.; de Paula, J.; Friedman, R. *Physical Chemistry*, 2nd ed.; Oxford University Press: New York, 2014.

(15) Comsa, G. Coherence Length and/or Transfer Width? *Surf. Sci.* **1979**, *81*, 57–68.

(16) Lapujoulade, J.; Lejay, Y.; Armand, G. The Thermal Attenuation of Coherent Elastic Scattering of Noble Gas from Metal Surfaces. *Surf. Sci.* **1980**, *95*, 107–130.

(17) Koleske, D. D.; Sibener, S. J. Generation of Pseudorandom Sequences for Use in Cross-Correlation Modulation. *Rev. Sci. Instrum.* **1992**, *63*, 3855.

(18) *Atomic and Molecular Beam Methods, Vol. 2*; Scoles, G., Ed.; Oxford University Press: New York, 1992.

(19) Padamsee, H. The Science and Technology of Superconducting Cavities for Accelerators. *Supercond. Sci. Technol.* **2001**, *14*, R28–R51.

(20) Reece, C. E. Continuous Wave Superconducting Radio Frequency Electron Linac for Nuclear Physics Research. *Phys. Rev. Accel. Beams* **2016**, *19*, 124801.

(21) Ford, D. C.; Cooley, L. D.; Seidman, D. N. Suppression of Hydride Precipitates in Niobium Superconducting Radio-Frequency Cavities. *Supercond. Sci. Technol.* **2013**, *26*, 105003.

(22) Ma, Q.; Ryan, P.; Freeland, J. W.; Rosenberg, R. A. Thermal Effect on the Oxides on Nb(100) Studied by Synchrotron-Radiation x-Ray Photoelectron Spectroscopy. *J. Appl. Phys.* **2004**, *96*, 7675–7680.

(23) Romanenko, A.; Grassellino, A.; Barkov, F.; Ozelis, J. P. Effect of Mild Baking on Superconducting Niobium Cavities Investigated by Sequential Nanoremoval. *Phys. Rev. Spec. Top. - Accel. Beams* **2013**, *16*, 012001.

(24) Grassellino, A.; Romanenko, A.; Sergatskov, D.; Melnychuk, O.; Trenikhina, Y.; Crawford, A.; Rowe, A.; Wong, M.; Khabiboulline, T.; Barkov, F. Nitrogen and Argon Doping of Niobium for Superconducting Radio Frequency Cavities: A Pathway to Highly Efficient Accelerating Structures. *Supercond. Sci. Technol.* **2013**, *26*, 102001.

(25) Grassellino, A.; Romanenko, A.; Trenikhina, Y.; Checchin, M.; Martinello, M.; Melnychuk, O. S.; Chandrasekaran, S.; Sergatskov, D. A.; Posen, S.; Crawford, A. C.; Aderhold, S.; Bice, D. Unprecedented Quality Factors at Accelerating Gradients up to 45 MVm^{-1} in Niobium Superconducting Resonators via Low Temperature Nitrogen Infusion. *Supercond. Sci. Technol.* **2017**, *30*, 094004.

(26) Lee, J.; Mao, Z.; He, K.; Sung, Z. H.; Spina, T.; Baik, S.-I.; Hall, D. L.; Liepe, M.; Seidman, D. N.; Posen, S. Grain-Boundary Structure and Segregation in Nb_3Sn Coatings on Nb for High-Performance Superconducting Radiofrequency Cavity Applications. *Acta Mater.* **2020**, *188*, 155–165.

(27) Becker, C.; Posen, S.; Groll, N.; Cook, R.; Schlepütz, C. M.; Hall, D. L.; Liepe, M.; Pellin, M.; Zasadzinski, J.; Proslier, T. Analysis of Nb_3Sn Surface Layers for Superconducting Radio Frequency Cavity Applications. *Appl. Phys. Lett.* **2015**, *106*, 082602.

(28) Trenikhina, Y.; Posen, S.; Romanenko, A.; Sardela, M.; Zuo, J.-M.; Hall, D. L.; Liepe, M. Performance-Defining Properties of Nb_3Sn Coating in SRF Cavities. *Supercond. Sci. Technol.* **2018**, *31*, 015004.

(29) Dickey, J. M.; Strongin, M.; Kammerer, O. F. Studies of Thin Films of Nb_3Sn on Nb. *J. Appl. Phys.* **1971**, *42*, 5808–5820.

(30) Porter, R. D.; Arias, T.; Cueva, P.; Hall, D. L.; Liepe, M.; Maniscalco, J. T.; Muller, D. A.; Sitaraman, N. Next Generation Nb_3Sn SRF Cavities for Linear Accelerators. *29th Linear Accel. Conf.* **2018**, 462–465.

(31) Kneisel, P.; Stoltz, O.; Halbritter, J. Measurements of Superconducting Nb_3Sn Cavities in the GHz Range. *IEEE Trans. Magn.* **1979**, *15*, 21–24.

(32) Arnolds, G.; Proch, D. Measurement on a Nb_3Sn Structure for Linear Accelerator Application. *IEEE Trans. Magn.* **1977**, *13*, 500–503.

(33) Posen, S.; Liepe, M. Stoichiometric Nb_3Sn in First Samples Coated at Cornell. *15th Conf. RF Supercond.* **2011**, 886–889.

(34) Farrell, H. H.; Isaacs, H. S.; Strongin, M. The Interaction of Oxygen and Nitrogen with the Niobium (100) Surface: II. Reaction Kinetics. *Surf. Sci.* **1973**, *38*, 31–52.

(35) Farrell, H. H.; Strongin, M. The Interaction of Oxygen and Nitrogen with the Niobium (100) Surface: I. Morphology. *Surf. Sci.* **1973**, *38*, 18–30.

(36) An, B.; Fukuyama, S.; Yokogawa, K.; Yoshimura, M. Surface Structures of Clean and Oxidized Nb(100) by LEED, AES, and STM. *Phys. Rev. B* **2003**, *68*, 115423.

(37) Lindau, I.; Spicer, W. E. Oxidation of Nb as Studied by the UV-Photoemission Technique. *J. Appl. Phys.* **1974**, *45*, 3720–3725.

(38) Wang, Y.; Wei, X.; Tian, Z.; Cao, Y.; Zhai, R.; Ushikubo, T.; Sato, K.; Zhuang, S. An AES, UPS and HREELS Study of the Oxidation and Reaction of Nb(110). *Surf. Sci.* **1997**, *372*, L285–L290.

(39) Veit, R. D.; Kautz, N. A.; Farber, R. G.; Sibener, S. J. Oxygen Dissolution and Surface Oxide Reconstructions on Nb(100). *Surf. Sci.* **2019**, *688*, 63–68.

(40) Uehara, Y.; Fujita, T.; Iwami, M.; Ushioda, S. Single NbO Nano-Crystal Formation on Low Temperature Annealed Nb(001) Surface. *Surf. Sci.* **2001**, *472*, 59–62.

(41) Arfaoui, I.; Cousty, J.; Guillot, C. A Model of the $NbO_{x\approx1}$ Nanocrystals Tiling a Nb(110) Surface Annealed in UHV. *Surf. Sci.* **2004**, *557*, 119–128.

(42) Musket, R. G.; McLean, W.; Colmenares, C. A.; Makowiecki, D. M.; Siekhaus, W. J. Preparation of Atomically Clean Surfaces of Selected Elements: A Review. *Appl. Surf. Sci.* **1982**, *10*, 143–207.

(43) Franchy, R.; Bartke, T. U.; Gassmann, P. The Interaction of Oxygen with Nb(110) at 300, 80 and 20 K. *Surf. Sci.* **1996**, *366*, 60–70.

(44) Pantel, R.; Bujor, M.; Bardolle, J. Continuous Measurement of Surface Potential Variations during Oxygen Adsorption on the (100), (110) and (111) Faces of Niobium Using Mirror Electron Microscope. *Surf. Sci.* **1977**, *62*, 589–609.

(45) Dawson, P. H.; Tam, W.-C. The Interaction of Oxygen with Polycrystalline Niobium Studied Using AES and Low-Energy SIMS. *Surf. Sci.* **1979**, *81*, 464–478.

(46) Usami, S.; Tominaga, N.; Nakajima, T. AES-LEED Study of Adsorption of Common Gases on the (100) Planes of W and Nb. *Vacuum* **1976**, *27*, 11–16.

(47) Hulpke, E.; Hüppauff, M.; Smilgies, D.-M.; Kulkarni, A. D.; de Wette, F. W. Lattice Dynamics of the Niobium (001) Surface. *Phys. Rev. B* **1992**, *45*, 1820–1828.

(48) Meyer, E.; Hug, H. J.; Bennewitz, R. *Scanning Probe Microscopy: The Lab on a Tip*; Advanced Texts in Physics; Springer-Verlag: Berlin, 2004.

(49) Gans, B.; Knipp, P. A.; Koleske, D. D.; Sibener, S. J. Surface Dynamics of Ordered $Cu_3Au(001)$ Studied by Elastic and Inelastic Helium Atom Scattering. *Surf. Sci.* **1992**, *264*, 81–94.

(50) Li, Y.; An, B.; Xu, X.; Fukuyama, S.; Yokogawa, K.; Yoshimura, M. Surface Structure of Niobium-Dioxide Overlayer on Niobium(100) Identified by Scanning Tunneling Microscopy. *J. Appl. Phys.* **2001**, *89*, 4772–4776.

(51) Engel, T.; Rieder, K.-H. Structural Studies of Surfaces with Atomic and Molecular Beam Diffraction. In *Structural Studies of Surfaces*; Springer Tracts in Modern Physics; Springer-Verlag: Berlin, 1982; Vol. 91, pp 55–180.

(52) Lapujoulade, J.; Lejay, Y.; Armand, G. The Thermal Attentuation of Coherent Elastic Scattering of Noble Gas from Metal Surfaces. *Surf. Sci.* **1980**, *95*, 107–130.

(53) Becker, J. S.; Brown, R. D.; Johansson, E.; Lewis, N. S.; Sibener, S. J. Helium Atom Diffraction Measurements of the Surface Structure and Vibrational Dynamics of CH_3-Si(111) and CD_3-Si(111) Surfaces. *J. Chem. Phys.* **2010**, *133*, 104705.

(54) Veit, R. D.; Farber, R. G.; Sitaraman, N. S.; Arias, T. A.; Sibener, S. J. Suppression of Nano-Hydride Growth on Nb(100) Due to Nitrogen Doping. *J. Chem. Phys.* **2020**, *152*, 214703.

(55) Davis, L. *Handbook of Auger Electron Spectroscopy*, 2nd ed.; Physical Electronics Industries: Eden Prairie, 1976.

(56) Padamsee, H.; Shepard, K. W.; Sundelin, R. Physics and Accelerator Applications of RF Superconductivity. *Annu. Rev. Part. Nucl. Sci.* **1993**, *43*, 635–686.

(57) Finnemore, D. K.; Stromberg, T. F.; Swenson, C. A. Superconducting Properties of High-Purity Niobium. *Phys. Rev.* **1966**, *149*, 231–243.

(58) Padamsee, H.; Knobloch, J.; Hays, T. *RF Superconductivity for Accelerators*; Wiley-VCH: New York, 2008.

(59) Gerigk, F. Superconducting RF at CERN: Operation, Projects, and R&D. *IEEE Trans. Appl. Supercond.* **2018**, *28*, 3500205.

(60) Broemmelsiek, D.; Chase, B.; Edstrom, D.; Harms, E.; Leibfritz, J.; Nagaitsev, S.; Pischalnikov, Y.; Romanov, A.; Ruan, J.; Schappert, W.; Shiltsev, V.; Thurman-Keup, R.; Valishev, A. Record High-Gradient SRF Beam Acceleration at Fermilab. *New J. Phys.* **2018**, *20*, 113018.

(61) Dhakal, P.; Ciovati, G.; Kneisel, P.; Myneni, G. R. Enhancement in Quality Factor of SRF Niobium Cavities by Material Diffusion. *IEEE Trans. Appl. Supercond.* **2015**, *25*, 3500104.

(62) Sürgers, C.; Schöck, M.; Löhneysen, H. V. Oxygen-Induced Surface Structure of Nb(110). *Surf. Sci.* **2001**, *471*, 209–218.

(63) Li, Y.; An, B.; Fukuyama, S.; Yokogawa, K.; Yoshimura, M. Surface Oxidation of a Nb(100) Single Crystal by Scanning Tunneling Microscopy. In *Materials Characterization*; 2002; Vol. 48, pp 163–167.

(64) Arfaoui, I.; Guillot, C.; Cousty, J.; Antoine, C. Evidence for a Large Enrichment of Interstitial Oxygen Atoms in the Nanometer-Thick Metal Layer at the NbO/Nb(110) Interface. *J. Appl. Phys.* **2002**, *91*, 9319–9323.

(65) Grundner, M.; Halbritter, J. XPS and AES Studies on Oxide Growth and Oxide Coatings on Niobium. *J. Appl. Phys.* **1980**, *51*, 397–405.

(66) McMillan, A. A.; Graham, J. D.; Willson, S. A.; Farber, R. G.; Thompson, C. J.; Sibener, S. J. Persistence of the Nb(100) Surface Oxide Reconstruction at Elevated Temperatures. *Supercond. Sci. Technol.* **2020**, *33*, 105012.

(67) Estermann, I.; Stern, O. Beugung von Molekularstrahlen. *Zeitschrift f{ü}r Phys.* **1930**, *61*, 95–125.

(68) Toennies, J. P. Helium Atom Scattering: A Gentle and Uniquely Sensitive Probe of Surface Structure and Dynamics. *J. Phys. Condens. Matter* **1993**, *5*, A25–A40.

(69) Benedek, G.; Toennies, J. P. Helium Atom Scattering Spectroscopy of Surface Phonons: Genesis and Achievements. *Surf. Sci.* **1994**, *299/300*, 587–611.

(70) Schober, H. R.; Dederichs, P. H. *Phonon States of Elements. Electron States and Fermi Surfaces of Alloys*; Hellwege, K.-H., Olsen, J. L., Eds.; Landolt-Börnstein - Group III Condensed Matter 13A; Springer-Verlag: Berlin Heidelberg, 1981.

(71) Nakagawa, Y.; Woods, A. D. B. Lattice Dynamics of Niobium. *Phys. Rev. Lett.* **1963**, *11*, 271–274.

(72) Sharp, R. I. The Lattice Dynamics of Niobium I. Measurements of the Phonon Frequencies. *J. Phys. C Solid State Phys.* **1969**, *2*, 421–431.

(73) Sharp, R. I. The Lattice Dynamics of Niobium II. Kohn Anomalies in Niobium. *J. Phys. C Solid State Phys.* **1969**, *2*, 432–443.

(74) Geerlings, P.; De Proft, F.; Langenaeker, W. Conceptual Density Functional Theory. *Chem. Rev.* **2003**, *103*, 1874.

(75) Payne, M. C.; Teter, M. P.; Allan, D. C.; Arias, T. A.; Joannopoulos, J. D. Iterative Minimization Techniques for Ab Initio Total-Energy Calculations: Molecular Dynamics and Conjugate Gradients. *Rev. Mod. Phys.* **1992**, *64*, 1045–1097.

(76) Sundararaman, R.; Letchworth-Weaver, K.; Schwarz, K. A.; Gunceler, D.; Ozhabes, Y.; Arias, T. A. JDFTx: Software for Joint Density-Functional Theory. *SoftwareX* **2017**, *6*, 278–284.

(77) Perdew, J. P.; Ruzsinszky, A.; Csonka, G. I.; Vydrov, O. A.; Scuseria, G. E.; Constantin, L. A.; Zhou, X.; Burke, K. Restoring the Density-Gradient Expansion for Exchange in Solids and Surfaces. *Phys. Rev. Lett.* **2008**, *100*, 136406.

(78) Garrity, K. F.; Bennett, J. W.; Rabe, K. M.; Vanderbilt, D. Pseudopotentials for High-Throughput DFT Calculations. *Comput. Mater. Sci.* **2014**, *81*, 446–452.

(79) Brown, A. M.; Sundararaman, R.; Narang, P.; Goddard III, W. A.; Atwater, H. A. Nonradiative Plasmon Decay and Hot Carrier Dynamics: Effects of Phonons, Surfaces, and Geometry. *ACS Nano* **2016**, *10*, 957–966.

(80) Marzari, N.; Vanderbilt, D. Maximally Localized Generalized Wannier Functions for Composite Energy Bands. *Phys. Rev. B* **1997**, *56*, 12847–12865.

(81) González-Pedreros, G. I.; Camargo-Martínez, J. A.; Mesa, F. Cooper Pairs Distribution Function for BCC Niobium under Pressure from First-Principles. *Sci. Rep.* **2021**, *11*, 7646.

(82) Brown, A. M.; Sundararaman, R.; Narang, P.; Goddard III, W. A.; Atwater, H. A. Ab Initio Phonon Coupling and Optical Response of Hot Electrons in Plasmonic Metals. *Phys. Rev. B* **2016**, *94*, 075120.

(83) Eliashberg, G. M. Interactions between Electrons and Lattice Vibrations in a Superconductor. *Sov. Phys. JETP* **1960**, *11*, 696–702.

(84) Allen, P. B. Neutron Spectroscopy of Superconductors. *Phys. Rev. B* **1972**, *6*, 2577–2579.

(85) Giustino, F.; Cohen, M. L.; Louie, S. G. Electron-Phonon Interaction Using Wannier Functions. *Phys. Rev. B* **2007**, *76*, 165108.

(86) Butler, W. H.; Pinski, I. J.; Allen, P. B. Phonon Linewidths and Electron-Phonon Interaction in Nb. *Phys. Rev. B* **1979**, *19*, 3708–3721.

(87) Sklyadneva, I. Y.; Benedek, G.; Chulkov, E. V; Echenique, P. M.; Heid, R.; Bohnen, K. P.; Toennies, J. P. Mode-Selected Electron-Phonon Coupling in Superconducting Pb Nanofilms Determined from He Atom Scattering. *Phys. Rev. Lett.* **2011**, *107*, 1–4.

(88) Tamtögl, A.; Kraus, P.; Mayrhofer-Reinhartshuber, M.; Campi, D.; Bernasconi, M.; Benedek, G.; Ernst, W. E. Surface and Subsurface Phonons of Bi(111) Measured with Helium Atom Scattering. *Phys. Rev. B* **2013**, *87*, 35410.

(89) Benedek, G.; Bernasconi, M.; Bohnen, K. P.; Campi, D.; Chulkov, E. V; Echenique, P. M.; Heid, R.; Sklyadneva, I. Y.; Toennies, J. P. Unveiling Mode-Selected Electron-Phonon Interactions in Metal Films by Helium Atom Scattering. *Phys. Chem. Chem. Phys.* **2014**, *16*, 7159–7172.

(90) Manson, J. R.; Benedek, G.; Miret-Arte, S. Electron−Phonon Coupling Strength at Metal Surfaces Directly Determined from the Helium Atom Scattering Debye−Waller Factor. *J. Phys. Chem. Lett* **2016**, *7*, 32.

(91) Hofmann, P.; Sklyadneva, I. Y.; Rienks, E. D. L.; Chulkov, E. V. Electron-Phonon Coupling at Surfaces and Interfaces. *New J. Phys.* **2009**, *11*, 125005.

(92) Bortolani, V.; Franchini, A.; Garcia, N.; Nizzoli, F.; Santoro, G. Calculation of Potential Cutoff for One-Phonon Atom-Surface Scattering. *Phys. Rev. B* **1983**, *28*, 7358–7361.

(93) Benedek, G.; Bernasconi, M.; Chis, V.; Chulkov, E.; Echenique, P. M.; Hellsing, B.; Toennies, J. P. Theory of Surface Phonons at Metal Surfaces: Recent Advances. *J. Phys. Condens. Matter* **2010**, *22*, 084020.

(94) Kröger, J. Electron-Phonon Coupling at Metal Surfaces. *Reports Prog. Phys.* **2006**, *69*, 899–969.

(95) Miyake, T.; Petek, H. Atomic Hydrogen Modification of Copper Surfaces Helium Atom Scattering. *Appl. Surf. Sci.* **1997**, *121–122*, 138–141.

(96) Van Der Veen, J. F.; Frenken, J. W. M. Dynamics and Melting of Surfaces. *Surf. Sci.* **1986**, *178*, 382–395.

(97) Pluis, B.; Denier van der Gon, A. W.; Frenken, J. W. M.; van der Veen, J. F. Crystal-Face Dependence of Surface Melting. *Phys. Rev. Lett.* **1987**, *59*, 2678–2681.

(98) Charlesworth, J. P.; MacPhail, I.; Madsen, P. E. Experimental Work on the Niobium-Tin Constitution Diagram and Related Studies. *J. Mater. Sci.* **1970**, *5*, 580–603.

(99) Farber, R. G.; Willson, S. A.; Sibener, S. J. Role of Nanoscale Surface Defects on Sn Adsorption and Diffusion Behavior on Oxidized Nb(100). *J. Vac. Sci. Technol. A* **2021**, *39*, 063212.

(100) Benedek, G.; Miret-Artés, S.; Toennies, J. P.; Manson, J. R. Electron–Phonon Coupling Constant of Metallic Overlayers from Specular He Atom Scattering. *J. Phys. Chem. Lett.* **2018**, *9*, 76–83.

(101) Tamtögl, A.; Kraus, P.; Avidor, N.; Bremholm, M.; Hedegaard, E. M. J.; Iversen, B. B.; Bianchi, M.; Hofmann, P.; Ellis, J.; Allison, W.; Benedek, G.; Ernst, W. E. Electron-Phonon Coupling and Surface Debye Temperature of Bi_2Te_3 (111) from Helium Atom Scattering. *Phys. Rev. B* **2017**, *95*, 195401.

(102) Anemone, G.; Taleb, A. Al; Benedek, G.; Castellanos-Gomez, A.; Farías, D. Electron–Phonon Coupling Constant of 2H-MoS_2 (0001) from Helium-Atom Scattering. *J. Phys. Chem. C* **2019**, *123*, 3682–3686.

(103) Jardine, A. P.; Ellis, J.; Allison, W. Quasi-Elastic Helium-Atom Scattering from Surfaces: Experiment and Interpretation. *J. Phys. Condens. Matter* **2002**, *14*, 6173–6191.

(104) Korobeinichev, O. P.; Chernov, A. A.; Sokolov, V. V.; Krasnoperov, L. N. Kinetics of Destruction of Diisopropyl Methylphosphonate in Corona Discharge. *Int. J. Chem. Kinet.* **2002**, *34*, 331–337.

(105) Korobeinichev, O. P.; Ilyin, S. B.; Shvartsberg, V. M.; Chernov, A. A. The Destruction Chemistry of Organophosphorus Compounds in Flames—I: Quantitative Determination of Final Phosphorus-Containing Species in Hydrogen-Oxygen Flames. *Combust. Flame* **1999**, *118*, 718–726.

(106) Ganesan, K.; Raza, S. K.; Vijayaraghavan, R. Chemical Warfare Agents. *J. Pharm. Bioallied Sci.* **2010**, *2*, 178.

(107) Kim, K.; Tsay, O. G.; Atwood, D. A.; Churchill, D. G. Destruction and Detection of Chemical Warfare Agents. *Chem. Rev.* **2011**, *111*, 5345–5403.

(108) Munro, N. B.; Talmage, S. S.; Griffin, G. D.; Waters, L. C.; Watson, A. P.; King, J. F.; Hauschild, V. The Sources, Fate, and Toxicity of Chemical Warfare Agent Degradation Products. *Environ. Health Perspect.* **1999**, *107*, 933–974.

(109) National Research Council. Review of Acute Human-Toxicity Estimates for GB (Sarin). In *Review of Acute Human-Toxicity Estimates for Selected Chemical-Warfare Agents*; National Academies Press (US): Washington (DC), 1997; pp 28–34.

(110) Szinicz, L. History of Chemical and Biological Warfare Agents. *Toxicology* **2005**, *214*, 167–181.

(111) Aschmann, S. M.; Tuazon, E. C.; Atkinson, R. Atmospheric Chemistry of Diethyl Methylphosphonate, Diethyl Ethylphosphonate, and Triethyl Phosphate. *J. Phys. Chem. A* **2005**, *109*, 2282–2291.

(112) Davis, E. D.; Gordon, W. O.; Wilmsmeyer, A. R.; Troya, D.; Morris, J. R. Chemical Warfare Agent Surface Adsorption: Hydrogen Bonding of Sarin and Soman to Amorphous Silica. *J. Phys. Chem. Lett.* **2014**, *5*, 1393–1399.

(113) Wilmsmeyer, A. R.; Gordon, W. O.; Davis, E. D.; Troya, D.; Mantooth, B. A.; Lalain, T. A.; Morris, J. R. Infrared Spectra and Binding Energies of Chemical Warfare Nerve Agent Simulants on the Surface of Amorphous Silica. *J. Phys. Chem. C* **2013**, *117*, 15685–15697.

(114) Zegers, E. J. P.; Fisher, E. M. Gas-Phase Pyrolysis of Diisopropyl Methylphosphonate. *Combust. Flame* **1998**, *115*, 230–240.

(115) Glaude, P. A.; Melius, C.; Pitz, W. J.; Westbrook, C. K. Detailed Chemical Kinetic Reaction Mechanisms for Incineration of Organophosphorus and Fluoroorganophosphorus Compounds. *Proc. Combust. Inst.* **2002**, *29*, 2469–2476.

(116) Kuiper, A. E. T.; van Bokhoven, J. J. G. M.; Medema, J. The Role of Heterogeneity in the Kinetics of a Surface Reaction: I. Infrared Characterization of the Adsorption Structures of Organophosphonates and Their Decomposition. *J. Catal.* **1976**, *43*, 154–167.

(117) Zegers, E. J. P.; Fisher, E. M. Gas-Phase Pyrolysis of Diethyl Methylphosphonate. *Combust. Sci. Technol.* **1996**, *116–117*, 69–89.

(118) Paciorek, K. J. L.; Kratzer, R. H.; Kaufman, J.; Nakahara, J. H.; Christos, T.; Hartstein, A. M. Thermal Oxidative Degradation Studies of Phosphate Esters. *Am. Ind. Hyg. Assoc. J.* **1978**, *39*, 633–639.

(119) Lhomme, V.; Bruneau, C.; Soyer, N.; Brault, A. Thermal Behavior of Some Organic Phosphates. *Ind. Eng. Chem. Prod. Res. Dev.* **1984**, *23*, 98–102.

(120) Higgins, C. E.; Baldwin, W. H. The Thermal Decomposition of Tributyl Phosphate. *J. Org. Chem.* **1961**, *26*, 846–850.

(121) Bruneau, C.; Soyer, N.; Brault, A.; Kerfanto, M. Thermal Degradation of Tri-n-Butyl Phosphate. *J. Anal. Appl. Pyrolysis* **1981**, *3*, 71–81.

(122) Yang, L.; Shroll, R. M.; Zhang, J.; Lourderaj, U.; Hase, W. L. Theoretical Investigation of Mechanisms for the Gas-Phase Unimolecular Decomposition of DMMP. *J. Phys. Chem. A* **2009**, *113*, 13762–13771.

(123) Glaude, P. A.; Curran, H. J.; Pitz, W. J.; Westbrook, C. K. Kinetic Study of the Combustion of Organophosphorus Compounds. *Proc. Combust. Inst.* **2000**, *28*, 1749–1756.

(124) Thompson, R. S.; Langlois, G. G.; Sibener, S. J. Oxidative Destruction of Multilayer Diisopropyl Methylphosphonate Films by $O(^3P)$ Atomic Oxygen. *J. Phys. Chem. B* **2018**, *122*, 455–463.

(125) Langlois, G. G.; Thompson, R. S.; Li, W.; Sibener, S. J. Oxidation, Destruction, and Persistence of Multilayer Dimethyl Methylphosphonate Films during Exposure to O(^{3}P) Atomic Oxygen. *J. Phys. Chem. C* **2016**, *120*, 16863–16870.

(126) Gibson, K. D.; Sibener, S. J. Fate of Some Chemical Warfare Simulants Adsorbed on an Inert Surface When Exposed to Rapid Laser Initiated Heating. *J. Phys. Chem. C* **2018**, *122*, 24684–24689.

(127) Oppelt, E. T. Incineration of Hazardous Waste. *JAPCA* **1987**, *37*, 558–586.

(128) Bulgakova, N. M.; Bulgakov, A. V. Pulsed Laser Ablation of Solids: Transition from Normal Vaporization to Phase Explosion. *Appl. Phys. A* **2001**, *73*, 199–208.

(129) Smausz, T.; Kondász, B.; Gera, T.; Ajtai, T.; Utry, N.; Pintér, M.; Kiss-Albert, G.; Budai, J.; Bozóki, Z.; Szabó, G.; Hopp, B. Determination of UV–Visible–NIR Absorption Coefficient of Graphite Bulk Using Direct and Indirect Methods. *Appl. Phys. A Mater. Sci. Process.* **2017**, *123*, 633.

(130) Schultrich, B. Carbon Ablation with ns Lasers. In *Tetrahedrally bonded amorphous carbon films*; Springer: Berlin, Heidelberg, 2018; pp 585–631.

(131) Kononenko, V. V.; Kononenko, T. V.; Pimenov, S. M.; Sinyavskii, M. N.; Konov, V. I.; Dausinger, F. Effect of the Pulse Duration on Graphitization of Diamond during Laser Ablation. *Quantum Electron.* **2005**, *35*, 252–256.

(132) Ready, J. F. *Effects of High-Power Laser Radiation*; Academic Press: New York, NY, 1971.

(133) Windholz, R.; Molian, P. A. Nanosecond Pulsed Excimer Laser Machining of Chemically Vapour-Deposited Diamond and Graphite: Part II Analysis and Modelling. *J. Mater. Sci.* **1998**, *33*, 523–528.

(134) Gibb, S.; Strimmer, K. MALDIquant: A Versatile R Package for the Analysis of Mass Spectrometry Data. *Bioinformatics* **2012**, *28*, 2270–2271.

(135) Savitzky, A.; Golay, M. J. E. Smoothing and Differentiation of Data by Simplified Least Squares Procedures. *Anal. Chem.* **1964**, *36*, 1627–1639.

(136) Stein, S. E. Mass Spectra. In *NIST Chemistry WebBook*; Linstrom, P. J., Mallard, W. G., Eds.; NIST Standard Reference Database Number 69; National Institute of Standards and Technology: Gaithersburg MD, 2018.

(137) Korobeinichev, O. P.; Shvartsberg, V. M.; Shmakov, A. G. The Chemistry of Combustion of Organophosphorus Compounds. *Russ. Chem. Rev.* **2007**, *76*, 1094–1121.

(138) Radziemski, L. J. Laser-induced Photodestruction of the Organo-phosphates: DIMP and DMMP. *J. Environ. Sci. Heal. Part B* **1981**, *16*, 337–361.

(139) Templeton, M. K.; Weinberg, W. H. Decomposition of Phosphonate Esters Adsorbed on Aluminum Oxide. *J. Am. Chem. Soc.* **1985**, *107*, 774–779.

(140) Guilbault, G. G.; Scheide, E.; Das, J. An Experimental Technique for Studying the Infrared Spectrum of Chemisorbed Compounds. *Spectrosc. Lett.* **1968**, *1*, 167–175.

(141) Crooks, R. M.; Yang, H. C.; McEllistrem, L. J.; Thomas, R. C.; Ricco, A. J. Interactions between Self-Assembled Monolayers and an Organophosphonate Detailed Study Using Surface Acoustic Wave-Based Mass Analysis, Polarization Modulation-FTIR Spectroscopy and Ellipsometry. *Faraday Discuss.* **1997**, *107*, 285–305.

(142) van Hest, M. F. A. M.; de Graaf, A.; van de Sanden, M. C. M.; Schram, D. C. Use of in situ FTIR Spectroscopy and Mass Spectrometry in an Expanding Hydrocarbon Plasma. *Plasma Sources Sci. Technol.* **2000**, *9*, 624.

(143) Kaiser, R. I.; Roessler, K. Theoretical and Laboratory Studies on the Interaction of Cosmic-Ray Particles with Interstellar Ices. III. Suprathermal Chemistry-Induced Formation of Hydrocarbon Molecules in Solid Methane (CH_4), Ethylene (C_2H_4), and Acetylene (C_2H_2). *Astrophys. J.* **1998**, *503*, 959–975.

(144) Silvi, B.; Labarbe, P.; Perchard, J. P. Spectres de Vibration et Coordonnées Normales de Quatre Espèces Isotopiques de Propène. *Spectrochim. Acta Part A Mol. Spectrosc.* **1973**, *29*, 263–276.

(145) Es-sebbar, E. -t.; Alrefae, M.; Farooq, A. Infrared Cross-Sections and Integrated Band Intensities of Propylene: Temperature-Dependent Studies. *J. Quant. Spectrosc. Radiat. Transf.* **2014**, *133*, 559–569.

(146) Yuan, B.; Eilers, H. T-Jump Pyrolysis and Combustion of Diisopropyl Methylphosphonate. *Combust. Flame* **2019**, *199*, 69–84.

(147) Shan, X.; Vincent, J. C.; Kirkpatrick, S.; Walker, M. D.; Sambrook, M. R.; Clary, D. C. A Combined Theoretical and Experimental Study of Sarin (GB) Decomposition at High Temperatures. *J. Phys. Chem. A* **2017**, *121*, 6200–6210.

(148) Ash, T.; Debnath, T.; Banu, T.; Das, A. K. Exploration of Unimolecular Gas-Phase Detoxication Pathways of Sarin and Soman: A Computational Study from the Perspective of Reaction Energetics and Kinetics. *Chem. Res. Toxicol.* **2016**, *29*, 1439–1457.

(149) Hahn, D. K.; RaghuVeer, K. S.; Ortiz, J. V. Computational Tests of Models for Kinetic Parameters of Unimolecular Reactions of Organophosphorus and Organosulfur Compounds. *J. Phys. Chem. A* **2011**, *115*, 14143–14152.

(150) Hidaka, Y.; Nakamura, T.; Tanaka, H.; Jinno, A.; Kawano, H.; Higashihara, T. Shock Tube and Modeling Study of Propene Pyrolysis. *Int. J. Chem. Kinet.* **1992**, *24*, 761–780.

(151) Davis, S. G.; Law, C. K.; Wang, H. Propene Pyrolysis and Oxidation Kinetics in a Flow Reactor and Laminar Flames. *Combust. Flame* **1999**, *119*, 375–399.

(152) Milne, G. S.; Steel, C. The Gas-Phase Oxidation of Photochemically Generated Isopropyl Radicals. *J. Phys. Chem.* **1968**, *72*, 3754–3761.

(153) Atkinson, R.; Carter, W. P. L. Reactions of Alkoxy Radicals under Atmospheric Conditions: The Relative Importance of Decomposition versus Reaction with O_2. *J. Atmos. Chem.* **1991**, *13*, 195–210.

(154) Wijnen, M. J. H. Reactions of Alkoxy Radicals. VI. Photolysis of Isopropyl Propionate. *J. Am. Chem. Soc.* **1960**, *82*, 1847–1849.

(155) Thompson, R. S.; Brann, M. R.; Purdy, E. H.; Graham, J. D.; McMillan, A. A.; Sibener, S. J. Rapid Laser-Induced Temperature Jump Decomposition of the Nerve Agent Simulant Diisopropyl Methylphosphonate under Atmospheric Conditions. *J. Phys. Chem. C* **2019**, *123*, 21564–21570.